学位論文

Study of relation between emission of supernova shock breakout and central engine activity

(超新星ショックブレイクアウトと中心エンジンの活動性との関係について)

平成 27 年 12 月博士（理学）申請

東京大学大学院理学系研究科
天文学専攻
大谷　友香理

Abstract

In this thesis, I theoretically predict how the properties of ultra-relativistic shock breakout emission depend on the temporal shock evolution. The fundamental motivation is the fact that shock breakout has been believed to be a prerequisite moment for any successful explosion of a core-collapse supernova, no matter how relativistic the explosion is. For future observations, it is worth while to predict the emission features for obtaining information on the mechanism of stellar explosion. Regardless of that, majority of the former studies suppose only non-/mildly- relativistic cases. Even the rest few studies have not calculated the spectrum by considering bulk-Compton scattering, which is regarded as an important process for shock breakout emission. In this thesis, I study effects of the bulk-Comptonization on spectra of emission generated from a strong shock passing through the stellar surface or circumstellar medium (CSM) with ultra-relativistic velocities. For that purpose, I construct a Monte-Carlo code, in which relativistic specification (such as Lorentz transformation and Klein-Nishina formula for Compton scattering) is taken into account.

First, I investigate ultra-relativistic shock breakout at the stellar surface, in which the shock is always accelerated to reach the surface. The resultant spectrum has two peaks when the averaged energy of bulk-Comptonized photons is about 20–30 times higher than that of thermal photons before Compton scattering, otherwise a single peak. As a development of the study, I examine if there is a possibility that shock breakout has some relationships with the observed long gamma-ray bursts (l-GRBs). Some features of spectral shape resemble those of l-GRBs, but the timescale of shock breakout is far shorter.

As a next step, I calculate the spectra and light curves of ultra-relativistic shock breakout in the CSM, where the shock is accelerated or decelerated depending on the energy injection rate from the central engine. The results show that decelerated shocks would tend to emit higher energy ($>$100 MeV) photons exclusively in the beginning of the shock breakout. Meanwhile, the spectral shape of the emission from accelerated shocks slightly changes with time. It might be difficult to explain the observed spectral shapes of l-GRBs.

In addition to the studies of ultra-relativistic shock breakout mentioned above, I study another topic, aiming at explaining the observation of an X-ray outburst (XRO 080109/SN 2008D) generated from a mildly-relativistic shock. In this study, I explore the dependence of mildly-relativistic shock breakout on shock asymmetry and the viewing angle Θ, by assuming an axisymmetric ellipsoidal shock. A comparison with XRO 080109 reveals that both of the observed spectrum and light curve can be explained by the axisymmetric model with oblateness of ≈ 0.3 and $\Theta > 30$ deg.

Contents

List of Figures

List of Figures

List of Figures

List of Tables

Chapter 1

Introduction

Stars more massive than 8 solar masses turn into core-collapse supernovae (CCSNe) within tens of millions of years after their birth. Since a huge amount of energy is released in the form of radiation by the subsequent explosion, they are known to become most powerful phenomena in the Universe. Though majority of the energy on the order of 10^{53} erg is converted into a huge amount of neutrinos for only several sec during the core-collapse, shock waves formed near the surface of the central core destroy progenitor stars, so that they begin to release the rest of the energy in the form of kinetic energy of matter in the envelope and emission from the stellar surfaces.

Study of neutrino transport is indispensable to understand the fundamental supernova physics because neutrinos dominate the energetics of this phenomenon. On the other hand, there are not very large possibilities of catching short bursts of neutrino particles towards the Earth. For this reason, the electro-magnetic emission is an important probe to understand the physics of supernovae, such as internal structure, nucleosynthesis, and explosion mechanism. In addition, high-energy emission generated in the very early phases contains much information about kinetic motion of the matter and the size of the progenitors. Especially, the first coming photons after core-collapse of a star that are generated from a shock wave when it breaks out the stellar surface (shock breakout) imprint that such information on the light curves and spectra (e.g. Falk, 1978; Klein & Chevalier, 1978; Ensman & Burrows, 1992; Soderberg et al., 2008). For example, some characteristic γ-ray emission (long Gamma-ray bursts; GRBs) associated with CCSNe originating from massive progenitors strongly suggests that some supernova explosions are asymmetric and probably forming jet-like structures blowing with ultra-relativistic velocities (Ruderman, 1975; Schmidt, 1978).

In this thesis, I investigate the relation between features of shock breakout emission and behaviors of the shock emerging from the stellar surface.

The main subject (Chapter 2 and 3) of this thesis is to investigate the properties of non-thermal γ-ray emission generated from the shock propagating in the stellar surface or the dense CSM. The subject aims at two goals. The first one is to find some relations between the shock breakout emission and the time-dependent activities of the central engines. Since the motion of shocked matter depends on energies supplied from the central core, it is

expected that one can extract some information on the central engine by studying influence of the motion of the shock on the emission. The second motivation is to find corresponding phenomena of the ultra-relativistic shock breakout by comparing with the observed X-ray or γ-ray transients. The leading candidates are long-GRBs. A long GRB begins with prompt γ-ray emission (lasting $\gtrsim$several sec) followed by lower energy (from optical to X-ray) afterglow emission (lasting $\gtrsim$several days). Most GRBs have similar properties in their spectra of the prompt phase, and luminosity behaviors of afterglow (Band et al., 1993). Based on the properties, GRB emission has long been thought to originate from synchrotron radiation emitted by acceleration of ultra-relativistic electrons (Preece et al., 1998). However, recent development in follow-up observations (, especially by the *Swift* satellite,) reveals presence of some properties inconsistent with the synchrotron model (Kaneko et al., 2006; Goldstein et al., 2012). To solve the problems, some former studies suggested that thermal photons with energies enhanced by non-thermal radiative processes might produce the prompt emission of GRBs (Paczynski, 1986; Goodman, 1986; Thompson, 1994; Mészáros & Rees, 2000). If the view is right, GRBs must originate from very similar radiation processes to shock breakouts. Therefore, discussing the similarities and differences between them would be good for understanding of the physics of GRBs.

To achieve the aims referred in the preceding paragraph, I make calculations of photon traveling across an ultra-relativistic shock. As a preliminary step (Chapter 2), I have studied emission of ultra-relativistic shock breakout at the surface of a Wolf-Rayet star (Ohtani et al., 2013). The resultant emission overlaps with the spectral features of typical GRBs, but its scale of the duration and total radiation energy are far smaller. This means that a larger emission region must be required to explain a GRB by a shock breakout. In addition, in order to know the relations between the behavior of a shock with various velocities and the central engine activity, further calculations in different situations are required. The behavior of a shock is determined by the energy injection rate and the density distribution of the upstream matter. The density gradient in the surface layer has a large negative value. It predicts acceleration of the shock until it disappears at the stellar surface, irrelevant to the energy supply to the shock after the generation (Nakayama & Shigeyama, 2005).On the contrary, once a new shock generates by collision between the ejected matter and the CSM, its behavior depends on the energy injection rate from the central engine (Blandford & McKee, 1976). For example, if the energy injection rate is constant with time, the shock will propagate with a constant velocity.

For the reasons referred in the previous paragraph, as the subsequent study (Chapter 3) I calculate emission from ultra-relativistic shock breakout in a CSM associated with energy supply from the central engine by using the Blandford & McKee self similar solutions.

In Chapter 4), I have another topic, which is for reproducing the observed properties of a famous X-ray outburst followed by a supernova. Recently, a significant progress was made in study of shock breakout through detailed observations of a bright X-ray outburst

080109/SN 2008D (Soderberg et al., 2008). The outburst is thought to be associated with a shock of mildly-relativistic velocities. Analysis of the luminosity evolution and spectrum of the outburst led to discoveries of unexpected properties, namely, evidence of shock breakout in the circumstellar matter (CSM), the existence of a non-thermal component in the spectrum, and possibility of asphericity. A previous theoretical study ascirbed the non-thermal property to photons obtaining the bulk kinetic energy of downstream electrons through electron scattering, using a 1D hydrodynamical code (Suzuki & Shigeyama, 2010a). The observed shape of the light curve can be explained by the influence of an asymmetric explosion (Suzuki & Shigeyama, 2010b). Both of these studies result in very intrinsic arguments for understanding properties of shock breakout. However, in order to obtain information on the geometry of supernova such as 2008D, there is a small problem. That is, though the light curve is examined using a 2D hydrodynamical model, the spectrum is explained in the context of a 1D model that was not turned to this particular supernova. To solve the problem, I examine both the light curve and spectra (of mildly-relativistic shock breakout) using a 2D model characterized with empirical formulae by Suzuki & Shigeyama (2010b).

From the following section, I briefly summarize the history of major studies about GRB and shock breakout.

1.1 Outline of the review

In order to get a perspective focusing on the problem about the supernova associated emission, it is necessary to understand what happens from the beginning of CCSNe to the explosions. First of all, I describe an overview of the birth of CCSNe including the picture of gravitational contraction of the core of a massive star (core-collapse), and generation of a bounce shock. The subsequent contents are recent studies about the central engines and hydrodynamical evolution of the inner region of supernovae. Finally, properties of electro-magnetic emission from the explosion (GRB and shock breakout) are summarized.

1.2 Pre-supernova evolution

Stars are born from collapsing clouds mainly composed of hydrogen molecules, and they achieve hydrostatic equilibrium followed by the ignition of nuclear fusion at the center. Thus, if the effect of the rotational motion can be neglected, a star should be a perfect sphere. The balance is expressed by equating the gravitational force and the pressure on a spherical shell.

Sum of the inward and outward pressure on the shell $4\pi r^2 \times [P(r) - P(r + dr)]$ must equals to the gravitational force exerted to the shell with the mass $dM_{\rm r}$, $-GM_r dM_r/r^2$,

where G is the gravitational constant. Therefore, the equilibrium can be written as follows.

$$\frac{1}{\rho}\frac{dP}{dr} = -\frac{GM_r}{r^2}. \tag{1.1}$$

The mass $M_{\rm r}$ enclosed by the sphere with a radius r is obtained by integrating

$$\frac{dM_r}{dr} = 4\pi r^2 \rho. \tag{1.2}$$

Inside the photosphere of a star, the luminosity L is expressed in proportion to the radial temperature gradient dT/dr, using the diffusion approximation as

$$\frac{dT}{dr} = -\frac{3}{4ac}\frac{\kappa\rho}{T^3}\frac{L}{4\pi r^2}, \tag{1.3}$$

where a is the radiation constant, c the speed of light, κ the opacity. Evolution of stars are driven by the nuclear fusion reactions. If the collapse can generate sufficient heat to support the conversion of the core elements into the heavier ones, the core evolves through the periods of hydrogen burning (10^7 yr), helium burning (10^6 Myr), carbon burning (10^3 yr), neon burning (10^1 yr), oxygen burning (10^0 yr), and silicon burning (1 day). A star more massive than 8 $M_\odot$ in the main sequence phase finally evolves to have an onion shell structure composed of layers with different elements including a core composed of iron at its center. Figure 1.1 displays the evolution of the densities and temperatures at the center of 15 and 25 $M_\odot$ stars (Woosley et al., 2002). Because iron is the most stable nucleus, it requires additional energy to produce other elements. Further nuclear reactions result in a catastrophic event.

From the time of production of the iron core, electrons become relativistically degenerate, having temperatures of $\approx 10^{10}$ K, and densities of $\gtrsim 10^9$ g cm^{-3} at the center of the core. The force of gravity is cancelled by the increased degeneracy pressure of electrons. The high temperatures and densities induce the photo-disintegration of iron nuclei

$$\gamma + {}^{56}_{26}\mathrm{Fe} \rightarrow 13\,{}^{4}_{2}\mathrm{He} + 4\mathrm{n} - 124.4\mathrm{MeV}, \tag{1.4}$$

together with electron capture reactions

$$e^- + N(Z, A) \rightarrow N(Z-1, A) + \nu_e, \tag{1.5}$$

During the photo-disintegration processes, the energies are supplied via the radiation field, originally from the internal energy of the gas. Therefore, once photo-disintegration occurs, the gas pressure in the core cannot increase sufficiently to sustain the core from gravitational contraction. In the case of the star less massive than about $11M_\odot$, which has a core of O, Ne, or Mg just before the explosion, electron-capture can cause the collapse.

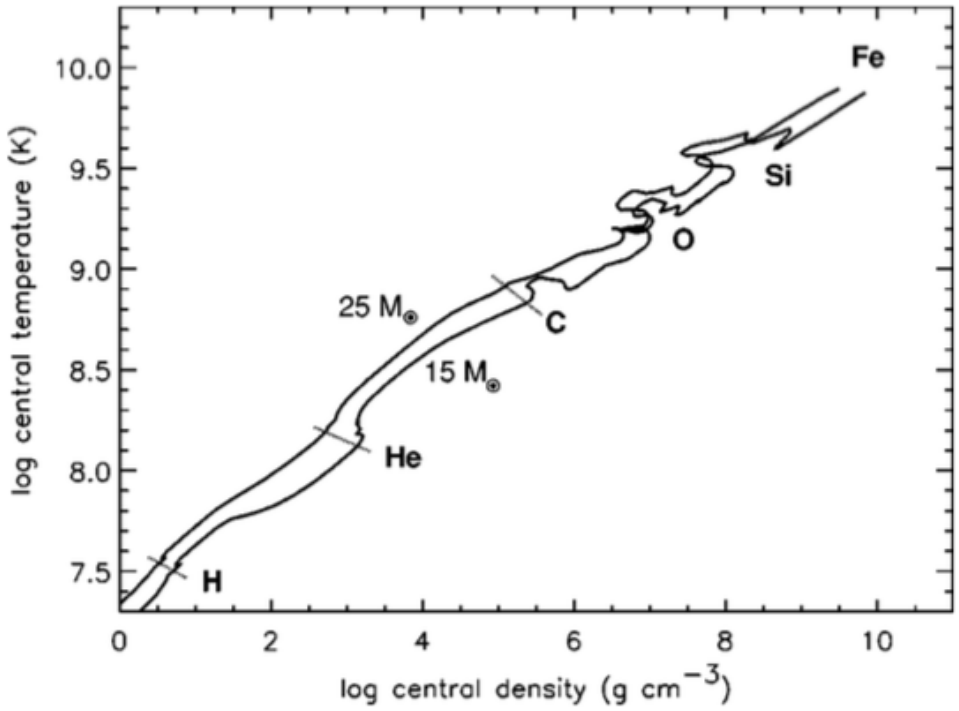

Figure 1.1: Temperature and density evolution at the central regions of main sequence stars with mass of 15 $M_\odot$ and 25 $M_\odot$, until they grow into iron cores (Woosley et al., 2002).

The core-collapse proceeds on the dynamical timescale

$$t_{\rm dyn} = \left(\frac{R^3}{2GM}\right)^{1/2} = 0.05 \left[\left(\frac{R}{10^8\ {\rm cm}}\right)^3 \frac{1.5 M_\odot}{M}\right]^{1/2} \ {\rm sec.} \tag{1.6}$$

The amount of the released energy is

$$\Delta E_{\rm grav} \approx -G M_{\rm c}^2 \left(\frac{1}{R_{\rm c}} - \frac{1}{R_{\rm nc}}\right) \approx \frac{G M_{\rm c}^2}{R_{\rm nc}} \approx 10^{53}\ {\rm erg}, \tag{1.7}$$

where $M_{\rm c}$ ($\approx 1.5\ M_\odot$) and $R_{\rm c}$ ($\approx 10^8$ cm) are the mass and the radius of the core before the collapse, and $R_{\rm nc}$ ($\approx 10^6$ cm) is the final radius. The kinetic energy of the ejected matter is

$$\Delta E_{\rm kin} = \frac{1}{2}\left(M - M_{\rm c}\right) v^2 \approx 10^{51}\ {\rm erg}, \tag{1.8}$$

which is only about % of the released energy. Most of the rest energies are converted into neutrinos.

The mean-free path of a neutrino depends on coherent scattering $A + \nu_{\rm e} \rightarrow A + \nu_{\rm e}$, and

expressed by the following equation.

$$\lambda_\nu = (\sigma_{\rm A} n_{\rm A})^{-1} \approx 10^6 \text{ cm} \left(\frac{\rho}{10^{11} \text{ g cm}^{-3}} \right)^{-5/3} \left(\frac{A}{56} \right)^{-1} \left(\frac{Y_{\rm e}}{26/56} \right)^{-2/3}, \tag{1.9}$$

where A denotes the mass of the element, $\sigma_{\rm A}$ the cross section, $n_{\rm A}$ the number density, $Y_{\rm e}$ the number of electrons per nucleon, and ρ the mass density. The length of λ_ν is much smaller than the core radius and the timescale of the diffusion

$$\tau_{\nu,\rm diff} = \frac{R_{\rm c}^2}{c\lambda_\nu} \approx 0.3 \text{ sec} \left(\frac{R_{\rm c}}{10^8 \text{ cm}} \right)^2 \left(\frac{10^6 \text{ cm}}{\lambda_\nu} \right), \tag{1.10}$$

are longer than the dynamical timescale $t_{\rm dyn}$, the produced neutrinos can not escape from the core as long as the density is higher than 10^{11}–10^{12} g cm^{-3}.

Immediately after the core collapse, collision of the falling matter and the inner core results in bounce at the the surface of the core. Then, a strong shock wave generates at the surface of the core and begins to propagate outward. Due to the shock heating the downstream matter, nuclear reactions start and produce radioactive elements such as nickel.

1.3 Evolution of supernova from shock generation to stagnation

The development of the shock increases the temperature up to $\approx 10^{11}$ K. The heat energy is consumed in the reactions of photo-disintegration of nuclei of heavy elements. Only within 1-2 msec, the shock exhausts its energy, and the cooling shock stagnates at a radius of 1-2$\times 10^7$ cm. How can the shock propagation restart ? The mechanism has been controversial, though there are some persuasive theories. In the subsequent section 1.3.1, I summarize two of the most well-known models.

1.3.1 Theoretical models of the central engine

There are several models proposed to explain the mechanisms of the stalled shock turning into explosion. In this section, I write about "delayed neutrino heating model" and "magnetohydrodynamic model".

1.3.1.1 Delayed neutrino heating

Neutrino heating model argues that the revival of the shock wave owes to neutrino absorbed by the matter in the outer layer of the core (e.g. Bethe & Wilson, 1985; Janka & Mueller, 1996; Janka, 2001). Though neutrinos interact only with the weak force, some of them may

collide with the matter before escaping from the star. Thus, in the region between the core and the shock, both cooling via neutrino emission and heating via absorption can work as follows.

$$\nu_{\rm e} + n \leftrightarrow p + e^-, \tag{1.11}$$

$$\bar{\nu}_{\rm e} + p \leftrightarrow n + e^+. \tag{1.12}$$

The reaction rates of the heating and cooling depend on the temperature in different manners. The formulation is derived by Janka (2001), for example. The cooling rate Q_ν^- per unit volume is expressed as

$$Q_\nu^- = \frac{3\alpha^2+1}{8}\frac{\sigma_0 c}{(m_{\rm e}c^2)^2}\int_0^\infty d\epsilon\ \epsilon^3\left(n_{\rm p}\frac{dn_{\rm e^-}}{d\epsilon} + n_{\rm n}\frac{dn_{\rm e^+}}{d\epsilon}\right) \tag{1.13}$$

$$\approx 145\ {\rm MeV\ s^{-1}}\frac{\rho}{m_{\rm u}}\left(\frac{kT}{2\ {\rm MeV}}\right)^6, \tag{1.14}$$

where $\sigma_0 = 1.76\times10^{-44}\ {\rm cm^2}$, $\alpha = -1.26$, ϵ the neutrino energy, $n_{\rm j=p,n}$ the number density of the nucleon, and $m_{\rm u}$ the atomic mass unit. On the other hand, the heating rate Q_ν^+ is

$$Q_\nu^+ = Q_{\nu_{\rm e}}^+ + Q_{\bar{\nu}_{\rm e}}^+, \tag{1.15}$$

$$Q_{\nu_{\rm i}}^+ = \frac{3\alpha^2+1}{4}\frac{\sigma_0 c n_{\rm j}}{(m_{\rm e}c^2)^2}\int_0^\infty d\epsilon_\nu\int_{-1}^{+1}d\mu\frac{d^2n_{\nu_{\rm i}}}{d\epsilon_\nu d\mu}\epsilon_\nu^3. \tag{1.16}$$

The above equations result in

$$Q_\nu^+ \approx 160\ {\rm MeV\ s^{-1}}\frac{\rho}{m_{\rm u}}\frac{L_{\nu_{\rm e},52}}{r_7^2\langle\mu_\nu\rangle}\left(\frac{k_{\rm B}T_{\nu_{\rm e}}}{4\ {\rm MeV}}\right)^2, \tag{1.17}$$

where $\mu = \cos\theta$, θ the angle between the directions of neutrino and the radial, $L_{\nu_{\rm e},52}$ the luminosity of $\nu_{\rm e}$ in units of 10^{52} erg s^{-1}, $k_{\rm B}$ the Boltzmann constant, and r_7 the radius in units of 10^7 cm.

Due to the temperature dependencies, a heating dominated region ("gain region") can be formed outside the cooling dominated region. Figure 1.2 shows the schematic view in a supernova. At the inner boundary of the gain region, at which $Q_\nu^+ = Q_\nu^-$, the following relation would be satisfied.

$$R_{\rm g,7}\left(\frac{k_{\rm B}T_{\rm g}}{2\ {\rm MeV}}\right)^3 \approx 1.05\sqrt{\frac{L_{\nu_{\rm e},52}}{\langle\mu_\nu\rangle_{\rm g}}}\left(\frac{kT_{\nu_{\rm e}}}{4\ {\rm MeV}}\right), \tag{1.18}$$

where $R_{\rm g,7}$ is the radius of the gain region in units of 10^7 cm, $T_{\rm g}$ the temperature at $r_7 = R_{\rm g,7}$, and $\langle\mu_\nu\rangle_{\rm g}$ the factor between 0.25 and 1.

The key issue of the mechanism is whether the neutrino heating can be strong enough

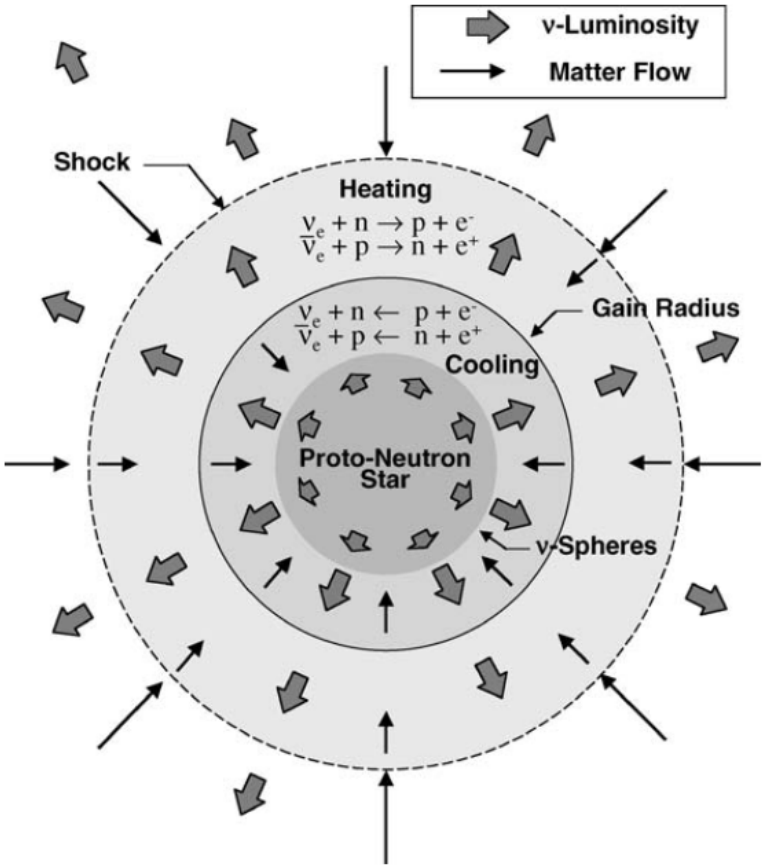

Figure 1.2: Neutrino transport in a core-collapse supernova (Mezzacappa, 2005).

to push the accreting matter outward. Former studies examined if the revival shock can reach the stellar surface by solving the neutrino transfer (e.g. 1D simulation: Burrows et al. 1995; Rampp & Janka 2000; Liebendörfer et al. 2001; Sumiyoshi et al. 2005; Kitaura et al. 2006, 2D: Herant et al. 1994; Burrows et al. 1995; Mezzacappa et al. 1998; Buras et al. 2003; Suwa et al. 2010; Müller et al. 2012, 3D: Fryer & Warren 2002; Takiwaki et al. 2012; Hanke et al. 2013; Müller 2015). In the cases of 1D hydrodynamical models, most studies have concluded that the shock does not success in reaching the stellar surface. However, in reality, part of the accreted matter would be taken away from the shock due to the hydrodynamical instabilities, such as convection and standing accretion shock instability. Several 2D/3D simulations indicate that the effects of these instabilities can make the gain region larger and enhance the shock propagation up to the stellar surface.

1.3.1.2 Magnetohydrodynamics

The magnetohydrodynamic (MHD) model considers that the rotational magnetic fields strongly support the stellar explosion (e.g. LeBlanc & Wilson, 1970; Bisnovatyi-Kogan et al.,

1976; Meier et al., 1976; Wheeler et al., 2002; Akiyama et al., 2003; Thompson et al., 2005; Burrows et al., 2007). Due to the conservation of the angular momentum, a star begins to spin rapidly after the collapse. At that time, the magnetic field lines move together with the fluid, and build a coil along the spin axis. During the collapse, the strength of the toroidal component B_ϕ increases depending on the poloidal component B_p and radial gradient rotational velocity $\partial\Omega/\partial \ln r$ of the star, such as

$$\frac{\partial B_\phi}{\partial t} \sim \Omega \left(\frac{\partial \Omega}{\partial \ln r} \right). \tag{1.19}$$

The concentration of the magnetic field causes a strong magnetic pressure along the spin axis, forcing the stalled shock outwards. If the magnetic field of the progenitor is as strong as $\approx 10^{12}$ G at the start of the core-collapse, and the rotation period of the protoneutron star is as short as 10 msec, the toroidal magnetic field can ultimately be strengthened to 10^{14}–10^{15} G. In such a case, the magnetic pressure would become strong enough to compete the gas pressure. As a consequence, the propagation of the shock revives in the toroidal direction.

Several studies indicate that the shock enhancement would be supported also by the magnetorotational instability, which may cause the significant mixing of the fluid (e.g. Meier et al., 1976; Akiyama et al., 2003). In order to ensure the successful explosion without further accretion of the matter, the shock revival should be achieved within several seconds.

1.4 Evolution of supernova remnant

The shock propagation is believed to revive at least in part, then ultimately the shock breaks out the stellar surface and disappears at once. However, when the ejected matter expands into the interstellar matter (ISM), a new shock generates at the boundary. Then, the ejecta expand as a spherical shell (supernova remnant) until reaching to a distance of several pc. Typically, the velocity of the ejecta is 10^9 cm s^{-1} at the time of explosion. The evolution of the remnant is determined by interactions with the ISM, undergoing four phases as described in the following paragraphs (e.g. Woltjer, 1972). Figure 1.3 shows the schematic image of the expanding matter.

Freely expanding phase At first, the ejecta expand freely. Influence of the swept-up ISM is negligible until the mass of the downstream matter exceeds the total mass of the ejecta ($\approx 10 M_\odot$).

Sedov-Taylor phase When the swept-up matter becomes heavier than the ejecta, the remnant begins to decelerate. However, the radiative cooling does not play a significant

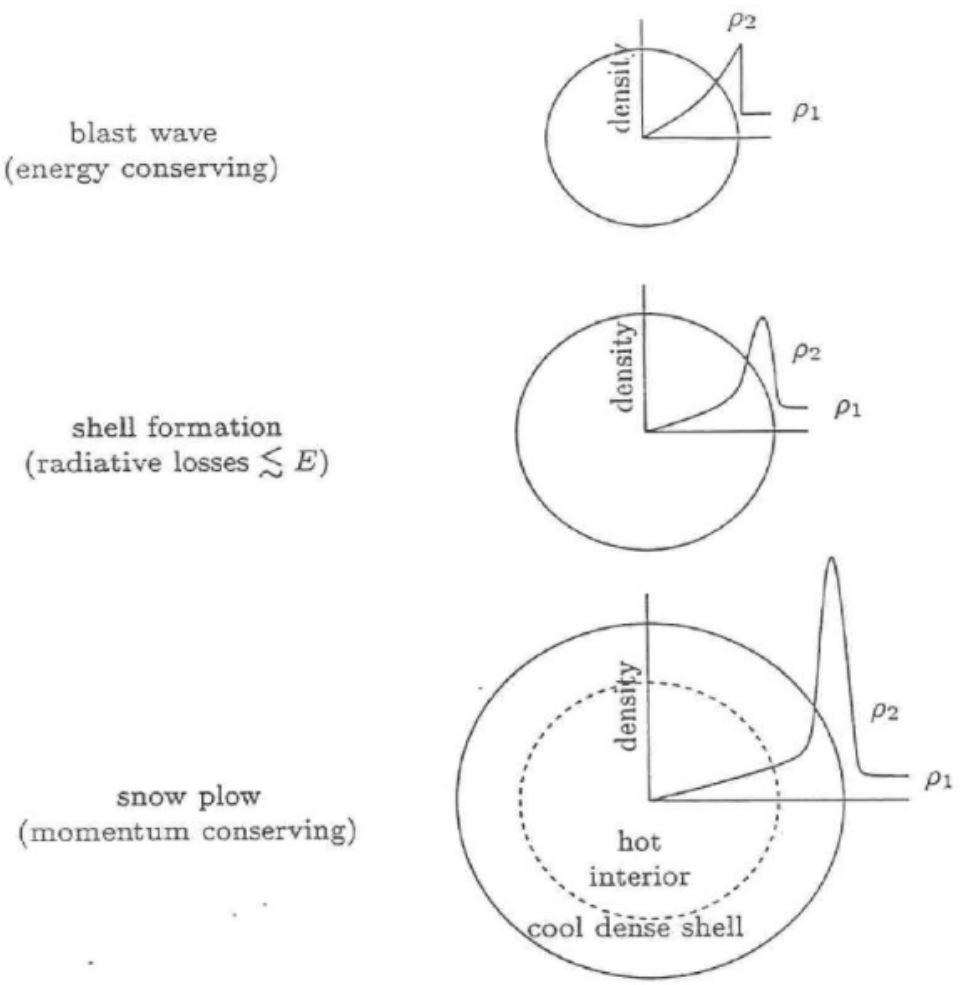

Figure 1.3: Density distribution of the supernova ejecta expanding in the surrounding matter (Shu, 1992).

role yet, because the temperature is still high ($\approx 10^8$ K). For this reason, the matter cools adiabatically.

Radiative cooling phase The shock becomes more slowly and cool, and the effect of radiative cooling becomes important at the surface of the shell. Deep inside the shell, the density is so low that the cooling is negligible. The pressure of the hot matter in this region powers the expansion of the shell, storing the ISM in front the shock ("snow plow").

Shock disappearance When the velocity of the shock decreases down to the speed of sound in the ISM, the shock disappears. The supernova remnant becomes indistinguishable from the ISM.

1.5 Gamma-ray Burst

Long duration gamma-ray bursts (GRBs) are flushes of γ-ray lasting from a few sec to several hundred sec.GRB was accidentally discovered in 1967 by the Vela satellite designed for detection of γ-ray pulses of nuclear weapons.Though several similar phenomena were detected since then (Klebesadel et al., 1973), the origin has been a mystery for long time. Even whether the locations of the sources are in the solar system, in the Milky Way galaxy, or the outside were unknown before 1990's.

From 1991 to 2000, 2704 GRBs were detected by the Burst and Transient Source Experiment (BATSE) on board the Compton Gamma Ray Observatory (CGRO) launched by NASA. The sky map for the samples shows that these bursts come from random directions, which seem to reflect the likelihood of occurrence either at cosmological distances or in the Galaxy (Paciesas et al., 1999). In addition, the BATSE-GRB catalogs clearly suggest that GRBs should be classified into two types, according to the distribution of the durations (Kouveliotou et al., 1993; Fishman et al., 1994). The bursts with durations longer than 2 sec are classified as long-GRBs, while those with the shorter durations are classified as short-GRBs.

In order to improve the location accuracy, a mission called High Energy Transient Experiment (HETE) was developed, planning to launched in 1996. Unfortunately, the first trial (HETE-1) was failed launch. Instead, HETE-2 was successfully launched in 2000, and began working for the localization analysis.

Then, in 1996, *BeppoSAX* satellite was launched by the Italian Space Agency with participation of the Netherlands Agency, for development of X-ray astronomy. The mission includes the similar concept with HETE. The first breakthrough in identification of GRB sources was provided by the *BeppoSAX* in the next year. On February 1997, a highly luminous flash of GRB 970228 was detected by the *BeppoSAX*, followed by a X-ray emission appeared at the same location 8 hours later (Costa et al., 1997).Another GRB 970508 was observed with association of an optical counterpart emission starting 4 hours after the "prompt" γ-ray burst on May. GRB 970508 was associated also by radio emission (e.g. Castro-Tirado & Gorosabel, 1999). Such lower-energy "afterglow" emission lasts at least for several days, providing lots of information on the host galaxy, such as the red-shifts. The optical spectrum of GRB 970508 taken by the Keck telescope revealed the absorption lines, of which the wavelength shift correspond to the redshift of the host galaxy, $z = 0.835$ (Metzger et al., 1997). Under the assumption that the burst was emitted isotropically, the evidence of a cosmological GRB subsequently enabled one to calculate the luminosity and total radiated energy (isotropic equivalent luminosity $L_{\rm iso}$ and energy $E_{\rm iso}$). Generally, $L_{\rm iso}$ is about 10^{53} erg s^{-1}.

The second breakthrough discovery was GRB 980425, which was associated with SN

1998bw (Patat & Piemonte, 1998). On April 1998, the burst was detected by the *BeppoSAX*. A few days later, the appearance of an optical source was confirmed by New Technology Telescope (NTT) at the European Southern Observatory (ESO), within the error box of GRB 980425. The features of the spectral evolution corresponds to an usual Type-Ic supernova, in which the complete lack (or weak signatures) of hydrogen, silicon, and helium is shown. Similarly, associations between GRBs and supernovae are found in several cases (, for example, GRB 030329/SN 2003dh, GRB 060218/SN 2006aj, GRB 120422A/SN 2012bz, and GRB 130427A/SN 2013cq). These discoveries provide the evidence that at least some long-GRBs originate from supernovae (e.g. Wang & Wheeler, 1998). Since the explosion energies of GRB associated supernovae are one order of magnitude greater than others, such supernovae are called hypernovae.

1.5.1 Wolf-Rayet star

Massive stars are surrounded by winds blown by the radiation pressure from the stellar surfaces. If the winds blow off the entire hydrogen envelopes, the progenitors exhibits the helium layers at their surfaces. These stars are called Wolf-Rayet stars, and thought to be the progenitors of long-GRBs.

Based on the spectral features at the explosions, Wolf-Rayet stars are largely classified in two types; the WN and WC stars (Smith, 1968; Crowther, 2007). Figure 1.4 shows the typical optical spectra. As shown in the figure, each of the spectral type is represented by the following features.

- WN: strong nitrogen and helium lines,
- WC: strong carbon and oxygen lines.

1.5.2 General properties of long-GRB

Most long-GRBs have some common characteristics in their behaviors. In this section, I summarize the main points.

1.5.2.1 Spectrum

A typical spectrum of emission from a GRB can be represented by the Band function (Band et al., 1993) composed of power-law functions with two different exponents, α and β,

$$N_E(E) = \begin{cases} A\left(\dfrac{E}{100\ \mathrm{keV}}\right)^{\alpha} \exp\left(-\dfrac{E}{E_0}\right) & \text{if } E \geqslant (\alpha-\beta)E_0, \\ A\left[\dfrac{(\alpha-\beta)E_0}{100\ \mathrm{keV}}\right]^{\alpha-\beta} \exp(\beta-\alpha)\left(\dfrac{E}{100\ \mathrm{keV}}\right)^{\beta} & \text{if } (\alpha-\beta)E_0 \geqslant E, \end{cases} \tag{1.20}$$

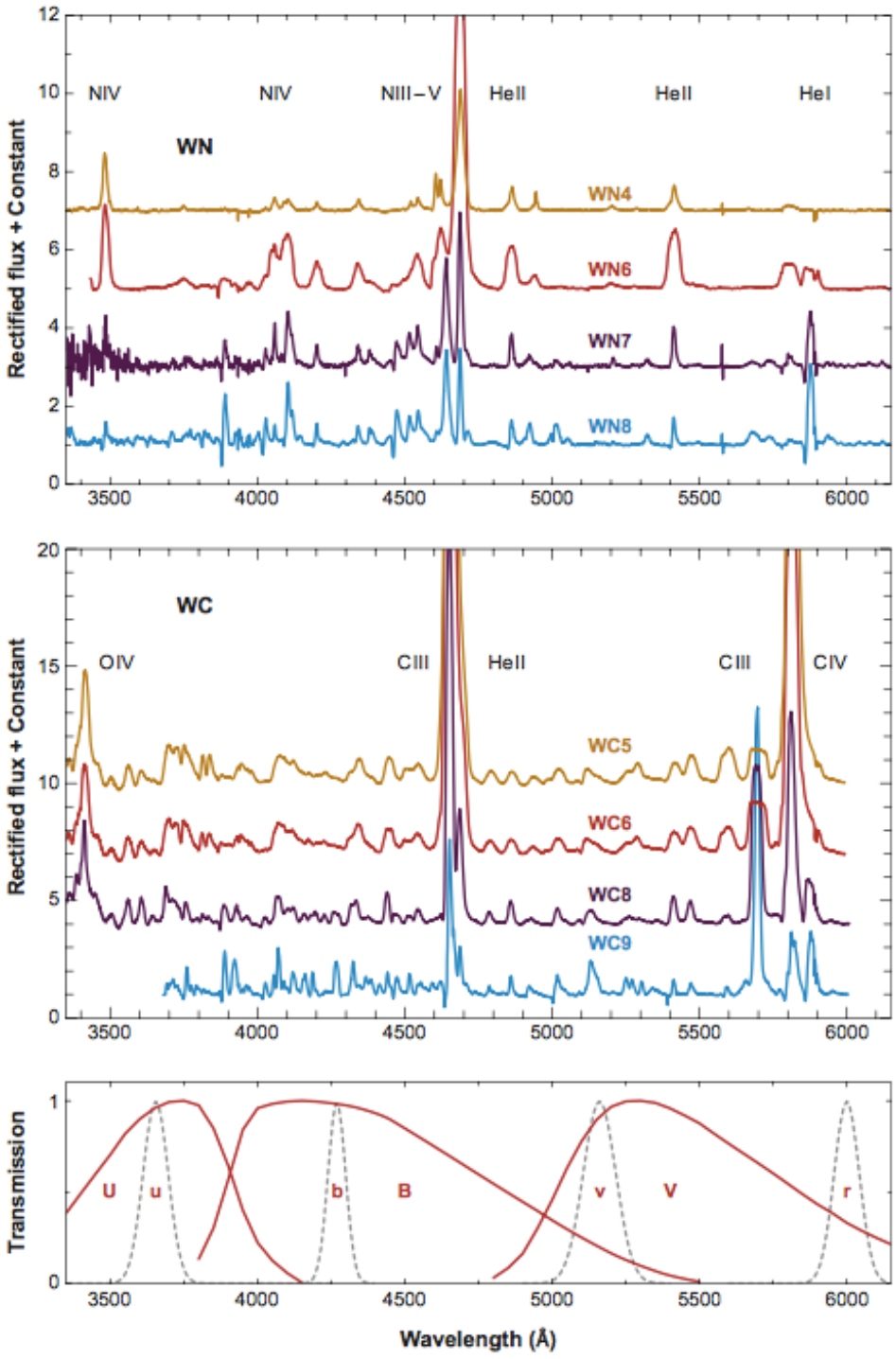

Figure 1.4: Optical spectra of the WN (top panel) and WC (middle panel) stars (Crowther, 2007). The bottom panel shows the narrow-band filters of Smith (1968); Massey (1984) and the broad-band filters of Johnson & Morgan.

where, in case of long GRBs, the break energy $E_{\rm break} = (\alpha - \beta)E_0$ is $\sim 200^{+300}_{-100}$ keV, the low-energy index $\alpha \sim -1^{+0.5}_{-0.5}$, and the high-energy index $\beta \sim -2.5^{+0.5}_{-0.7}$ (see Figure 1.5; GRB 990123, for example). We should note that the parameters are widely distributed in the range of $100 \lesssim E_{\rm break} \lesssim 1000$ keV, $-2 \lesssim \alpha \lesssim 1$, and $-4 \lesssim \beta \lesssim -1$. Spectral catalogue taken by individual instrument are as follows; BATSE: Preece et al. (2000); Kaneko et al. (2006); Goldstein et al. (2013), *BeppoSAX*: Band et al. (2009); Guidorzi et al. (2011), *Swift*: Butler et al. (2007), *Fermi*/GBM: Guiriec et al. (2010); Nava et al. (2011); Goldstein et al. (2012).

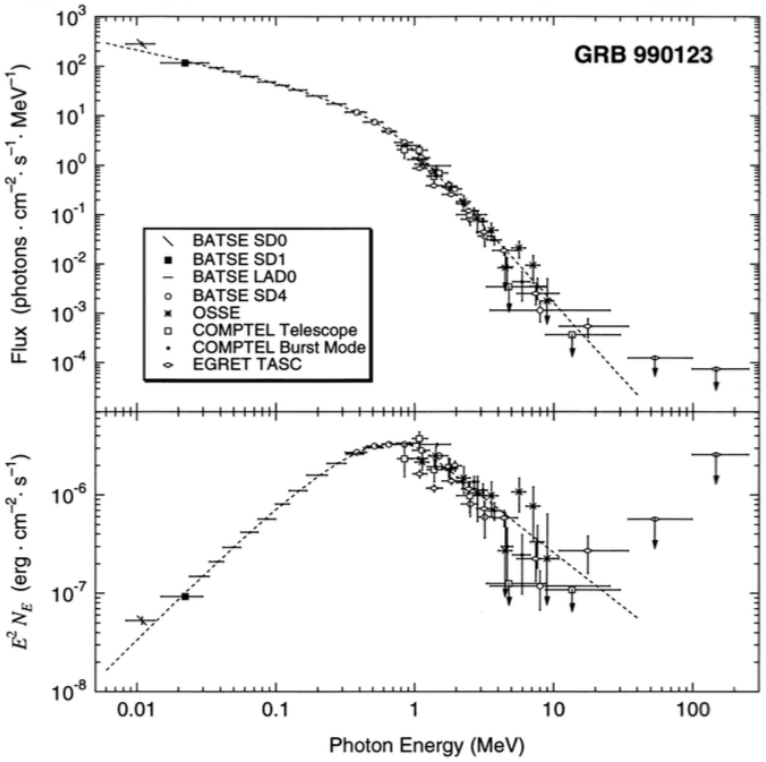

Figure 1.5: Integrated spectrum of GRB 990123, which displays the typical Band features of the prompt bursts (Briggs et al., 1999). The top panel shows the number flux and the bottom panel νF_ν.

1.5.2.2 Time variability

A GRB light curve consists of a single pulse or otherwise many individual pulses, as shown in Figure 1.6. Typically, both the number and the characteristic timescale of the pulses are very different from one burst to another.

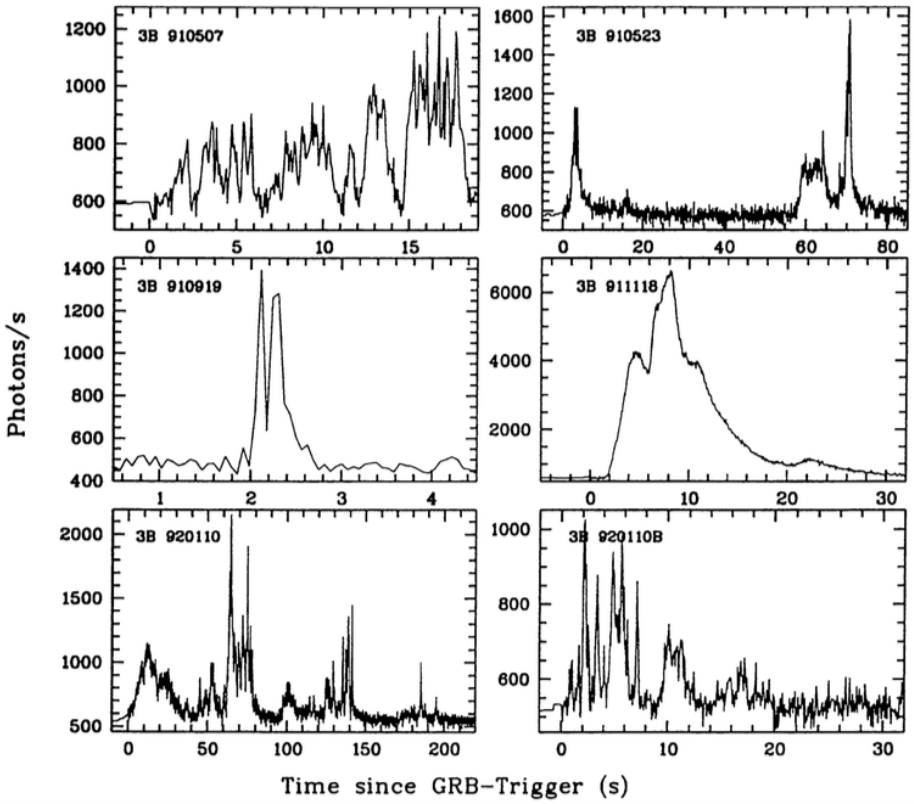

Figure 1.6: Examples of GRB light curves (Greiner, 1999).

1.5.2.3 Compactness problem

A photon with a high energy can interact with another high photon, producing a pair of an electron and a positron,

$$\gamma + \gamma \rightarrow e^- + e^+ \tag{1.21}$$

The threshold energy is the sum of the rest mass energies of the electron and the positron $2m_{\rm e}c^2 \approx 1.022$ MeV. Pair-production can occur when $E_1 E_2 > (m_{\rm e}c^2)^2$, where $E_{\rm i=1,2}$ is the photon energy in the rest-frame of the gas fluid. Because of the high flux of MeV-photons in GRBs, it is necessary to discuss how γ-ray photons escapes from the source without being prevented by pair-production (Ruderman, 1975; Schmidt, 1978).

The short-term variabilities in the prompt emission of GRBs require the source objects to be compact, if the expanding velocities are non-relativistic. For example, when the timescale of the variability $\delta t \approx 10$ msec, the scale of the size R is as follows.

$$R \sim c\delta t \lesssim 10^9 \text{ cm}. \tag{1.22}$$

Assuming that the radiation is isotropically equivalent, the luminosity of the radiation is

$$L_{\gamma\gamma} = 4\pi d^2 f_{\gamma\gamma} \sim 10^{51}\ \mathrm{erg\ s^{-1}} \left(\frac{d}{10^{28}\ \mathrm{cm}}\right)^2 \left(\frac{f_{\gamma\gamma}}{10^{-6}\ \mathrm{erg\ s^{-1}\ cm^{-2}}}\right), \tag{1.23}$$

where d is the distance and $f_{\gamma\gamma}$ the γ-ray flux. The total γ-ray fluence is

$$\epsilon_{\gamma\gamma} \sim L_{\gamma\gamma}\delta t \sim 10^{49}\ \mathrm{erg} \left(\frac{d}{10^{28}\ \mathrm{cm}}\right)^2 \left(\frac{f_{\gamma\gamma}}{10^{-6}\ \mathrm{erg\ s^{-1}\ cm^{-2}}}\right). \tag{1.24}$$

The cross section is close to the Thomson cross section σ_T, so the number of collisions per unit time is $\sigma_\mathrm{T} f_\mathrm{p} L_{\gamma\gamma}\delta t/m_\mathrm{e}c^2$ where f_p the fraction of photons with energies higher than $2m_\mathrm{e}c^2$. Therefore, optical depth is expressed by

$$\tau_{\gamma\gamma} \sim \frac{\sigma_\mathrm{T} f_\mathrm{p} L_{\gamma\gamma}\delta t}{R^2 m_\mathrm{e} c^2}. \tag{1.25}$$

When the outflow is non-relativistic,

$$\tau_{\gamma\gamma} \sim 10^{13} f_\mathrm{p} \left(\frac{R}{10^9\ \mathrm{cm}}\right)^{-2} \left(\frac{L_{\gamma\gamma}}{10^{51}\ \mathrm{erg\ s^{-1}}}\right) \left(\frac{\delta t}{10\ \mathrm{msec}}\right) \gg 1, \tag{1.26}$$

so photons can not escape from the source (, "compactness problem").

The problem can be solved if considering that the outflow has relativistic velocities. Pair-production is diminished by following two effects caused by the expanding source with a Lorentz factor Γ. Due to the Doppler effect, the energies of photons moving towards the observer increases by factor of Γ. In the rest-frame of the outflow, the occurrence condition can expressed as

$$E_1 E_2 > \frac{\Gamma^2}{4}(m_\mathrm{e}c^2)^2, \tag{1.27}$$

in the relativistic limit. Using the photon flux at energies higher than the peak of the Band spectrum, $N(E)dE \propto E^{\beta_\mathrm{C}} dE$,

$$f_\mathrm{p} \propto \int_{E_\mathrm{i}} N(E)dE \propto E_1^{\beta_\mathrm{C}+1} \propto \Gamma^{2(\beta_\mathrm{C}+1)}, \tag{1.28}$$

for $\beta_\mathrm{C} < -1$. Additionally, due to the beaming effect, the relativistic outflow allows the size of the source become Γ^2 times larger than estimated in Equation (1.22). When photons are emitted isotropically in the rest frame of the outflow, they are collimated to a small angle. The half angle is Γ^{-1}, so the visible region is $4\Gamma^2$ times smaller than the actual surface area. Therefore, the arrival of a photon emitted from the edge of a spherical shell delays $\Delta t \Gamma^2 R/c$ relative to a photon from the center of the shell, namely,

$$R \sim \Gamma^2 c \Delta t. \tag{1.29}$$

In the standard GRB model (synchrotron model), electrons with momentum p in the downstream of shocks are thought to have a distribution as follow.

$$N(p) \propto p^{-(C_{\rm sh}+2)/(C_{\rm sh}-1)}, \tag{1.30}$$

where $C_{\rm sh}$ denotes the compression ratio of the shocked outflow. Since $C_{\rm sh} = 4$ for strong shocks, Equation (1.30) results in $N(p) \propto p^{-2}$, namely, $\beta_{\rm C}$. Therefore, considering the effects of the blue-shifted photons and the beaming, the optical depth for pair-production decreases by a factor of

$$\tau_{\gamma\gamma} \times \Gamma^{2(\beta_{\rm C}+1)} \times (\Gamma^2)^{-2} \sim \Gamma^{-6}. \tag{1.31}$$

When $\Gamma \gg 1$, $\tau_{\gamma\gamma}$ becomes significantly smaller than 1, allowing γ-ray photons to escape. For these reasons, GRBs are believed to originate from outflows expanding with Lorentz factors $\Gamma \gg 1$.

1.5.2.4 Relationships between spectral properties, luminosity, and radiated energy

Based on increased data, many studies have found that most long-GRBs are likely to have some relationships between the properties such as spectra, luminosity evolution, variability, and radiated energies (Norris et al., 2000; Reichart et al., 2001; Guidorzi et al., 2005, 2006; Ghirlanda et al., 2004, 2005; Sonbas et al., 2013; Dainotti et al., 2013, 2015a).

For example, Amati et al. indicate that there is a positive correlation between the photon energies $E_{\rm p,i} = (1+z)E_{\rm p,obs} = (1+z)(2+\alpha)E_0$ at which the νF_ν Band spectra peak (hereafter so-called peak energy) and the total radiated energies (generally represented by the isotropic energies; $E_{\rm iso}$), as shown in Figure 1.7 (2002; 2006; 2008; 2009). The energies $E_{\rm p,i}$ and $E_{\rm iso}$ of a GRB are values in the rest-frame of the burst, and $E_{\rm iso}$ is estimated assuming that the emission is isotropic. The distribution of GRBs in the $E_{\rm iso}$-$E_{\rm p}$ plane is fitted by a power-law function, and the best-fit index is 0.54 ± 0.03 with a 68% uncertainty (1σ) of 0.18 ± 0.02. We should note that there are some arguments about the sample selection bias and the adequacy of the fitting function (e.g. Butler et al., 2009; Dainotti et al., 2015b; Massaro et al., 2008), but even though, the correlation is believed to be a powerful information source of GRB nature. Later, a similar correlation was proposed by Yonetoku et al. (2004), using the isotropic peak luminosity $L_{\rm iso}$ and peak energy $E_{\rm p}$.

1.5.3 *Properties of Swift-GRBs*

The *Swift* satellite is the most famous explorer known for its wide field of view, fastest reaction to the incoming high-energy photons, and high sensitivity in multi-wavelength

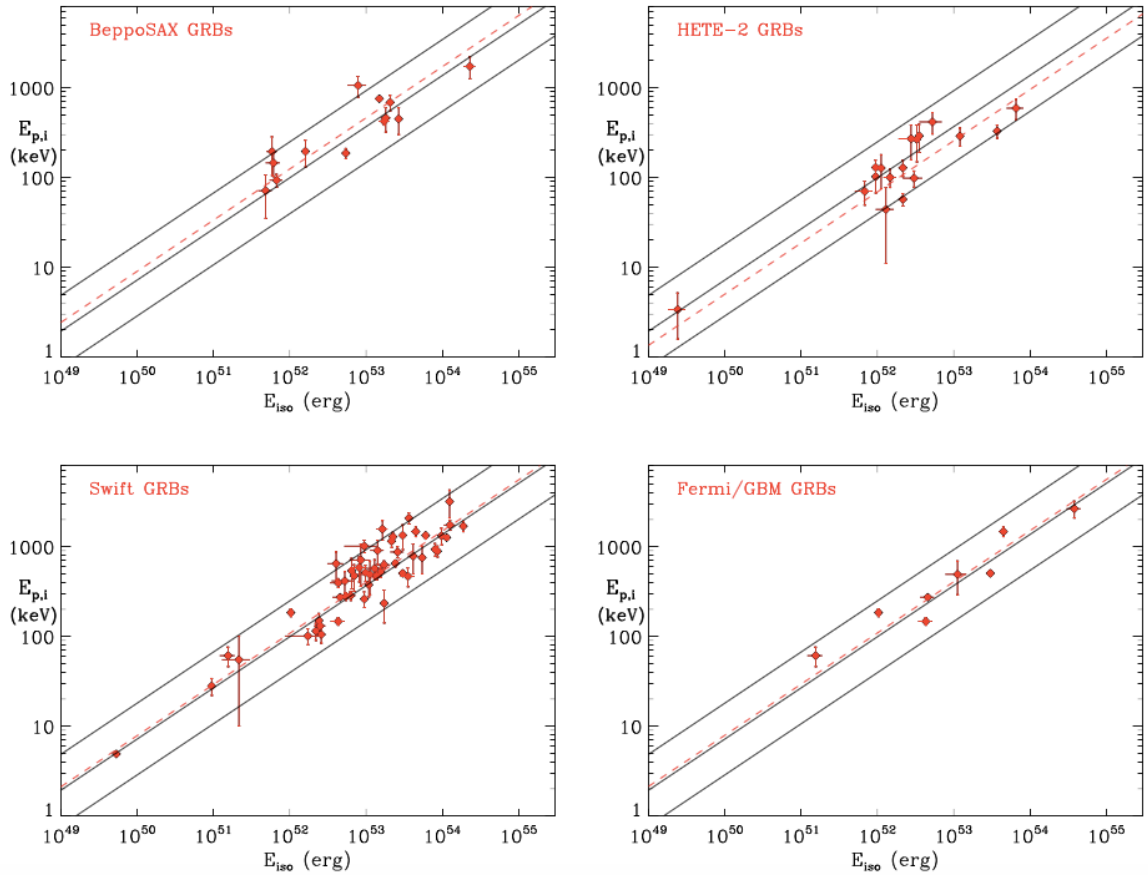

Figure 1.7: The total isotropic energies $E_{\rm iso}$ and the peak energy $E_{\rm iso}$ of 95 GRBs in the redshift range of 0.033 to 8.1, detected by the *BeppoSAX*, *HETE-2*, *Swift*, and *Fermi* (Amati et al., 2009). The solid lines show the best-fits to the all data using a power-law model within 2σ. The dashed lines show the comparison of best-fits to the data taken by each instrument.

study. The mission has been held by NASA since November 2004. [1]

The rapid response acheived smooth combination of the last part of the prompt data and the beginning of the afterglow data (e.g. Tagliaferri et al., 2005; Barthelmy et al., 2005; Liang et al., 2006; O'Brien et al., 2006; Nousek et al., 2006; Margutti et al., 2013). Top two panels in Figure 1.8 display some *Swift*-GRB light curves consisting of the combined BAT and XRT data (left: long-GRB, right: short-GRBs; Gehrels et al. 2009). During the pre-*Swift* period, it had been thought that the phase transition would follow a simple power-law decay. In contrast to the prediction, the combined data lead to the recognition of a tendency of having two distinguishable decay (sometimes linked by a plateau/shallow decay) for each burst, unless the light curve includes another bump component due to a X-ray flare, such

[1] The properties of the *Swift* satellite are summarized in Appendix A.1.

as GRB 050502B and 050724.

The bottom panel of Figure 1.8 and Table 1.1 show the stylized representation and the typical starting times, slope indexes, and the frequencies based on the 380 *Swift*-GRBs up to December 2008. At the first decay segment just after the prompt phases, at least half GRBs rapidly decay in luminosity on the timescale of 10^2–10^3 sec. The relation between the elapsed times since the trigger and the luminosities are expressed by a power-law function with index of ~ -3 (I: "steep decay"). At the turning point to the next afterglow (second or third) segment, their decreasing rate become lower. In most cases the power-law indexes increases to -1 (III: "normal decay") at the time. Some GRBs require further shallower decay with indexes of -0.5 (II: "shallow decay/plateau") before the transition to the normal decay. In this case, the normal decay comes at 10^3–10^4 from the trigger.

Zhang et al. (2006) gives an intrinsic explanation of the typical luminosity behaviors by interpreting the emission as a track of the central engine activity. They claims that a long-lived central engine would be responsible for the existence of the shallow decay phase. One problem appears from the context of the continuous energy injection as referred by Zhang & Mészáros (2001)(, in which the energy supplying rate is derived using the Blandford & McKee self-similar solution). That is, if the continuous energy injection requires the smooth variety of the central engine luminosity, which can not explain the time variabilities of the observed GRBs. In order to avoid the difficulty, Zhang et al. suggests that there might be two different energy sources; the fireball (causing the prompt emission) and magnetic fields (causing the continuous energy injection).

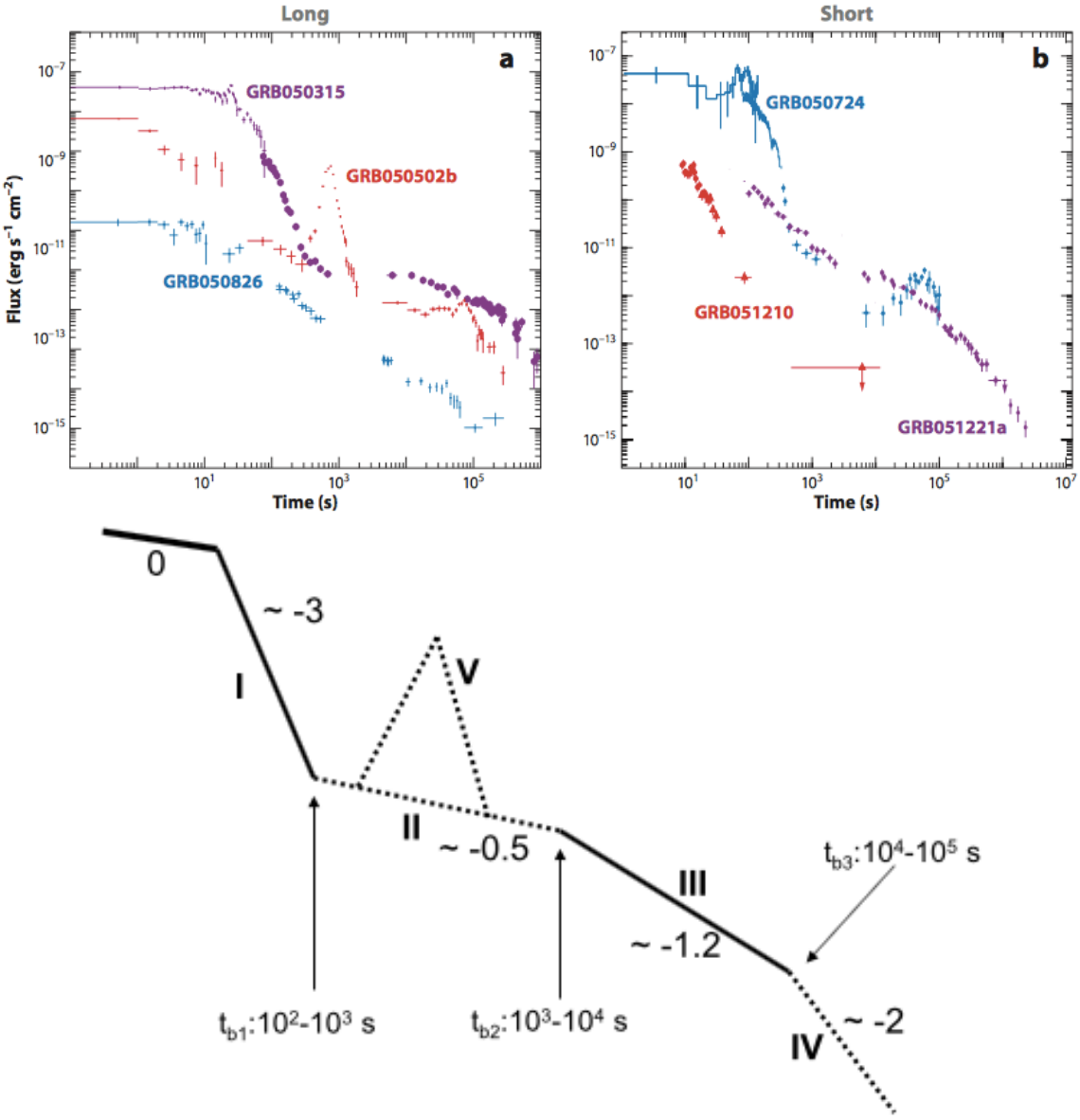

Figure 1.8: Combined *Swift* BAT & XRT light curves (top; Gehrels et al. 2009) and the representative schematic image (bottom; Zhang et al. 2006). Left panel shows the long bursts, and right panel the short bursts. Typical frequencies of each segment are summarized in Table 1.1 with the starting times and the slope indexes (Table 1 of O'Brien & Willingale).

Table 1.1: Representative parameters for GRB light curves (O'Brien & Willingale, 2007).

Phase	Start T (s)	Decay index[a]	Approximate frequency
Steep decline	10^1–10^2	>3	50%
Shallow slope	10^2–10^3	0.5	60%
Classical afterglow	10^3–10^4	1.3	80%
Jet break late phase	10^5–10^6	2.3	20%[b]
X-ray flares	10^2–10^4		50%

[a]Decay index α defined by $F = F_o t^{-\alpha}$.
[b]Of the 80% with no observed jet break, about half had afterglow observations terminate before expected time of jet break.

1.5.4 *Properties of Fermi-GRBs*

The *Fermi* Gamma-ray Space Telescope is the first GRB explorer sensitive for the high energy photons (from MeV to GeV). On June 2008, the *Fermi* was launched by NASA, and it has moved along the low Earth circular orbit (at an altitude of 565 km, and an inclination of 25.5 degree). [2] In the first year after its birth, the *Fermi* telescope have discovered 252 GRBs (138 of them were in the LAT FoV) by the GBM. Figure 1.9 is the sky map from the LAT observation (above 300 MeV). In the following paragraphs, I summarize the important discoveries in GRB owing to the *Fermi* telescope.

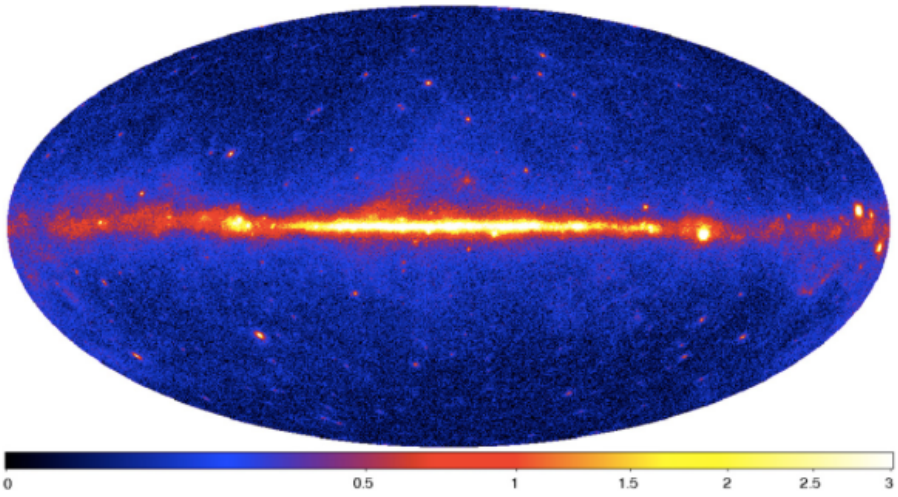

Figure 1.9: Sky map of the *Fermi*/LAT-detected GRBs (Abdo et al., 2009b).

Delayed high-energy component Several Fermi-GRBs have an extra spectral components in addition the Band, in the energies greater than 100 MeV (Abdo et al., 2009a; Ackermann et al., 2010, 2013). For example, Figure 1.10 and 1.11 show the spectra and light curves in multiple energy bands of GRB 090902B using combined data from the GBM and LAT. As shown in Figure 1.10, the energy distribution of the high-energy component follows by a power-law function. From Figure 1.11, it is clear that the onset time of the high-energy emission is several sec with respect to the low-energy emission. The delay are thought to be caused by some intrinsic mechanisms of the central engine or processes of light propagation from the sources to the observer (e.g. Castignani et al., 2014).

Planck component A small number of GRBs have spectra that described using the Planck distributions, rather than the Band distributions. Some of them (910807, 910927, 911118, 970111, 980306, 090902B) have the thermal components only at the beginning (Ghirlanda et al., 2003; Guiriec et al., 2011). Meanwhile, other GRBs (930214, 941023,

[2] The properties of the *Fermi* telescope are summarized in Appendix A.2.

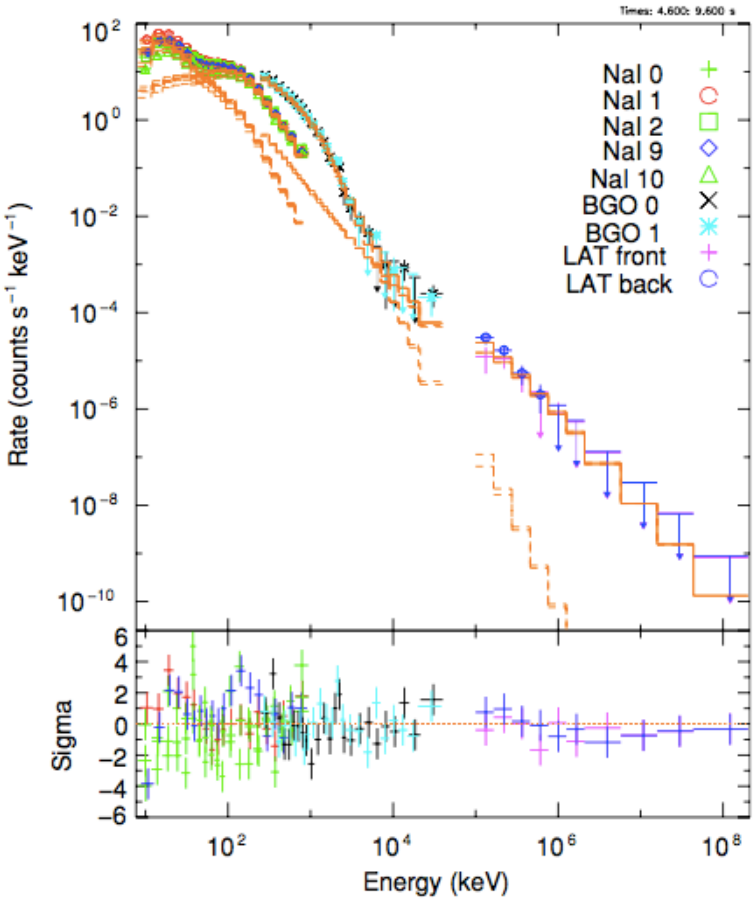

Figure 1.10: Count-rate spectrum of GRB 090902B taken by the Fermi/GBM and LAT (Abdo et al., 2009a). The low-energy component (from 50 keV to 20 MeV) is fitted by the Band function, while the high-energy one (from 100 MeV) a power-law model.

951228, and 990413) have such spectral features throughout the prompt phases (Ryde, 2004; Bosnjak et al., 2006). Note that some GRBs (110721A, 100724B, and 120323A) have both of the Planck and Band components (Guiriec et al., 2011; Axelsson et al., 2012; Guiriec et al., 2013). Figure 1.12 shows the time-integrated spectra of GRB 120323A at beginning (left panel) and end (right panel) of the emission. The spectra are well fitted by a combination of a blackbody and the Band function in both of the two phases, though the non-thermal feature becomes dominant in the later phase.

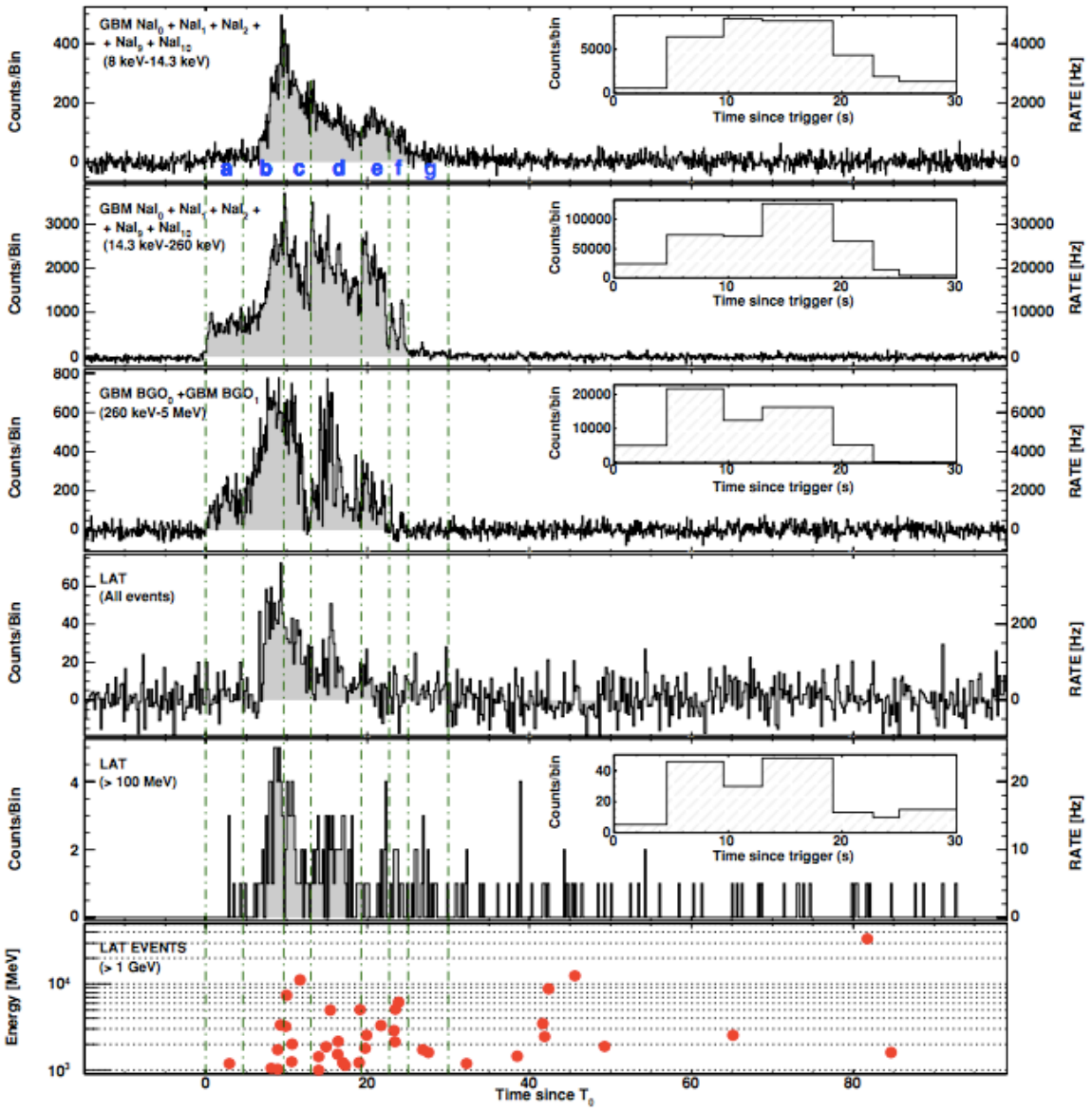

Figure 1.11: Light curves (1st–5th panels) of GRB 090902B in multiple energy bands (Abdo et al., 2009a). The bottom panel shows the photon energies as a function of time.

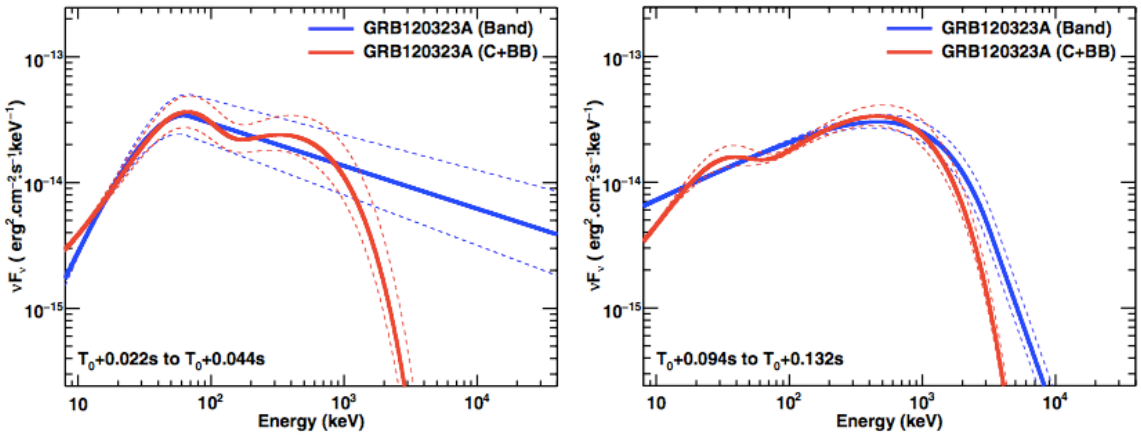

Figure 1.12: Time-integrated spectrum of GRB 120323A fitted by a blackbody combined with the Band function (Guiriec et al., 2013). Each panel shows the emission at beginning (left) and end (right) of the prompt phase.

1.5.5 Radiation

Former studies (e.g. Cavallo & Rees, 1978; Goodman, 1986; Paczynski, 1986) propose that a huge amount of energy (10^{51}-10^{53} erg) confined in a small region (with radius $\approx 10^{6}$-10^{11} cm) would create a fireball of temperature $> mc^2$, initially has a large opacity for pair production and electron scattering. Soon, the energy must be converted into the kinetic energy of an outflow. The forming process of the primordial fireball is a mystery. No matter what is it, GRB emission models have been constructed under the assumption that a fireball must be formed as the energy source of GRB, immediately after the core-collapse. The fireball is thought to expand and ultimately becomes transparent. During the expanding, some fraction of its energy would be converted into the emission. The important problem concerning GRB is what kind of emission mechanism can explain the observed features.

1.5.5.1 Synchrotron model

Standard GRB model has explained the origin of the emission by synchrotron radiation produced by electron moving with ultra-relativistic velocities as follows (e.g. Sari et al., 1998; Preece et al., 1998). (The schematic view is shown in Figure 1.13.)

First of all, a highly relativistic outflow is produced from the central source, and the temperature decreases as $T_\gamma \propto r^{-1}$. The total energy does not vary with time, so the Lorentz factor of the outflow initially increases as $\Gamma \propto r$. The Lorentz factor becomes constant after it reaches a value η, which corresponds to the ratio of the total energy to the mass of the outflow, namely,

$$\eta \sim \frac{L_{\rm iso}}{\dot{M}c^2} \sim 10^{2}\text{-}10^{3}. \tag{1.32}$$

For convenience, the outflow is identified as a group of multiple shell components with different Lorentz factors. Due to the differences in the Lorentz factor, the shells begin to collide with the nearest shells, when the outflow reaches at the radius

$$r_{\rm is} \sim \Gamma^2 c\Delta t \sim 3 \times 10^{13}\ {\rm cm} \left(\frac{\Gamma}{300}\right)^2 \left(\frac{\Delta t}{10\ {\rm msec}}\right), \tag{1.33}$$

where Δt is the timescale of the variability in the prompt phase. The collisions produce shocks with relativistic velocities (so-called internal shocks) at the boundaries of the shells. The radius $r_{\rm is}$ is significantly larger than the photospheric radius of the outflow

$$r_{\rm ph} \sim \frac{\sigma_{\rm T} L_{\rm iso}}{4\pi\Gamma^3 m_{\rm p} c^3} \sim 1 \times 10^{12}\ {\rm cm} \left(\frac{L_{\rm iso}}{10^{51}\ {\rm erg\ s^{-1}}}\right) \left(\frac{\Gamma}{100}\right)^{-3}. \tag{1.34}$$

Due to the interactions with the external matter, the outflow begins to decelerate at the

radius

$$r_{\rm es} \sim 6 \times 10^{17}\ {\rm cm} \left(\frac{E}{10^{51}\ {\rm erg}}\right)^{1/3} \left(\frac{n_{\rm ext}}{1\ {\rm cm}^{-3}}\right)^{-1/3} \alpha^{-2/3}\Gamma^{-2/3}, \tag{1.35}$$

where $n_{\rm ext}$ is the number density of the external matter, and α the half opening angle of the jet. At this time, a forward shock and a reverse shock (external shocks) are produced at the boundary.

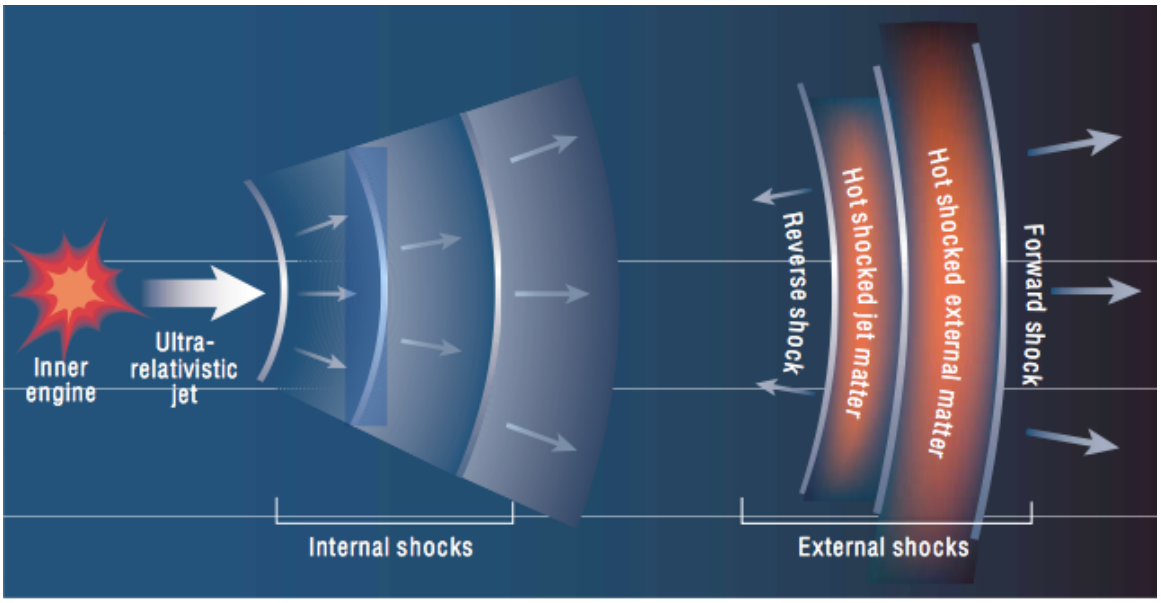

Figure 1.13: Schematic image of GRB synchrotron model (Piran, 2003).

Prompt and afterglow emission of a GRB is thought to be caused by the relativistic electron motions in the internal and external shocks, respectively. In a magnetic field behind the shock, an electron moving with a Lorentz factor $\gamma_{\rm e}$ produces synchrotron radiation with a power

$$P(\gamma_{\rm e}) = \frac{4}{3}\sigma_{\rm T} c \gamma^2 \gamma_{\rm e}^2 \frac{B^2}{8\pi}, \tag{1.36}$$

where γ is the Lorentz factor of the fluid, and B the strength of the magnetic field in the rest-frame of the fluid. The characteristic frequency is

$$\nu(\gamma_{\rm e}) = \gamma \gamma_{\rm e}^2 \frac{q_{\rm e} B}{2\pi m_{\rm e} c}. \tag{1.37}$$

When $\gamma_{\rm e}$ is larger than a critical value

$$\gamma_{\rm c} = \frac{6\pi m_{\rm e} c}{\sigma_{\rm T} \gamma B^2 t} = \frac{3 m_{\rm e}}{16 \epsilon_{\rm B} \sigma_{\rm T} m_{\rm p} c} \frac{1}{t \gamma^3 n}, \tag{1.38}$$

where t is the time in the observer frame, the power decreases with time due to the syn-

chrotron cooling. The spectrum behavior depends on whether γ_c is smaller than the minimum Lorentz factor of electrons γ_m or larger. When $\gamma_c < \gamma_m$, all the electrons are enough energetic so that they rapidly cool until γ_e decreases down to γ_c (, "fast cooling"). When $\gamma_m < \gamma_c$, only some fraction of electrons cools (, "slow cooling"). Assuming the electron distribution as

$$N(\gamma_e)d\gamma_e \propto \gamma_e^{-p} d\gamma_e, \tag{1.39}$$

(via processes such as the Fermi acceleration,) the synchrotron model results in spectra shown in Figure 1.14. The cut-off frequency ν_a indicates the threshold at which synchrotron self-absorption becomes efficient.

The synchrotron model provides good explanations for the origin of the high-energy Band spectra and the afterglow light curves. However, there are two discrepancies between the model and observed GRBs, namely, "line of death" and "energy efficiency".

Line of death Though the low-energy spectral index α is widely distributed between ≈ -2 and ≈ 1, the synchrotron emission model does not allow α greater than -2/3 (Preece et al., 1998).

Energy efficiency The synchrotron model had predicted that the internal shock can release only 40% or less of the energy emitted by a GRB (Preece et al., 1998). However, the photometric data of the Swift-GRBs reveal that ≈70-90% of the total energies are carried by γ-ray photons (Kaneko et al., 2006; Goldstein et al., 2012).

To solve the discrepancies, several studies focus on the photospheric emission from the outflow.

1.5.5.2 Photospheric model

The picture of an expanding fireball has predicted the generation of photospheric emission around the same time as the prompt emission (Paczynski, 1986; Goodman, 1986; Thompson, 1994; Mészáros & Rees, 2000). The fireball initially consists almost entirely of $e^{\pm}$ pairs, and there is a relatively small amount of baryons. As referred in the first paragraph of Section 1.5.5, most of the thermal energy in the fireball is converted to the kinetic energy carried by the baryons (Shemi & Piran, 1990). The conversion is thought to occur a radius

$$r > r_0 \eta, \tag{1.40}$$

where r_0 is the radius at which the accreted matter forms a disk ($\approx 10^7$ cm) and η the parameter defined by Equation (1.32). If the fireball is highly baryon dominated, the radius

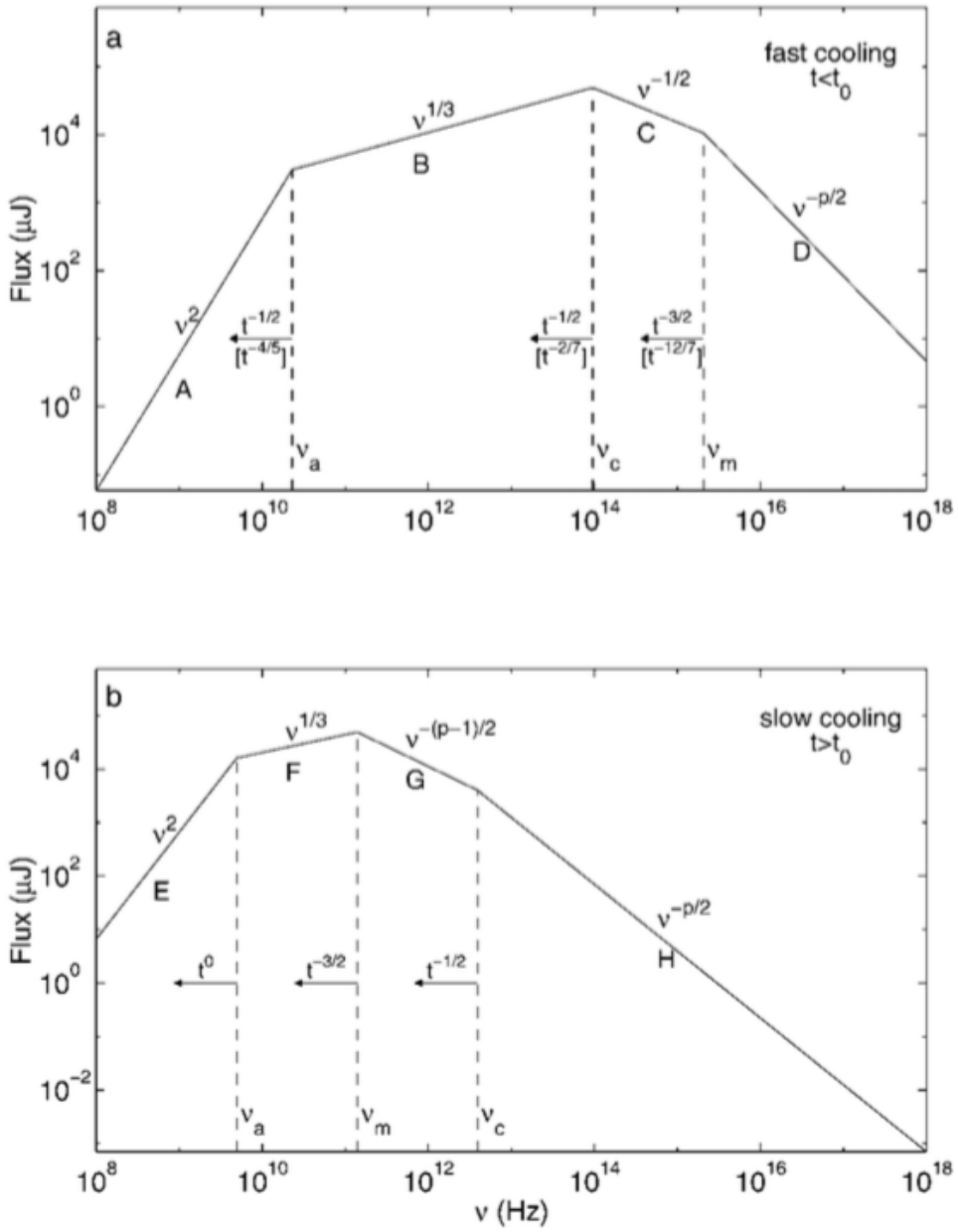

Figure 1.14: Synchrotron model spectra for the fast cooling (top panel) and the slow cooling (bottom panel) phases (Sari et al., 1998).

of the photosphere $r_{\rm ph}$ can be initially smaller than $r_0\eta$. In this case, a significant fraction of the thermal energy becomes radiation escaping from the fireball.

An problem with the photospheric emission model is that the thermal emission alone does not explain the non-thermal spectral features of the observed GRB.

As a cause for the discrepancy, the geometrical effect of the photosphere is focused by some studies, e.g., Pe'er (2008); Lundman et al. (2013); Ruffini et al. (2013). In the direction of the line of sight, the scattering optical depth have an angle dependency expressed by

$$\tau = \int_{R_0}^{R_{\rm out}} \sigma_{\rm T} n_{\rm e} \Gamma (1 - \beta \cos\phi) \frac{dr}{\cos\phi}, \tag{1.41}$$

where ϕ is the angle between the radial direction and the photon travel, R_0 the radius at the photon generation, $R_{\rm out}$ the radius at which the photon escapes from the outflow, and $n_{\rm e}$ the number density of electron. β and Γ denotes the velocity in units of c and the Lorentz factor of the outflow. As a consequence, in reality the position of the photosphere follows an aspherical distribution as shown in Figure 1.15. In the observer frame, the temperature of outflow decreases with the angle ϕ. This is because the effect of adiabatic cooling becomes stronger and that of the Doppler boost becomes weaker. Accordingly, photons close to the line of sight have energies higher than those distant from the line of sight. As a result, the lower-energy component of the spectra becomes softer ($\alpha \approx -1$) in the observer frame, and the higher-energy one becomes harder ($\beta \approx -2$). Figure 1.16 shows the comparison of the resultant spectra and the Planck distribution at a temperature (Goodman, 1986).

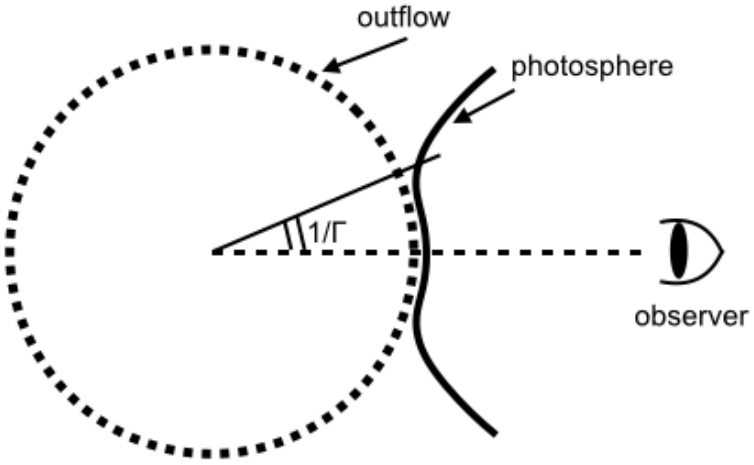

Figure 1.15: Schematic image of the relation between the line of sight and the photosphere of a relativistic outflow.

There is another famous theory studied by Rees & Mészáros (2005); Pe'er et al. (2006); Beloborodov (2010), for example. The key mechanism is dissipation of the kinetic energy in the optically thick region, which is thought to be caused by the internal shock, magnetic reconnection, or collisional processes. After the dissipation, the heated electrons can emit

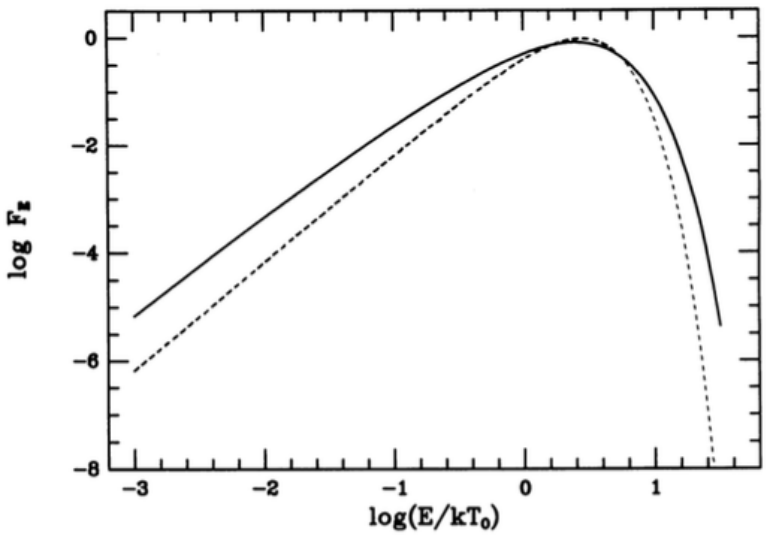

Figure 1.16: Broadening spectrum of the photospheric emission (solid) due to the geometric effect (Goodman, 1986). The dotted line shows the Planck distribution at a temperature.

synchrotron emission or induce inverse Comptonization of thermal photons.

Furthermore, there are still some intriguing studies concerning the photospheric emission. For example, Ito et al. (2014) calculates electron scattering taking account of the complex spatial distributions of the outflow. They considers a jet structure with multiple velocity components as illustrated in Figure 1.17 (top). The figure also shows the resultant spectra (bottom). If the velocity gradients are large enough, the spectra will have non-thermal features, which resemble the Band distribution with $-2.5 \lesssim \beta \lesssim -2$ and $-1 \lesssim \alpha \lesssim 0$. Ito et al. shows that the Band-like spectra can be reproduced regardless of the viewing angle (except near the outer edge of the jet).

Ryde et al. (2011) performs a model calculation for reproducing the spectral evolution of GRB 090902B. They shows that the prompt emission of GRB 090902B consists of two components, of which spectra are represented using a Planck and Band-like distribution, respectively. The results indicate that the photospheric emission from the outflow can directly contribute to the GRB prompt emission.

Mészáros & Rees (2011) suggests that the origin of the high-energy components (from MeV to GeV) of the *Fermi*-GRBs can also be explained in the context of the photospheric model. In their analytical study, if the outflow is magnetically dominated, the high-energy emission of a GRB will originate as synchrotron radiation from a dissipative photosphere (at the radius of $\approx 10^{13}$ cm).

We should note that the synchrotron and photospheric models will provide different interpretations of the empirical correlations between observable quantities, such as the Amati-

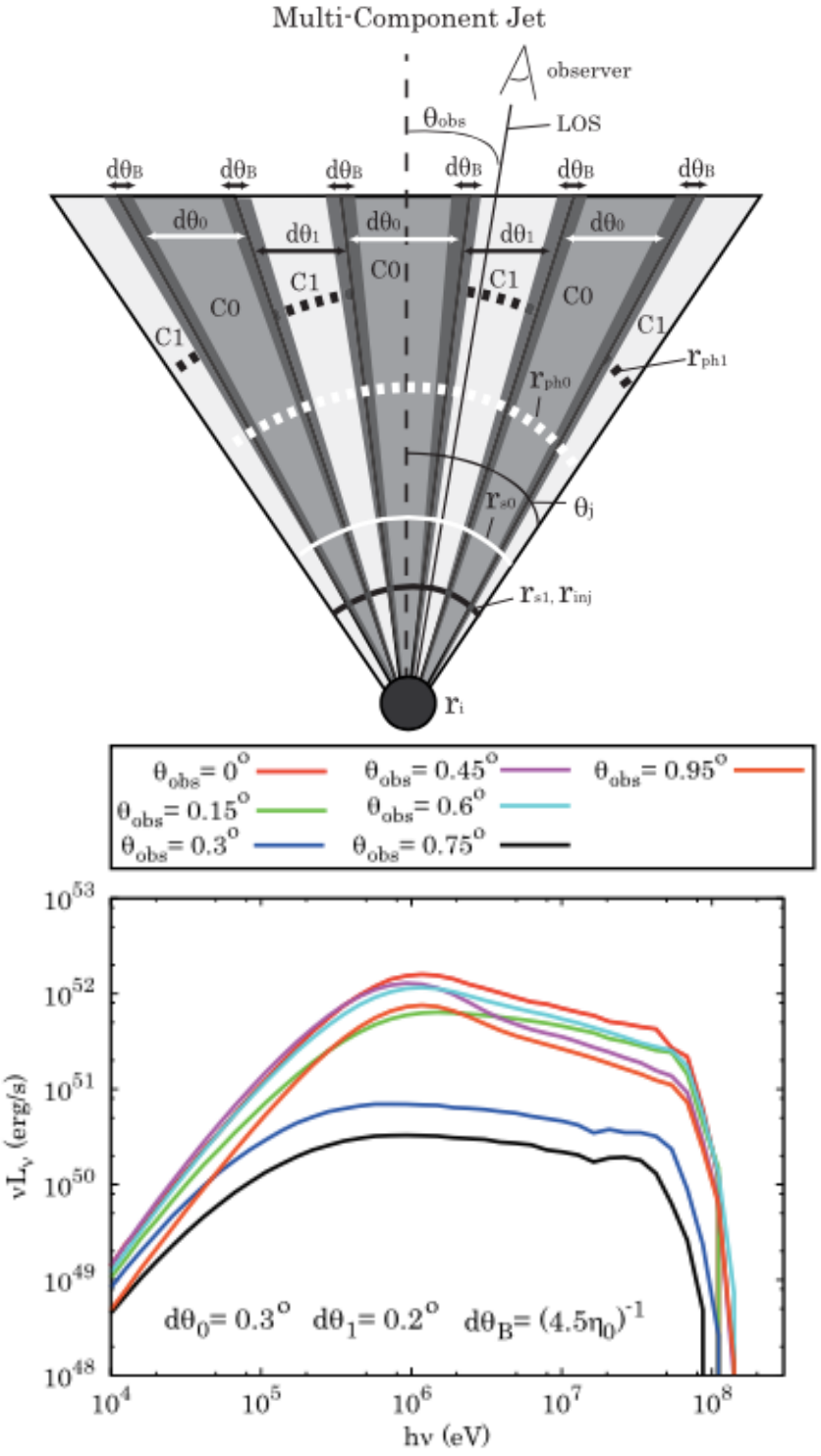

Figure 1.17: Spectra modified by electron scattering when the jet has an angular-dependent structure in terms of velocity (Ito et al., 2014). The lines also display the dependence on the increasing viewing angle with respect to the jet axis.

relation (e.g. Rees & Mészáros, 2005; Thompson et al., 2007). For example, the peak spectral energy $E_{\rm p}$ does not mean the same thing in the two models. In the synchrotron model, $E_{\rm p}$ will corresponds to the synchrotron peak,

$$E_{\rm p} \propto \Gamma^{-2} t_{\rm var}^{-1} L^{1/2}, \tag{1.42}$$

where Γ is the Lorentz factor of the outflow, $t_{\rm var}$ the variability timescale of Γ, and $L \sim L_{\rm iso}$ the luminosity (Zhang & Mészáros, 2002). In the photospheric model, $E_{\rm p}$ will nearly equal to the thermal peak,

$$E_{\rm p} \propto \Gamma k_{\rm B} T'_{\rm p} \propto \Gamma (L/\Gamma r^2)^{1/4} \propto \Gamma^2 L^{-1/4}, \tag{1.43}$$

where $T'_{\rm p} (\propto r^{-1})$ is the temperature in the co-moving frame (Rees & Mészáros, 2005). Such different dependencies (e.g. on Γ) would give hints about the expansion of the outflow.

1.6 Nature of shock breakout

The first appearance of a GRB and a CCSN must be the emergence of a shock wave from the surface of the progenitor (shock breakout), and is believed to be identified by a bright, but short electromagnetic phenomenon. Basic understanding for the process can be derived by a simple geometric explanation of the shock from the time of its birth, as follows;

First of all, due to the bounce of the central core of the progenitor star following the gravitational collapse, a shock is generated and starts propagating outward. Although there are some unsettled questions in the energy source, the shock ultimately passes through the entire region from the core to the stellar surface. At the same time, the shock also begins to give a significant fraction of the kinetic energy to the downstream electrons.The region is so thick that electrons frequently collide with other particles. They instantly convert their thermal energy into photons. While photons are co-moving with matter in the down stream of the shock as long as the shock propagates in the deep interior, they escape into the outer space when the shock approaches the stellar surface. We can estimate the moment of shock breakout from the condition that the diffusion speed of photons exceeds the speed of the shock. Since the photon diffusion speed is determined by the optical depth τ measured from infinity, the breaking out condition is expressed as a simple formula,

$$v_{\rm sh} \lesssim v_{\rm diff} = \frac{c}{\tau}. \tag{1.44}$$

Unfortunately, there are difficulties to observe a supernova in this phase; A supernova seems to suddenly appear where no sign has been found before, and it leaves the phase in a short time. The duration is determined by the light crossing time of the emission region. Thus, the emission can not last more than several hours, even if progenitor is a red-supergiant star (of which the radius $\approx 10^{13}$ cm). For these reasons, we have not discovered supernovae, which exhibited signatures of shock breakout, except for a small number of examples. The next several subsections are summary of history about studying shock breakout, i.e. some discoveries and developments.

1.6.1 Observed shock breakouts

Existence of shock breakout had long been believed since 1970's. Some former studies (e.g. Falk, 1978; Klein & Chevalier, 1978) have predicted that in general a CCSN can emit a thermal flash in the energy range of UV or X-ray. Several observations provide the evidences of shock breakout (, for example, SN 1987A, 1993J, 1999ex, SNLS-04D2dc, SNLS-06D1jd, and 2013df). In the following sections, I introduce the two most famous examples.

1.6.1.1 Ultra-violet burst from SN 1987A

On February 1987, the optical emission from SN 1987A was detected in the Large Magellanic Cloud (LMC) by the Las Campanas Observatory (Kunkel et al., 1987). (As well known, the first signature from this supernovae was detected as a burst of 24 neutrinos, about 1 day before the optical emission.) With in a day from the discovery, the photometric and spectroscopic survey began at the South African Astronomical Observatory (SAAO). Due to the broad absorption lines of hydrogen and a plateau phase, SN 1987A was classified as Type-IIP (Menzies et al., 1987; Catchpole et al., 1987). Figure 1.18 shows the light curves in optical (left panel) and UV (right panel). The rapid decreasing luminosity of the UV emission is thought to be a signature of the end of the shock breakout (Catchpole et al., 1987; Hamuy et al., 1988).

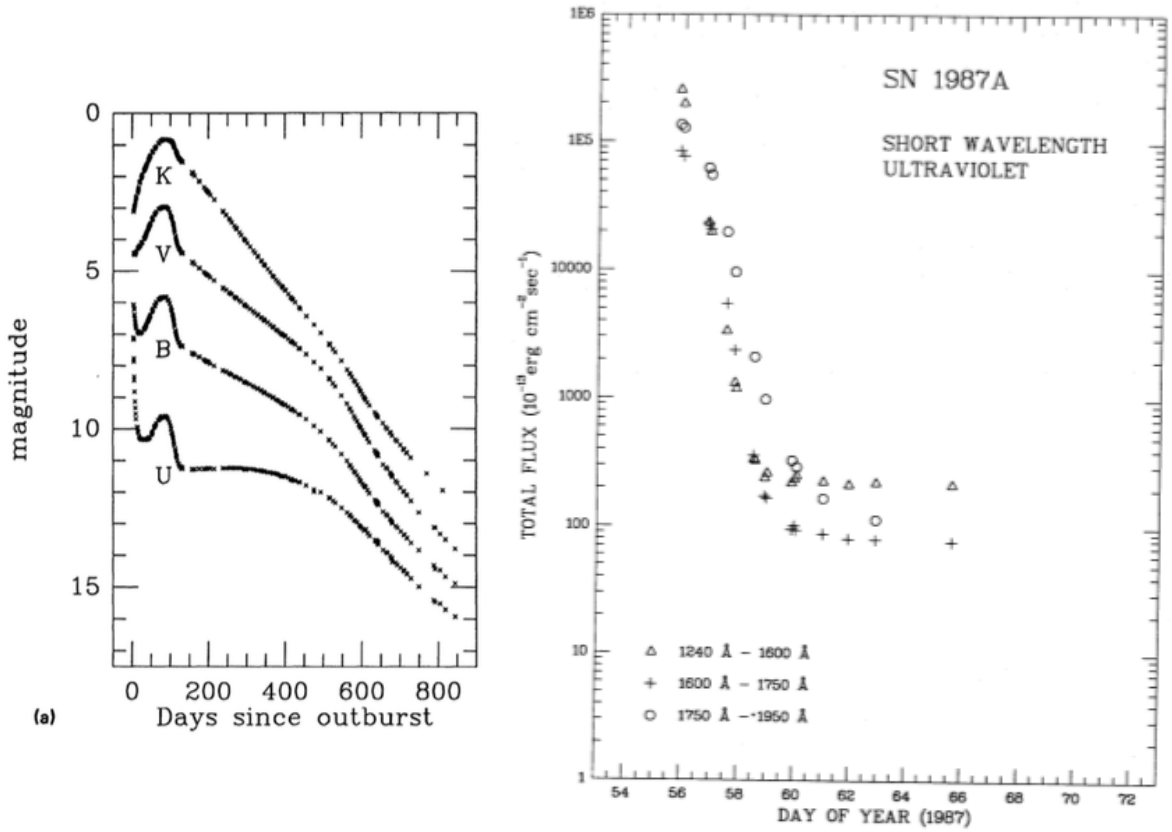

Figure 1.18: Light curves of SN 1987A optical (left panel, taken from Figure 6 of Suntzeff & Bouchet (1990)) and in UV (right panel, Kirshner et al. (1987)).

The hypothesis is supposed by another remarkable feature of SN 1987A called "light echo", detected by NASA's Hubble Space Telescope (HST) (Schaefer, 1987; Chevalier & Fransson, 1987; Crotts et al., 1992). Figure 1.19 shows the optical images in 1994 and 2014. The echo might be primary an UV emission generated by a shock propagation, and reflected by dust in the circumstellar or interstellar structure (Schaefer, 1987; Chevalier & Fransson, 1987; Crotts et al., 1992).

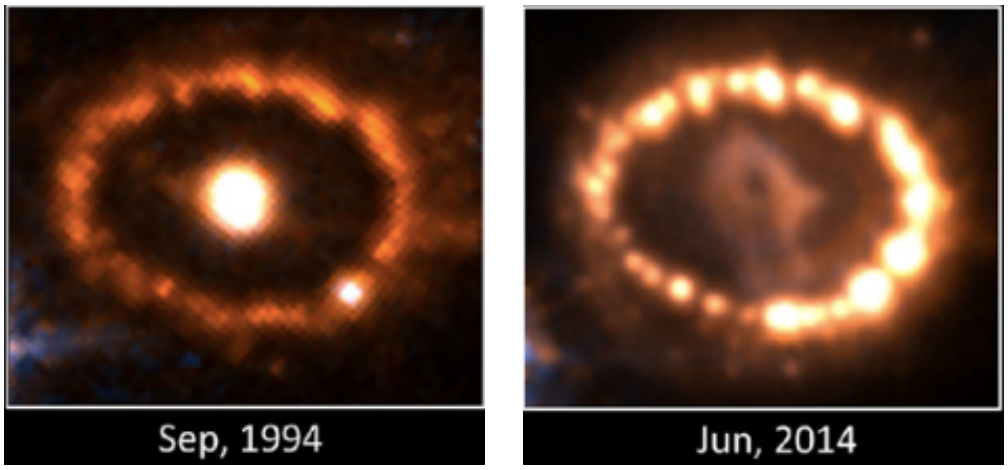

Figure 1.19: The HST B- and R-band images of SN 1987A in 1994 (left panel) and 2014 (right panel). The images are taken from Figure 1 of Fransson et al. (2015).

In the spectra of the UV emission, there are narrow emission lines of carbon, nitrogen, helium, and oxygen. Former studies (Fransson & Lundqvist, 1989; Lundqvist & Fransson, 1991, 1996) explain the origin of the lines by considering ionization of the ISM by the UV emission and recombination. For example, Lundqvist & Fransson (1996) investigates the fluxes of the emission lines as a function of the density of the ionized gas in a spherical shell (of which radius is $\approx 6 \times 10^{17}$ cm). Figure 1.20 shows a result of the model calculation for a nitrogen line, comparing with the observation. Lundqvist & Fransson indicates that in order to reproduce the evolution of the line features, the emission should generate as a blackbody radiation at peak effective temperature of 5–8^5 K. The corresponding color temperature is $(1.0–1.5)\times10^6$ K. Ensman & Burrows (1992) performs a more detailed calculation considering a couple of the hydrodynamics and radiation.

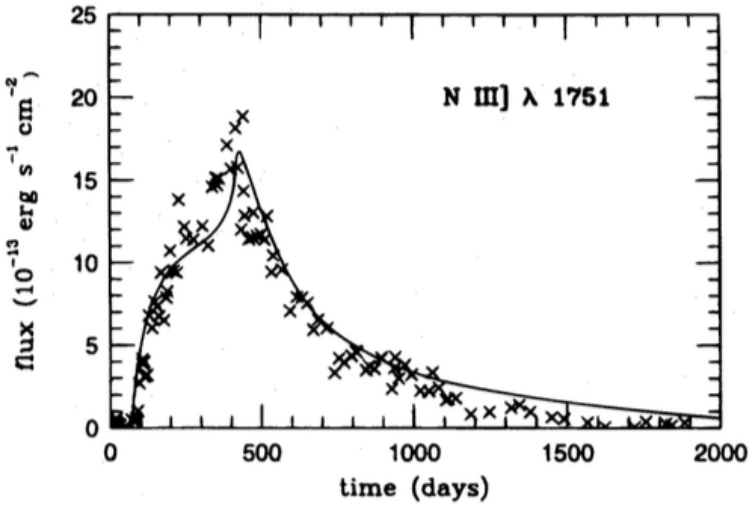

Figure 1.20: Evolution of the flux of the nitrogen emission line, in context of a Lundqvist & Fransson model aiming at reproducing the UV emission of SN 1987A.

1.6.1.2 XRO 080109/SN 2008D

The first detailed observation that could take spectroscopic data was carried out by the discovery of a luminous X-ray burst in 2008. In January, the *Swift* X-ray Telescope (XRT) suddenly detected the burst when it was in observation of a nearby spiral galaxy NGC 2770 at a distance of 27 Mpc (Soderberg et al., 2008). The X-ray burst, numbered as 080109, was lasting for about 400 s (hereafter Δt_{080109}). At this moment, the Ultraviolet/Optical Telescope (UVOT) could not find any counterpart object. In 1.4 hours after the XRT discovery, UVOT subsequently detected the counterpart both in the UV and optical bands. Furthermore, an optical follow-up observation by the Gemini North 8m telescope started within 1.7 days, and the obtained spectral features revealed that XRO 080109 was associated with a type Ibc supernova 2008D. Two left (right) corners of Figure 1.21 displays the X-ray (UV) images captured at the birth of SN 2008D (bottom) and 2 days before (top). (See appearance of the bright burst and development of the counterpart object on the right edge of the host galaxy !) Somewhat remarkably, there was no sign of the associated γ-ray emission by the *Swift* Burst Alert Telescope (BAT).

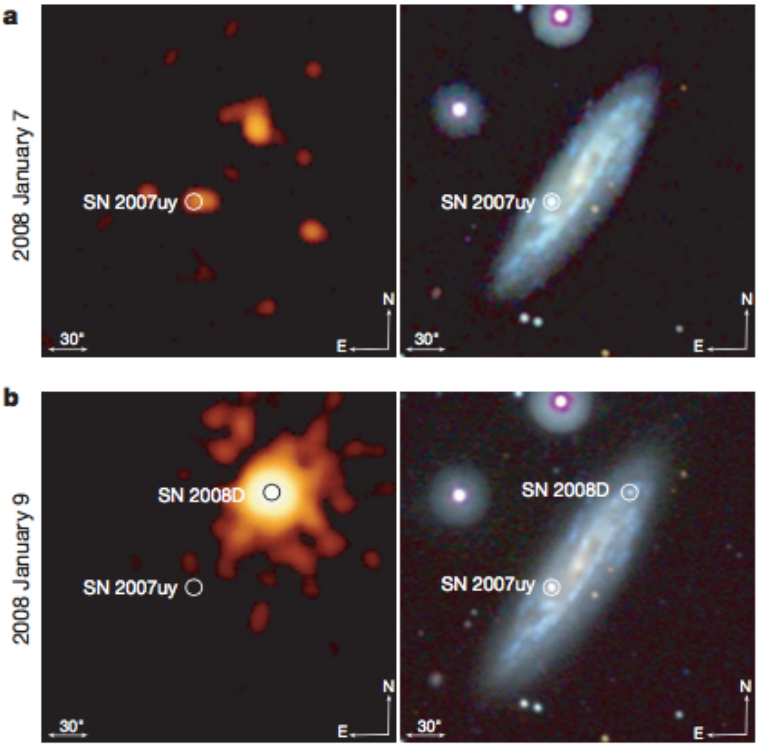

Figure 1.21: Appearance of XRO 080109/SN 2008D (top) in the spiral galaxy NGC 2770, and the comparison image taken 2 days before explosion (Soderberg et al., 2008). The left panels show the *Swift* X-ray images, and the right panels UV images.

The X-ray luminosity reaches 6×10^{43} erg s^{-1} ($=L_{p,080109}$) at its peak, and the released radiation energy until the disappearance was 2×10^{46} erg ($=E_{p,080109}$). (The properties are summarized in Table 1.2.) Figure 1.22 shows the count-rate light curve taken by the

Swift/XRT, in the energy range of [0.3-10] keV. The photon arrival rate increases in the first 70 sec and exponentially decreases to near zero in the next 500 sec. Using the duration as an indicator of the breakout radius as mentioned above, the breakout radius $R_{\mathrm{b},080109}$ of SN 2008D was estimated about $c\Delta t_{080109} \approx 10^{12}$ cm, which is one magnitude order larger than the typical radius of a Wolf-Rayet star. Meanwhile, results of the spectral and light curve (in UV, opt) analysis strongly indicate that the progenitor of SN 2008D was a ordinary Wolf-Rayet star. For this reason, Soderberg et al. concludes that the X-ray burst must originate from a shock passing through the dense circumstellar wind, rather than the progenitor surface.

Table 1.2: Properties of XRO 080109/SN 2008D (see also in text).

Date	UT	Δt_{080109}	$L_{p,080109}$	E_{080109}
2008-01-09	13:32:49	~400 sec	6×10^{43} erg s^{-1}	2×10^{46} erg

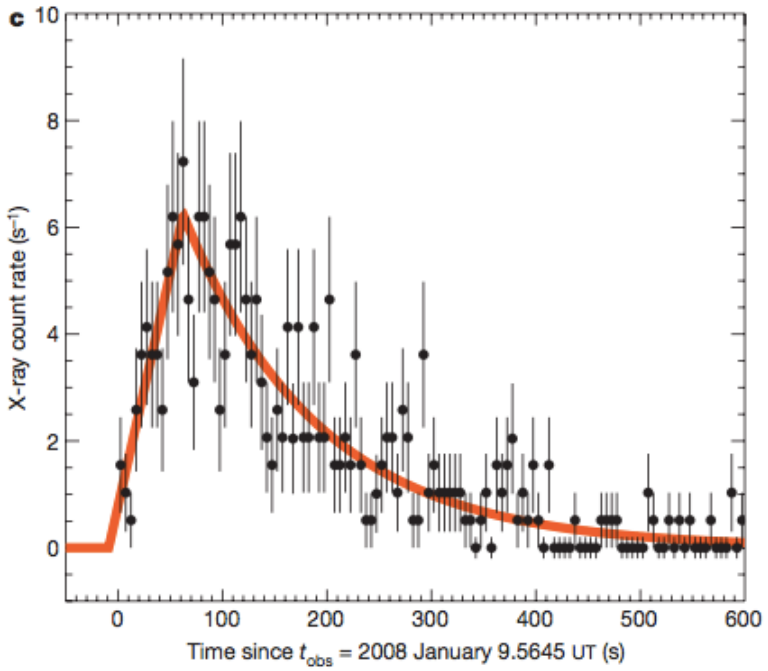

Figure 1.22: Light curve of XRO 080109 in energy range of [0.3:10] keV (Soderberg et al., 2008).

Non-thermal spectrum and bulk Comptonization Figure 1.23 displays the X-ray count-rate spectrum and two types of numerical fitting for the data (lines). The top panel shows the best-fit power-law energy distribution with the exponent $\beta_{080109} = 2.3 \pm 0.3$, in which χ^2=7.5 for the degree of freedom (df) of 17 and the probability $P = 0.98$. The bottom panel shows the blackbody form with the temperature $kT = 0.71 \pm 0.08$ keV, in which the residual is $\chi^2 = 26.0$ for $df = 17$ and $P = 0.074$. Thus, it is clear that the power-law model is much more suitable for the observed spectrum. This means some non-thermal

mechanisms can significantly affect the emission. Soderberg et al. suggested scattering of photons between the ejecta and the circumstellar medium (CSM) as the origin of the non-thermal component (bulk Comptonization).

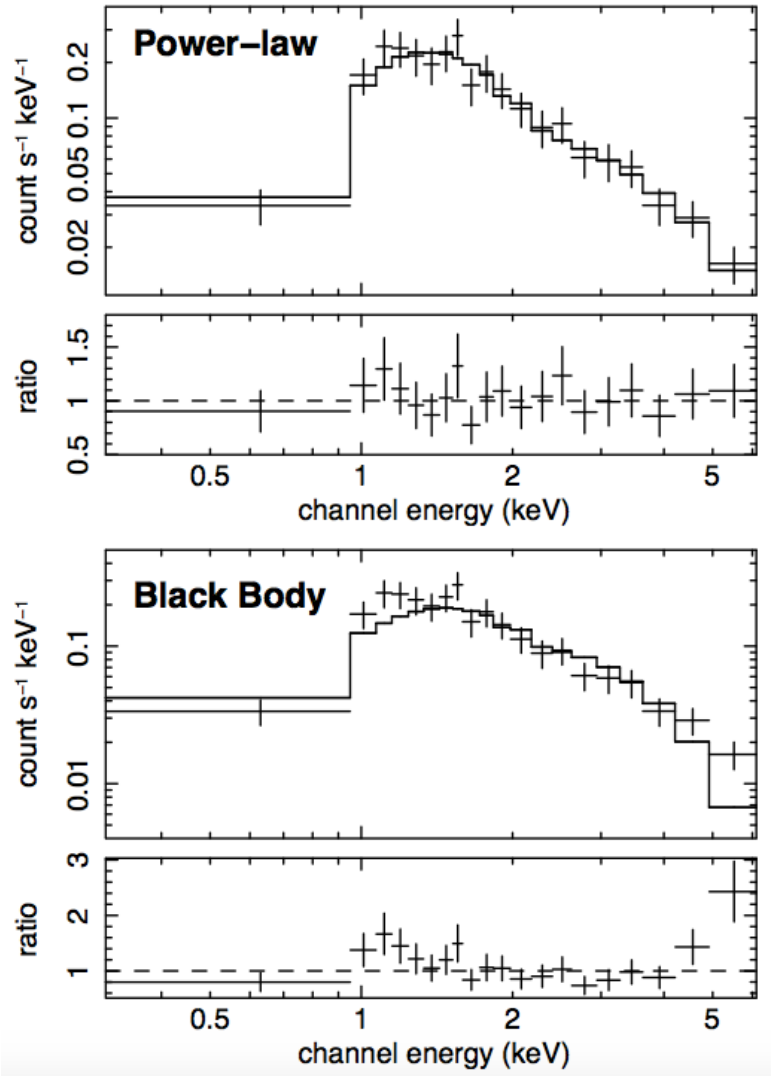

Figure 1.23: X-ray spectra of XRO 080109 (plus signs) (Soderberg et al., 2008). The top panel also displays the best-fit power-law model with the exponent $\beta_{080109} = 2.3 \pm 0.3$ (χ^2=7.5, $df = 17$, $P = 0.98$) in the solid line, and the bottom panel the blackbody model with the temperature $kT = 0.71 \pm 0.08$ keV ($\chi^2 = 26.0$, $df = 17$, $P = 0.074$).

Figure 1.24 shows a simple image of how a photon moves across the shock front (color) and how the photon energy changes during the travel (gray). Here we assume that the pre- and post-shock regions are filled with large number of electrons and optically thick. If we observe electrons in the co-moving frame, they would move in random directions on either side of the shock. Electrons in the post-shock move in the observer frame with the bulk kinetic energy. Therefore, when a photon meets these electrons, it can obtain the bulk energy during inverse Compton scattering in the observer frame.

To investigate whether bulk Compton scattering mechanism can indeed reproduce the observed X-ray spectral feature, Suzuki & Shigeyama (2010a) made radiative transfer simulations by using a non-relativistic hydrodynamic description of Sakurai (1960) for a shock propagating through a stellar surface. In the simulations, they isotropically emit thermal photons with a temperature of 0.1 keV at the position of the shock, propagating at a velocity of $V_{\rm i} = (0.1 \sim 0.4)c$ at the moment of breakout. Figure 1.25 shows their resultant spectra. As long as the initial velocity $V_{\rm i}$ is smaller than $\sim 0.3c$, the larger $V_{\rm i}$ lead to the stronger effect of bulk-Compton scattering on the spectral hardening. When $V_{\rm i} = 0.3c$, a power-law model with the index of about -2.4 represents the resultant energy distribution over the observed energy range of [1-7] keV quite well(see Figure 3 in their article, if necessary). Since the difference of the spectral hardening effect between the case of $V_{\rm i} = 0.3c$ and $0.4c$ is little, both of the 2 spectra for $V_{\rm i} \geqslant 0.3c$ can reproduce the observed X-ray burst.

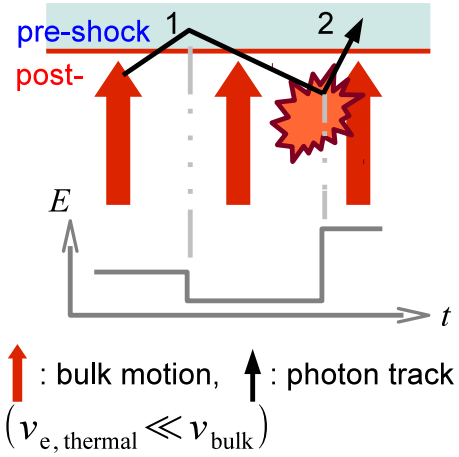

Figure 1.24: Schematic view of the bulk Compton scattering (color) and energy change of a photon (gray).

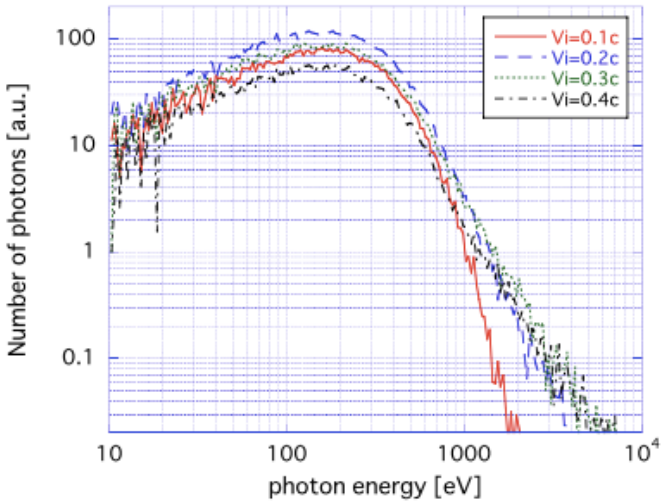

Figure 1.25: Influence of bulk-Compton scattering on a thermal spectrum, indicated by radiative transfer simulations of Suzuki & Shigeyama (2010a). The results for the 4 different shock velocity at breakout ($V_{\rm i}$) indicates that when $V_{\rm i} \geqslant 0.3c$, it is possible to interpret the spectral feature of XRO 080109 as a evidence of bulk-Compton scattering.

Influence of shock asymmetry on emission According to Suzuki & Shigeyama (2010b), there seems a sign of shock asymmetry in the light curve of XRO 080109. They calculate the behavior of the shock wave until it emerges from the stellar surface, having the initial condition of the radial velocity component $v_{\rm in}$ in the form of

$$v_{\rm in}(\theta) = \sqrt{\frac{2E_{\rm exp}}{4\pi r_{\rm in}^2 \Delta r_{\rm in} \rho_{\rm in}}} \frac{1 + \alpha\cos(2\theta)}{1 - 2\alpha/3 + 7\alpha^2/15}, \tag{1.45}$$

where θ is the angle measured from the symmetry axis, $E_{\rm exp}$ the energy released by the explosion. The radius $r_{\rm in}(\simeq 10^8)$ cm and the mass density $\rho_{\rm in}$ at the inner boundary are derived by the progenitor model of Shigeyama & Nomoto (1990). The parameter α represents the degree of asymmetry (when $\alpha = 0$, the shock is spherically symmetric).

The results of their calculation indicate that when $E_{\rm exp} = 10^{51}$ erg, the shock reaches the velocity of $0.3c$ at the stellar surface, and the emergence time $T_{\rm em}$ is well approximated by a function of θ and α (from 0 to 0.8) as follows,

$$T_{\rm em}(\alpha, \theta) = 65\alpha(1 + 3.6\alpha)(\sin^2\theta - 0.2\sin^4\theta). \tag{1.46}$$

Figure 1.26 displays the θ-dependence of the emergence times for α =0, 0.2, 0.5, and 0.8.

Using the above profile, they investigate the dependences of the the light curves on the degree of asymmetry and the direction of the observer's location Θ (relative to the symmetry axis). In their calculation, photons are produced from a blackbody at temperature of $\sim 10^6$ K. Photons are emitted after the shock reaches a radius $R_{\rm b} \sim 3 \times 10^{12}$ cm for the following 40 sec. All photons are assumed to continue traveling without interaction, until detected by an observer at a radius $D = 100R_{\rm b}$.

As a result, Figure 1.27 shows the light curves for Θ =0, 30, 60, and 90 deg when $\alpha = 0.5$. When the observer is on-axis (, Θ is close to 0 deg), the luminosity increases rapidly during 40 sec after the onset, then increases more slowly until it peaks at $\approx$ 200 sec later. Finally, the luminosity decreases rapidly to zero within $\approx$ 40 sec. The behavior is explained by considering the shock emergence time and the light crossing time. The rapid increase and decrease of 40 sec corresponds to broadening and shrinking of the photosphere. During the slow increasing phase, firstly, photons produced at location angles $\theta \approx 0$ deg come, then secondary, those of $\theta \approx 90$ deg gradually appears. On the contrary, when the observer is off-axis (, $\Theta \sim 90$ deg), the behavior of the luminosity evolution seems very different. It reaches the peak within 40 sec after the onset, then decreases during the subsequent 120 sec. This is because the photons produced at location angles $\theta \approx 0$ deg are generated ~ 70 sec earlier than those of $\theta \approx 90$ deg, but being $\approx R_{\rm b}$ longer distant measured the observer. In this case, most of photons reach the observe within almost same period of time.

By comparing the results with XRO 080109, Suzuki & Shigeyama claims that the shape of the light curve of the outburst is similar to the axisymmetric model with $\alpha = 0.5$ and $\Theta = 90$ deg.

1.7 Ultra-relativistic shock breakout at the surface of a Wolf-Rayet star

In principle, a shock in a supernova progenitor can breakout with the velocity larger than 99% of the speed of light, as ensured by the existence of GRBs. In an ultra-relativistic shock, bulk-Comptonization becomes more significant than in a mildly-relativistic circumstance, so photons must have energies of γ-ray.

Nakar & Sari (2010, 2012) investigate how the luminosity of thermal emission evolutes as a results of the shock propagating with relativistic velocities. Their calculations deal with an entire event of supernova explosion, from shock breakout at ultra-relativistic velocities to the period of non-relativistic, spherical expansion. Using self-similar solutions constructed by Johnson & McKee (1971); Tan et al. (2001); Pan & Sari (2006), they describe the evolution of the planar shock before and after the breakout. In order to calculate the light curve, they pays a great attention to estimation of the photon temperature and opacity, by considering the influence of particle interactions (such as free-free emission, inverse Compton scattering, and energy loss due to the processes) averaged over photon energies. Regardless of that, Nakar & Sari does not calculate the bulk-Comptonization on spectrum shape.

In my former study, I focus on the change of spectral shape due to bulk-Comptonization (Ohtani et al., 2013). In the study, the dynamics of the shock is described using a self-similar solution constructed by Nakayama & Shigeyama (2005). Note that in the Nakayama & Shigeyama solution, the temporal evolution of the shock Lorentz factor is solely determined by the density distribution of the atmosphere and independent of the central engine activity. The resultant spectrum consists of two remarkable components; the lower energy one is a integration of Doppler shifted blackbody, and higher energy one is the bulk component.

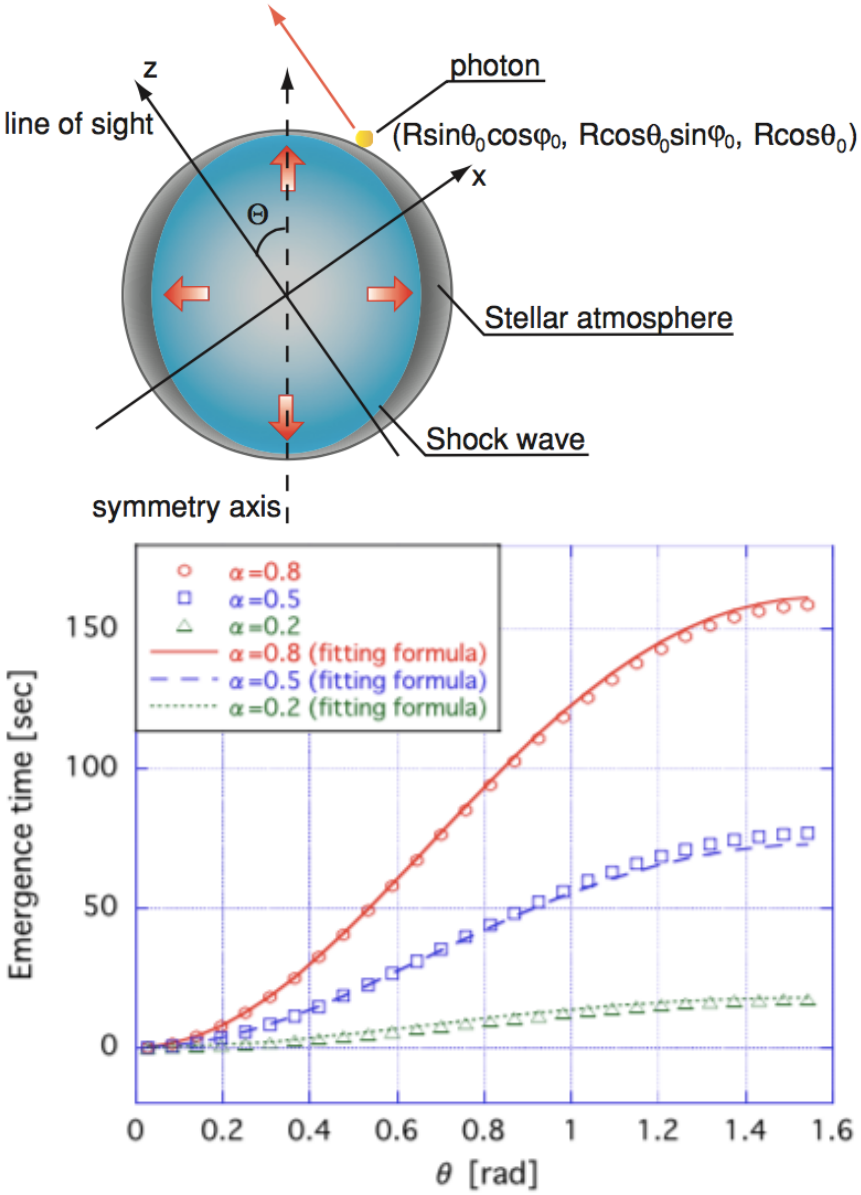

Figure 1.26: Schematic view of an axisymmetric shock (top) and the emergence time in directions of 0 rad$< \theta < \pi/2$ rad (bottom) when the explosion energy $E_{\rm exp} = 10^{51}$ erg (Suzuki & Shigeyama, 2010b).

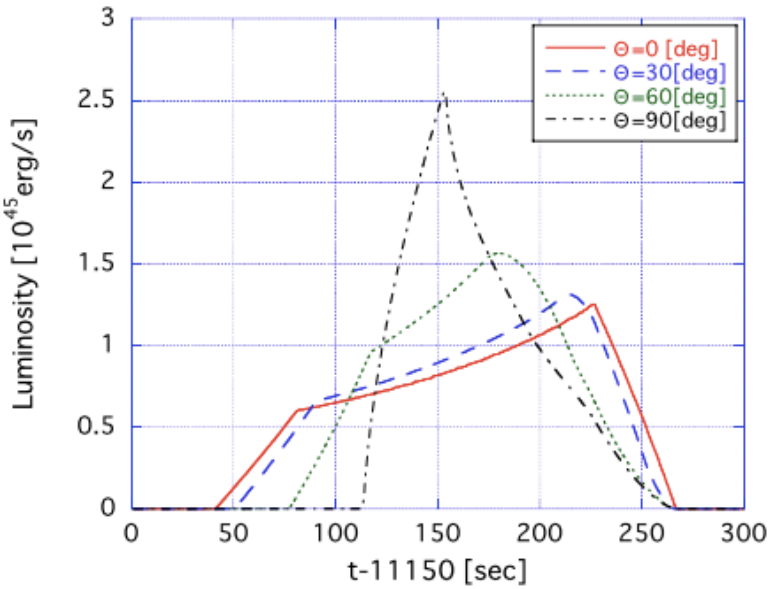

Figure 1.27: Influence of the shock asymmetry ($\alpha = 0.5$) and the viewing angle Θ on the light curve of the thermal emission (Suzuki & Shigeyama, 2010b). When $\Theta \approx 0$ deg, photons produced near the symmetry axis ($\theta \approx 0$ deg) form the first part ($t - 11150$ sec$\lesssim$150 sec) and those of $\theta \approx$90 deg the second part (150 sec$\lesssim t - 11150$ sec). On the other hand, when $\Theta \approx 90$ deg, the luminosity peaks rapidly because the time delays of photon generating (equal to the shock emergence times ~ 70 sec) for $\theta \approx$90 deg begin competing with the light crossing time across the stellar surface ($= R_b/c \approx 100$ sec).

Chapter 2

Ultra-relativistic shock breakout at the stellar surface

Is there any relations between shock breakout emission and long-GRBs ? To investigate that, it is necessary to calculate bulk-Comptonization on thermal photons generated from a Wolf-Rayet star. First of all, I calculate propagation of γ-ray photons owing to an ultra-relativistic shock passing through the stellar surface. [1].

Due to the large density gradient, the shock must accelerate. The behavior is described by a self-similar solution constructed by Nakayama & Shigeyama (2005). In order to calculate the radiation transfer in the matter with ultra-relativistic velocities, I construct a Monte-Carlo code in which Lorentz transformation is fully taken into account.

2.1 Hydrodynamics

The hydrodynamical evolution is described by a self-similar solution constructed by Nakayama & Shigeyama (2005). [2] Here I summarize the procedure to obtain the solutions. Before the shock propagation, the density distribution in the surface later of a star is expressed in terms of the distance x measured from the stellar surface,

$$\rho = \begin{cases} bx^{\delta} & x \geqslant 0, \\ 0 & x < 0, \end{cases} \tag{2.1}$$

where $x > 0$ in the star. The atmosphere is assumed to be plane-parallel. The index δ equals 3 for radiative atmosphere.

In the relativistic limit, basic equations governing the plane-parallel fluid can be approx-

[1] This chapter was published in the Astrophysical Journal (2013) by Ohtani, Suzuki, & Shigeyama

[2] The derivation of the basic equations of fluids is described in Appendix B.

imated by the following equations.

$$\frac{d}{dt}\left(p\gamma^4\right) = \gamma^2\frac{\partial p}{\partial t}, \tag{2.2}$$

$$\frac{d}{dt}\ln\left(p^3\gamma^4\right) = -4\frac{\partial \beta}{\partial x}, \tag{2.3}$$

$$\frac{d}{dt}\left(pn^{-4/3}\right) = 0, \tag{2.4}$$

where γ is the Lorentz factor, β the velocity in units of c, p the pressure, and n the number density.

When the subscript 1 and 2 denote the pre- and post-shock, the boundary conditions at the shock front with a Lorentz factor Γ are written as follows.

$$p_2 = \frac{1}{3}e_1 = \frac{2}{3}\Gamma^2\omega_1, \tag{2.5}$$

$$n_2' = 2\Gamma^2 n_1, \tag{2.6}$$

$$\Gamma^2 = 2\gamma^2, \tag{2.7}$$

where e is the energy density, $w = e + p$ the enthalpy, and $n_2' = n_2\gamma$ the density measured in the observer frame.

Then, I introduce a similarity variable χ defined by

$$\chi = [1 + 2(m+1)\Gamma^2]\left(1 + \frac{x}{t}\right), \tag{2.8}$$

changes with time t as

$$\Gamma^2 = B_{\rm sh}(-t)^{-m}. \tag{2.9}$$

Here, the shock reaches the stellar surface at $t = 0$, so the solutions can be obtained in the range of $t \lesssim 0$.

When $\chi = 1$, the position x corresponds to the shock front ($x = X_{\rm s}$). Instead of p, γ, and n, non-dimensional functions $f(\chi)$, $g(\chi)$, and $h(\chi)$ are introduced as

$$p = \frac{2}{3}bX_{\rm s}^{\delta}\Gamma^2 f(\chi), \tag{2.10}$$

$$\gamma^2 = \frac{1}{2}\Gamma g(\chi), \tag{2.11}$$

$$n' = 2\frac{b}{\mu}X_{\rm s}^{\delta}\Gamma^2 h(\chi), \tag{2.12}$$

following Blandford & McKee (1976). The the boundary conditions become $f(1) = g(1) = h(1) = 1$.

Then the coordinate system is transformed from (t, x) to (Γ, χ) by using

$$t\frac{\partial}{\partial t} = -\frac{m\Gamma}{2}\frac{\partial}{\partial \Gamma} + (m+1)(2\Gamma^2 - \chi)\frac{\partial}{\partial \chi}, \tag{2.13}$$

$$t\frac{\partial}{\partial x} = 2(m+1)\Gamma^2\frac{\partial}{\partial \chi}, \tag{2.14}$$

$$t\frac{d}{dt} = -\frac{m\Gamma}{2}\frac{\partial}{\partial \Gamma} + (m+1)\left(\frac{2}{g} - \chi\right)\frac{\partial}{\partial \chi}. \tag{2.15}$$

By using Equations (2.10)–(2.12) and (2.13)–(2.15), the basic equations (2.2) and (2.3) ultimately result in

$$\frac{1}{g}\frac{d\ln f}{d\chi} = \frac{(\delta - m)g\chi + 8m - 4\delta}{(m+1)(g^2\chi 2 - 8g\chi + 4)}, \tag{2.16}$$

$$\frac{1}{g}\frac{d\ln g}{d\chi} = \frac{-mg\chi + 7m - 3\delta}{(m+1)(g^2\chi 2 - 8g\chi + 4)}, \tag{2.17}$$

$$\frac{1}{g}\frac{d\ln h}{d\chi} = \frac{(m-\delta)g^2\chi^2 + (8\delta - 10m)g\chi + 18m - 10\delta}{(m+1)(2 - g\chi)(g^2\chi 2 - 8g\chi + 4)}. \tag{2.18}$$

Note that the denominators of Equations (2.16)–(2.18) become 0 at $g\chi = 4 - 2\sqrt{3}$. The numerator should simultaneously become 0, indicating that m has the eigen values,

$$m = (\mp 2\sqrt{3} - 3)\delta. \tag{2.19}$$

The negative m is forbidden, because $\Gamma \to \infty$ when $X_{\rm s} \to 0$. Therefore,

$$m = (2\sqrt{3} - 3)\delta, \tag{2.20}$$

and Equations (2.16)–(2.18) become

$$\frac{1}{g}\frac{d\ln f}{d\chi} = \frac{-2\delta}{[2 + \sqrt{3}(\delta+1)](g\chi - 4 - 2\sqrt{3})}, \tag{2.21}$$

$$\frac{1}{g}\frac{d\ln g}{d\chi} = \frac{-\sqrt{3}\delta}{[2 + \sqrt{3}(\delta+1)](g\chi - 4 - 2\sqrt{3})}, \tag{2.22}$$

$$\frac{1}{g}\frac{d\ln h}{d\chi} = \frac{-2\delta(g\chi - 4\sqrt{3})}{(-g\chi + 2)[2 + \sqrt{3}(\delta+1)](g\chi - 4 - 2\sqrt{3})}. \tag{2.23}$$

I solve the above three equations in the range of $0 < \chi \leqslant 1$ by using the Runge-Kutta method.

2.1.1 Parameter determination

In order to obtain the density profile and the shock behavior, it is necessary to select the parameters b and $B_{\rm sh}$ defined in Equation (2.1) and (2.9).

The optical depth of the pre-shock region is expressed by

$$\tau = \frac{\sigma_{\rm T}}{\mu m_{\rm H}} \int_0^{X_{\rm s}} b x^{\delta} dx = \frac{\sigma_{\rm kl} b X_{\rm b}^{\delta+1}}{(\delta+1)\mu m_{\rm H}}, \tag{2.24}$$

where μ is the mean molecular weight and $m_{\rm H}$ the mass of a hydrogen atom.

Therefore, when $X_{\rm s} = X_{\rm b}$ at the moment of breakout ($t = t_{\rm b}$),

$$b = \frac{(\delta+1)\mu m_{\rm H}}{\sigma_{\rm T} X_{\rm b}^{\delta+1}} \times \tau. \tag{2.25}$$

When considering a WC star, $\mu = 2$ because the number of electrons per nucleon is

$$\frac{\rm Z_O}{A_{\rm O} m_\mu} = \frac{1}{2} \quad (= \mu^{-1}), \tag{2.26}$$

where $Z_{\rm X}$ and $A_{\rm X}$ denote the atomic number and mass number of element X.

Since the shock velocity $V_{\rm s}$ is close to c at $t = t_{\rm b}$, the optical depth should be $\tau \approx 1$. However, in order to estimate the influence of bulk Comptonization, it is necessary to calculate the radiative transfer of photons which scattered at least several times before escape from the star. For this reason, I determine the density distribution so that the optical depth of the pre-shock region is relatively large ($\tau = 3$) for high-energy photons (5 times higher than the average energy of the blackbody emitted from the shock front at $t = t_{\rm b}$).

The parameter $B_{\rm sh}$ is determined when the two factor is given; the position of the shock front $X_{\rm b}$ and shock Lorentz factor $\Gamma_{\rm b}$ at $t = t_{\rm b}$,

$$B_{\rm sh} = \Gamma_{\rm b}^2 (-t)^m. \tag{2.27}$$

Because of the high temperature ($> 10^6$ K), the radiation pressure is the dominant force in comparison to the gas pressure. Thus, the temperature $T_{\rm s}$ of the shock is expressed by

$$T_{\rm s} = \left(\frac{3p}{a}\right)^{1/4} = \left(\frac{2 b X_{\rm s}^3 \Gamma^2}{a}\right)^{1/4}, \tag{2.28}$$

where a is the radiation constant. Figure 2.1 displays the evolution of the Lorentz factor, number density, and temperature at the shock front, when $X_{\rm b} = 10^7$ cm and $\Gamma_{\rm b} = 100$.

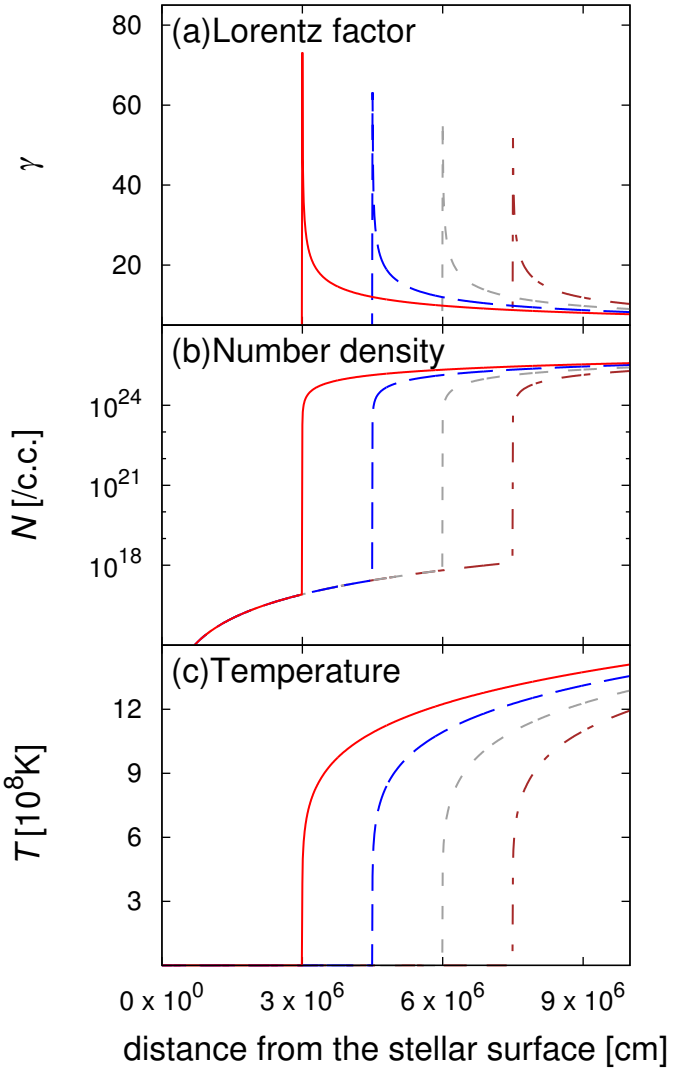

Figure 2.1: Evolution of the Lorentz factor, number density, and temperature at the shock front propagating through the stellar surface, in the case of $X_{\rm b} = 10^7$ cm and $\Gamma_{\rm b} = 100$. Each line shows the profile at time 2.5×10^{-4} s (brown dash-dotted line), 1.5×10^{-4} s (gray short-dashed line), 2.0×10^{-4} s (blue long-dashed line), and 1.0×10^{-4} s (red solid line) in the observer frame.

2.2 Radiative processes

Due to the terms of scattering, the radiation transfer equation (witten in Pomraning 1973) has a complex expression, which contain both integral and differential functions. Furthermore, photon has 6 degrees of freedom in space, consisting of three in the location and three in the momentum. In order to solve the equation, I use a Monte-Carlo method.

The calculation is roughly divided into the following processes.

1. Generation of seed photons (blackbody)
2. Estimation of the mean free path
3. Calculation of scattering in the electron co-moving frame

Since I used the principle parts of the Monte-Carlo calculation throughout the thesis (Chapter 2, 3, and 4), I described all of the processes of the code in this section. Before the description, I summarize the peculiar points in setting of this study in the following section.

2.2.1 Conditions

The following list describes the setup for Monte-Carlo calculations.

- Only inverse-Compton scattering is taken into consideration, because
  - the effective optical depth of the pre-shock region $\tau_* = \sqrt{\alpha_\nu^{\rm ff}(\alpha_\nu^{\rm ff} + \bar{n}_{\rm e}\sigma_{\rm kl})}X_{\rm b}$ will become significantly smaller than 1 when $T \approx 10^4$ K. For example, even the photon energy is as low as 100 keV ($\alpha_\nu^{\rm ff} \lesssim 1.7 \times 10^{-16}$ cm^{-1}), $\tau_* \lesssim 10^{-12}X_{\rm b} \ll 1$ where $X_{\rm b}$ in cm.
- The photosphere is located at the shock front.
- I assume that when a photon enters the shock, it immediately scatters off an electron at the shock front.
- The angular aperture of a jet is 10 deg. The angle is determined by referring the former analysis of observed GRBs (e.g. Frail et al., 2001; Ghirlanda et al., 2004; Fong et al., 2012).
- The light curve and spectrum are presented for several pairs of the shock Lorentz factor $\Gamma_{\rm b}$ and the distance $X_{\rm b}$ between the shock front the stellar surface at the moment of breakout.

Figure 2.2 and 2.3 show the outlines of the Monte-Carlo simulation.

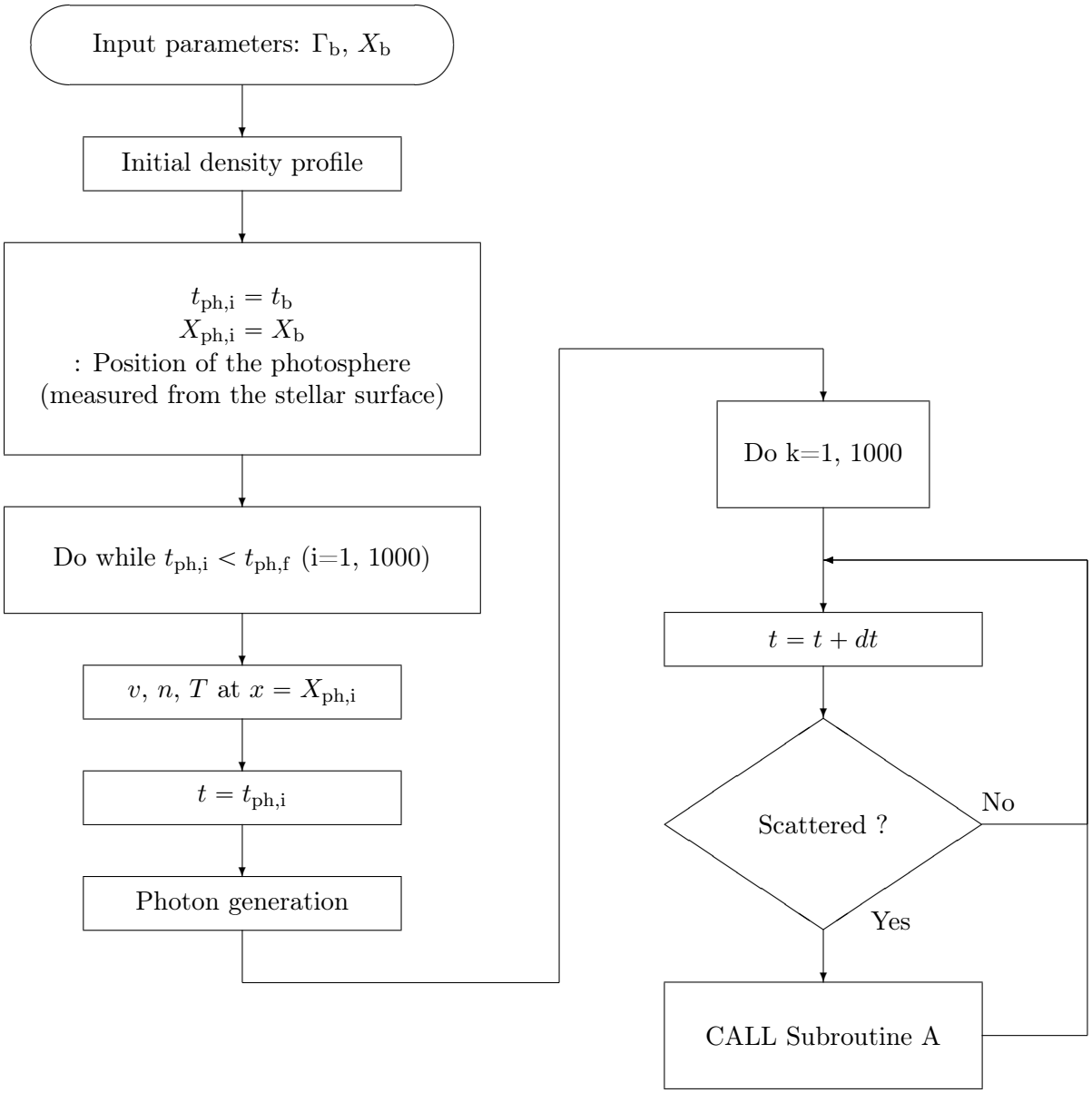

Figure 2.2: Flowchart of the Monte-Carlo simulation used for ultra-relativistic shock breakout at the stellar surface. Note that x denotes the distance measured from the stellar surface. Subroutine A is defined in Figure 2.3.

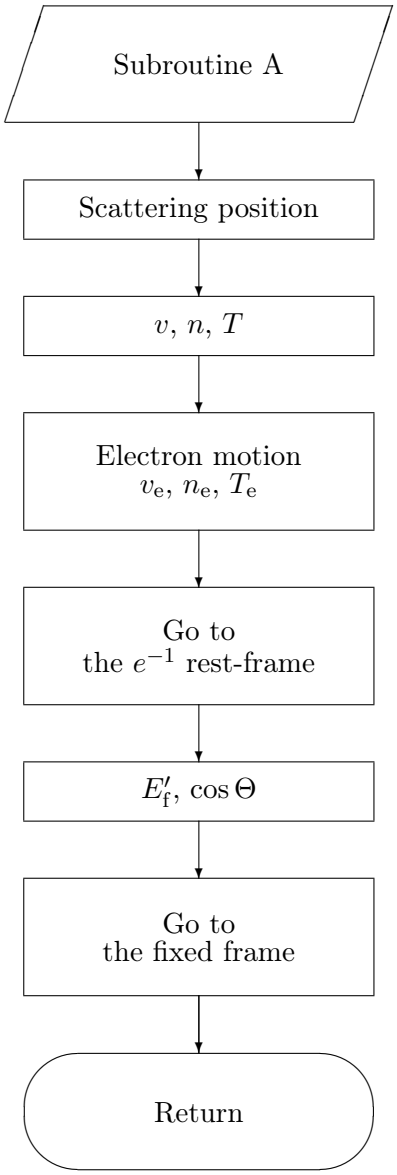

Figure 2.3: Subroutine A.

2.2.2 Photon generation

At the start of calculations, thermal photons at a temperature of T are generated from the photosphere.

In the rest-frame of the fluid, the energy distribution of photons ϵ' follows the Planck function,

$$B_{\rm ph}(\epsilon') = \frac{2}{h^3c^2}\frac{\epsilon'^2}{\exp(\epsilon'/k_{\rm B}T)-1}, \tag{2.29}$$

where h is the Planck constant and $k_{\rm B}$ the Boltzmann constant. In order to determine the initial energy of a seed photon, I define a non-dimensional energy $x_{\rm ph} = h\nu/k_{\rm B}T$, then generate two random numbers $0 < R_1 < 20x_{\rm ph}$ and $0 < R_2 < x_{\rm ph}^2/[\exp(x_{\rm ph})-1]$. The initial photon energy becomes $x = R_1$, if R_1 and R_2 satisfy $R_2 < R_1^2/[\exp(R_1)-1]$.

The total number of seed photons is 10^6. The number of photons generated in a volume V is

$$N_\nu = \frac{V}{\pi^2c^3}\int_0^\infty B_{\rm ph}d\epsilon \propto \frac{{k_{\rm B}}^3T^3}{\pi^2h^3c^3}V\int_0^\infty \frac{x^2}{e^x-1}dx = \frac{2{k_{\rm B}}^3T^3}{\pi^2h^3c^3}V\zeta(3), \tag{2.30}$$

where $\zeta(3) = \Sigma_{n=1}^{\infty}1/n^3 \approx 1.202$ denotes the Riemann zeta function.

The momentum of each photon is specified by defining the direction using the inclination angle θ' and the azimuth angle ϕ'. Since the photons should be emitted isotropically in the co-moving frame at the moment of generation, I determine the values of (θ', ϕ') as

$$\theta' = \arccos(R_3), \qquad \phi' = R_4, \tag{2.31}$$

where $R_{3,4}$ are the random numbers in the ranges of $-1 < R_3 < 1$, $0 < R_4 < 2\pi$. The angles (θ, ϕ) in the observer frame are derived by using a Lorentz transformation. Since the velocity of the shock is mildly-relativistic, the number of photons moving outward from the star tends to be several tens percent larger than that of photons moving inward.

2.2.3 Electron distribution

The momentum of a relativistic electron is derived in a similar way as photons. The distribution of their kinetic energies are represented by the Maxwell-Boltzmann distributions in the rest-frame of the fluid,

$$f_{\rm e} = C_{\rm e}\exp\left[-\frac{p_{\rm e}^2}{2m_{\rm e}k_{\rm B}T_{\rm e}}\right], \tag{2.32}$$

where $p_{\rm e}$ is the momentum, $m_{\rm e}$ the rest mass, and $T_{\rm e} = T$ the temperature of an electron. The coefficient $C_{\rm e}$ should be determined by the normalization. The total electron number $n_{\rm e}$ should equal the integration $4\pi C_{\rm e} \int f_{\rm e} d^3p$, so

$$C = (2\pi m_e k_{\rm B} T_e)^{\frac{3}{2}}. \tag{2.33}$$

Here, I generate the random numbers $-3\sqrt{2m_{\rm e}k_{\rm B}T_{\rm e}} < R_5 < 3\sqrt{2m_{\rm e}k_{\rm B}T_{\rm e}}$ and $0 < R_6 < 1$. If $R_6 < {R_5}^2 \exp\left[-{R_5}^2/2m_e k_{\rm B} T_e\right]$, the momentum p equals R_5.

The direction of motion $(\theta_{\rm e}, \phi_{\rm e})$ are determined in exactly the same way as photons.

2.2.4 Interactions

Firstly, I calculate the possibility P for electron scattering of a photon traveling a short distance (dl). The scattering cross section is given by the Klein-Nishina formula

$$\begin{aligned} \sigma_{\rm kl} \quad &= \sigma_T \cdot \frac{3}{4} \left[\frac{1+x_{\rm ph}}{x_{\rm ph}^3} \left\{ \frac{2x_{\rm ph}(1+x_{\rm ph})}{1+2x_{\rm ph}} - \ln(1+2x_{\rm ph}) \right\} \right. \\ &\left. + \frac{1}{2x_{\rm ph}} \ln(1+2x_{\rm ph}) - \frac{1+3x_{\rm ph}}{(1+2x_{\rm ph})^2} \right], \end{aligned} \tag{2.34}$$

where $x_{\rm ph} \equiv h\nu/mc^2$. The scattering possibility is written as follows.

$$P = 1 - \exp(-\tau^n), \tag{2.35}$$

where $\tau^n = \sigma_{\rm kl} n_{\rm e} c dt$ denotes the optical depth for the photon path.

Furthermore, the probability of free-free absorption is characterized by the following coefficient $\alpha_\nu^{\rm ff}$, when the photon with an energy ϵ' travels in a gas composed of ions with the atomic number Z.

$$\alpha_\nu^{\rm ff} = 3.7 \times 10^8 T^{-1/2} Z^2 n_{\rm e} n_{\rm i} \nu^{-3} (1 - e^{-\epsilon'/k_{\rm B}T}) \bar{g_{\rm ff}} \quad {\rm cm}^{-1}, \tag{2.36}$$

where $n_{\rm e}$ and $n_{\rm i}$ is the density of the electrons and the ions, and $\bar{g_{\rm ff}}$ is the gaunt factor (Rybicki & Lightman, 1979).

As a consequence, when a photon travels a distance dl, it has a chance to either be absorbed or scattered, so the corresponding optical depth τ is derived as the sum of $\tau_{\rm ff} = \alpha_\nu^{\rm ff} dl$ and $\tau_{\rm sc} = \sigma_{\rm kl} n_{\rm e} dl$. Then the total interaction probability $P_{\rm tot}$ is given by

$$P_{\rm tot} = 1 - \exp(-\tau), \tag{2.37}$$

where

$$\tau = \gamma(1 - \beta \cos\Theta_{\rm r})(\alpha_{\rm ff} + \sigma_{\rm kl} n_{\rm e}) dl, \tag{2.38}$$

where β and γ are the velocity in units of c and Lorentz factor of the shocked matter. $\Theta_{\rm r}$ denotes the angle between the photon momentum and the radial direction.

Once I generate two random numbers R_7 and R_8 in the range of $[0, 1]$, I decide immediately know whether the photon interacts or not in the following way.

- when $P < R_7$, the photon goes straight on,
- when $P < R_7$ and $R_8 < \alpha_{\rm ff}/(\alpha_{\rm ff} + \sigma_{\rm kl} n_{\rm e})$, the photon is absorbed,
- when $P < R_7$ and $\alpha_{\rm ff}/(\alpha_{\rm ff} + \sigma_{\rm kl} n_{\rm e}) < R_2$, the photon is scattered.

When the photon is scattered, it transforms to the rest frame of the target electron after the photon flies the distance $l = -\ln(1 - R_7)/\sigma_{\rm kl} n_{\rm e}$. [3]

The direction of scattered photon is derived by the relation of the Klein-Nishina differential cross section and the angle between the photon momentum before and after scattering Θ';

$$\frac{d\sigma_{\rm kl}}{d\Omega} = \frac{1}{2} r_0^2 f(\epsilon_{\rm i}', \Theta')^2 \left[f(\epsilon_{\rm i}', \Theta') + f(\epsilon_{\rm i}', \Theta')^{-1} - \sin^2\Theta' \right] \tag{2.39}$$

where $f(\epsilon', \Theta') = [1 + (1 - \cos\Theta')\epsilon'/m_{\rm e}c^2]^{-1}$, Ω is the solid angle and r_0 the classical electron radius. The photon energy changes satisfying the following relation,

$$\epsilon_{\rm f}' = \frac{\epsilon'}{1 + (1 - \cos\Theta')\epsilon'/m_{\rm e}c^2}, \tag{2.40}$$

where $\epsilon_{\rm f}$ is the scattered photon energy in the rest-frame of the electron.

2.3 Light crossing time

Generally, there are a very small fraction of emitted photons that can reaches to a distant point. In order to ensure the accuracy of the Monte-Carlo calculation, it is preferable to count all the photons escaped from the star. In this thesis, the problem is solved by the following method.

Figure 2.4 displays the path of the following two photons (A and A$'$) from the stellar surface (or edge of the emission region).

[3] Appendix C describe the formulation of the Lorentz transformation.

- The photon A appears from a point which is in the line of sight $l_{\rm B}$, and the path $l_{\rm A}$ has the direction angle ϕ measured from $l_{\rm B}$.
- The photon A$'$ appears from a point detached from $l_{\rm B}$, and the direction of the path $l'_{\rm A}$ is same as $l_{\rm B}$.

For convenience, I assume that the emission region is spherical symmetric, and the energies of the two photons are the same. When the angle between $l'_{\rm A}$ and the radial direction at the point A$'$ is ϕ, the photon paths $l_{\rm A}$ and $l'_{\rm A}$ are equivalent. Therefore, in the calculation, the contribution of the photon A is derived by considering of A$'$, instead. The arrival time is given by the sum of the emergence time $t_{\rm f}$ from the emission region and the difference in the light crossing time h/c, so

$$t_{\rm obs} = t_{\rm f} + \frac{R(1-\cos\phi)}{c}. \tag{2.41}$$

where R is the radius of the emission region.

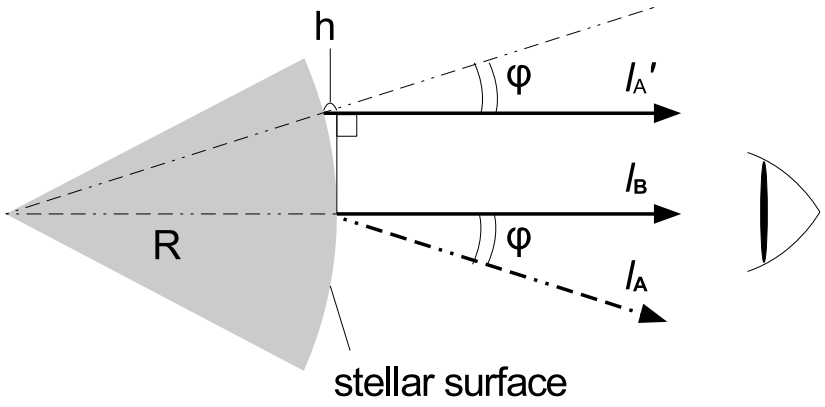

Figure 2.4: Schematic image of photons arriving to the observer (Ohtani et al., 2013).

2.4 Results

I calculate spectra and light curves of photons emitted from an ultra-relativistic shock associated with a jet. Before going to resultant figures, I present an overall picture of how photons travel through the stellar surface.

2.4.1 Propagation of photons

Photons emitted from the shock front have an isotropic distribution in the rest frame of the shock. [4] In the observer frame, they are concentrated in a small solid angle $d\Omega$, because the shocked matter moves with a Lorentz factor of $\Gamma/\sqrt{2}$. For conservation of number, the angular distribution in the observer frame can be written by $2/[\Gamma^2[1-(1-2\Gamma^{-2})^{1/2}\cos\phi]^2]$, where ϕ is the angle between the direction of the photons and the shock normal. Figure 2.5 displays the angular distributions in the cases of Γ =10, 50, 100. The emitted photons initially have energies of $E \approx \Gamma k_{\rm B}T$ in the observer frame.

Here in the limit of $\Gamma \gg 1$, about two third of emitted photons move in the directions with $\cos\phi > \sqrt{1-\Gamma^{-2}}$. These photons proceed ahead of the shock front. Once photons scatter off upstream electrons, the photon energies (E) change so that they approach to the rest mass energy of an electron. Namely,

- if $m_{\rm e}c^2 \lesssim \Gamma k_{\rm B}T$, E decreases to $m_{\rm e}c^2$,
- and if $\Gamma k_{\rm B}T < m_{\rm e}c^2$, E does not appreciably change.

Since the shock accelerates, most of scattered photons will be overtaken by the shock front, and immediately scatter off downstream electrons. At this time, the photon energies increase up to $\sim \Gamma(1+\cos\phi)m_{\rm e}c^2/\sqrt{2}$. If the optical depth of the upstream is still larger, similar processes will repeat. Eventually, the photon energies converge toward a critical value of $\Gamma_{\rm ph}m_{\rm e}c^2$, where the subscript ph denotes the position of the photosphere.

2.4.2 Spectra

In order to calculate the absolute value of luminosity, I assume that the stellar radius R is 10^{10} cm when $X_{\rm b} = 10^7$ cm, 10^{12} cm when $X_{\rm b} = 10^9$ cm, and 10^{13} when $X_{\rm b} = 10^{11}$ cm. In the following, the three models are called "Model-S", "Model-M", and "Model-L". Note that the radius R does not affect the shape of the spectrum on logarithmic scale. Figure 2.6 shows the schematic picture of the position of the shock front.

Figure 2.7 shows the resultant spectra for "Model-S", "Model-M", and "Model-L". For all of the three models, I examine the cases of $\Gamma_{\rm b}$ = 10, 50, 100. The red solid lines in Figure 2.7 show the time-integrated spectra of scattered photons, which escaped from the stellar surface before the shock disappears. The blue dotted lines display the same photons as the red solid line but for the moments they originate from the shock front. Hereafter, I call them as "initial" photons. The energy distribution of "initial" photons exactly matches the doppler shifted Planck distributions at different temperatures.

[4] Appendix D summarize some of the relativistic effects on radiation.

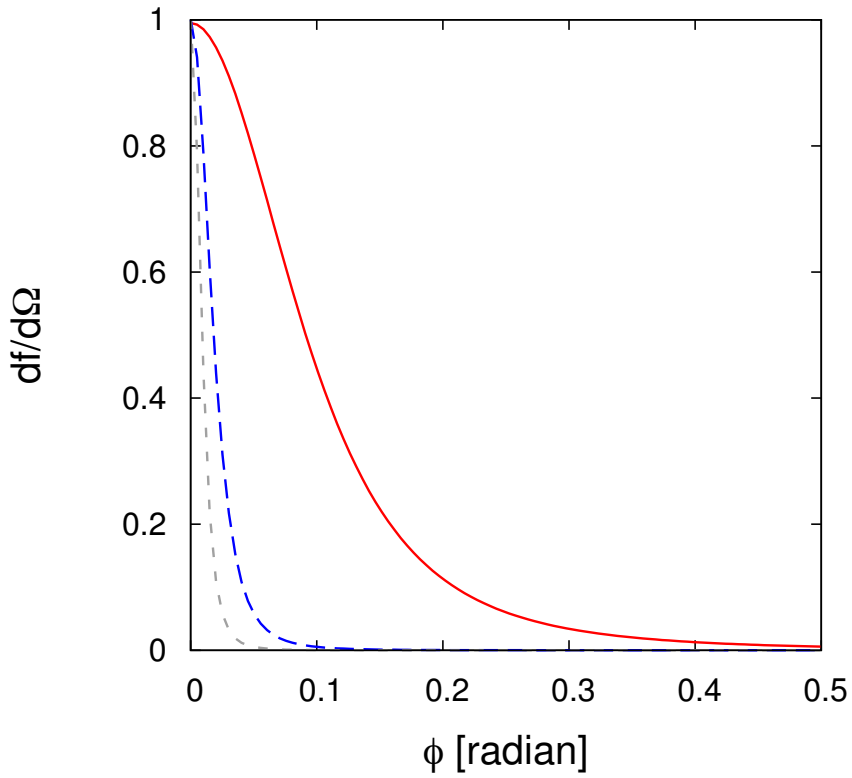

Figure 2.5: The angular distribution of the emitted photons with respect to the shock normal in the observer frame. The shock Lorentz factors are 10 (red solid line), 50 (blue long-dashed line), and 100 (gray short-dashed line).

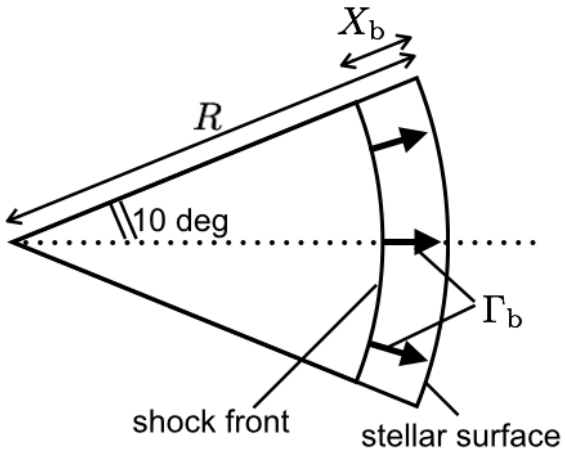

Figure 2.6: Schematic image of the shock front at the stellar surface.

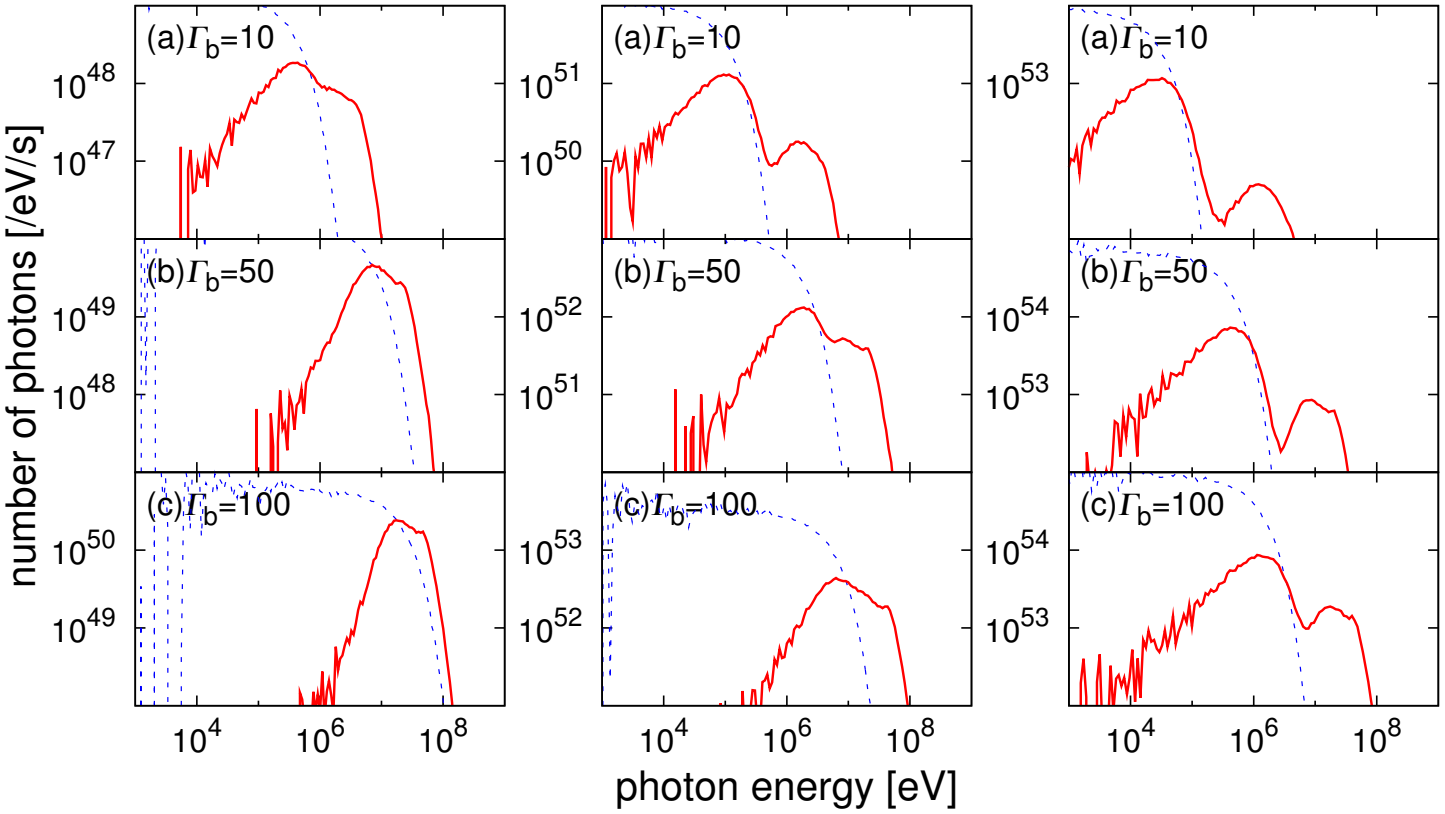

Figure 2.7: Time-integrated spectra of the ultra-relativistic shock breakout at the surface of a star. The left panels show when $(R, X_{\rm b}) = (10^7, 10^{10})$ cm (Model-S), the middle panels when $(10^9, 10^{12})$ cm (Model-M), and the right panels when $(10^{11}, 10^{13})$ cm (Model-L). The red solid lines show the energy distribution of scattered photons, while the blue dotted lines those at the moment that the photons originate from the shock front.

The time-integrated spectra (red solid lines) show that each spectrum has two notable features. One is the signature of bulk-Comptonization appearing at photon energies of $\Gamma_{\rm ph} m_{\rm e} c^2 \propto \Gamma_{\rm b} (\equiv E_{\rm HE})$. Here the subscript ph denotes the position of the shock front when the optical depth of the upstream matter is 1. The $E = E_{\rm HE}$ component consists of photons scattered at $\tau \gtrsim 1$. On the other hand, the other characteristic feature appears at the cut-off energy of the "initial" spectrum, of which typical value is $\Gamma_{\rm ph} k_{\rm B} T_{\rm s,ph} (\equiv E_{\rm LE})$. This is because the $E = E_{\rm LE}$ spectral component consists of photons generated at $\tau < 1$.

Though all of the time-integrated spectra has both of the thermal and non-thermal components, the spectral shapes are very sensitive to $X_{\rm b}$.

- In Model-S, the spectrum has a single peak at $E = E_{\rm LE}$ and a cut-off at $E = E_{\rm HE}$.
- In Model-L, the spectrum consists of two peaks at energies $E_{\rm LE}$ and $E_{\rm HE}$.
- Model-M is the intermediate case.
  - When $50 \lesssim \Gamma_{\rm b}$, a single peak.
  - When $\Gamma_{\rm b} = 10$, two peaks.

The reason why the spectral shape depends on $(X_{\rm b}, \Gamma_{\rm b})$ is explained by the $(X_{\rm b}, \Gamma_{\rm b})$ dependences of $E_{\rm LE}$, i.e.,

$$E_{\rm LE} = \Gamma_{\rm ph} k_{\rm B} T_{\rm s,ph} \propto \frac{X_{\rm s}^{3/4}}{X_{\rm b}}. \tag{2.42}$$

When $X_{\rm b}$ becomes large, $E_{\rm LE}$ becomes one or two orders of magnitude lower than $E_{\rm HE}$. For this reason, the thermal photons form a component separated from the non-thermal component. Here I describe the spectral shape around $E = E_{\rm LE}$ using a broken power-law function with exponents α and β. As an example, Figure 2.8 shows the power-law fitting for Model-M, $\Gamma_{\rm b} = 10$. (For the double-peak spectra, I define E_ξ as the energy of the flux minimum between the two peaks.) Table 2.1 shows the summary of the spectral features.

I compare the results with the GRB Band function. In observed GRB spectra, the peak energies are lower than 1 MeV. From Figure 2.7 and Table 2.1, this condition can be satisfied by Model-M and L, when $\Gamma_{\rm b}$ is 10 or 50. In these models, when a spectrum has a double-peak structure, the power-law exponent β has a value within the standard deviation for GRBs. However, the exponent α has a value significantly larger than zero in any of the models. It can not explain the lower-energy component of the Band function.

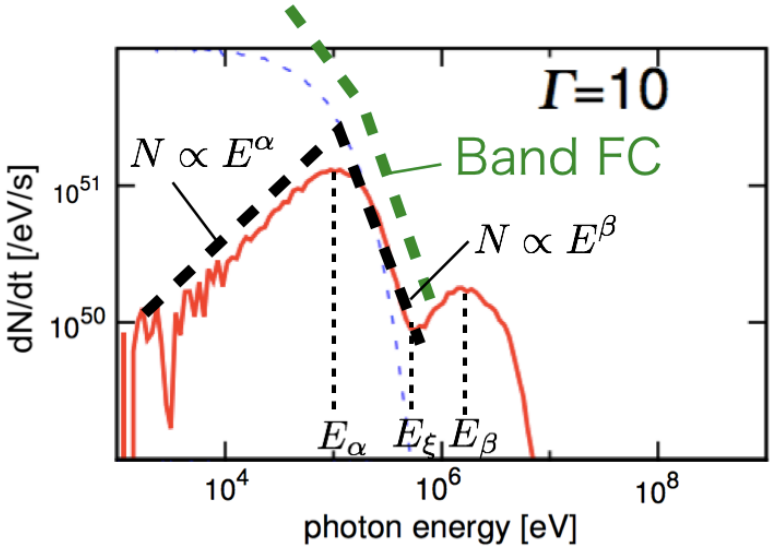

Figure 2.8: Example of fitting the resultant spectrum to a broken power-law distribution (in the case of Model-M, $\Gamma_{\rm b} = 10$).

Table 2.1: Summary of the spectral features of ultra-relativistic shock breakout at the stellar surface. $E_{\rm LE}$ and $E_{\rm HE}$ are the characteristic photon energies of the thermal components and bulk Comptonization, respectively. E_ξ is the photon energy at which the flux has minimum value between $E_{\rm LE}$ and $E_{\rm HE}$. α and β are power-law indexes of the lower- and higher-energy sides than $E = E_{\rm LE}$.

$X_{\rm b}$	$\Gamma_{\rm b}$	$k_{\rm B}T(\tau = 3)$	Double Peak?	$\Gamma_{\rm ph}$	$E_{\rm LE}$	α	$E_{\rm HE}$	β	E_ξ
10^7 cm	10	13 keV	No	12	0.4 MeV	1.25	4.0 MeV	-0.57	-
	50	42 keV	No	61	6.3 MeV	1.41	22 MeV	-0.67	-
	100	76 keV	No	121	16 MeV	1.94	48 MeV	-0.60	-
10^9 cm	10	3.4 keV	Yes	12	120 keV	0.93	1.6 MeV	-2.20	630 keV
	50	11 keV	No	61	2.0 MeV	1.20	20 MeV	-0.79	5.5 MeV
	100	18 keV	No	121	6.6 MeV	0.82	41 MeV	-2.73	-
10^{11} cm	10	1.0 keV	Yes	12	34 keV	0.74	1.2 MeV	-2.81	270 keV
	50	2.8 keV	Yes	61	500 keV	0.64	8.0 MeV	-2.43	2.8 MeV
	100	4.7 keV	Yes	121	1.3 MeV	0.58	17 MeV	-1.90	7.2 MeV

2.4.3 Light curves

Figure 2.9 shows the light curves when $\Gamma_{\rm b} = 10$. Here I define $t_{\rm obs}^{99}$ as the time when 99% of scattered photons have reached the observer. $t_{\rm obs}^{99} = 5.9 \times 10^{-4}$ sec in Model-S, 6.1×10^{-2} sec for Model-M, and 0.6 sec in Model-L. The overall shape ($0.1t_{\rm obs}^{99} \lesssim t_{\rm obs} \lesssim 0.9t_{\rm obs}^{99}$) of the light curves are fitted with power-law distributions with exponents larger than -1.0 and smaller than -0.9. The durations ($t_{\rm obs}^{99}$) correspond to the light crossing time of the emission region, which is proportional to $R/(c\Gamma_{\rm b}^2)$. Accordingly, the emission can not last longer than 2 sec, even when R is as large as 10^{13} cm. The fact suggests that the contribution of shock breakout to the emission of a GRB might be very small.

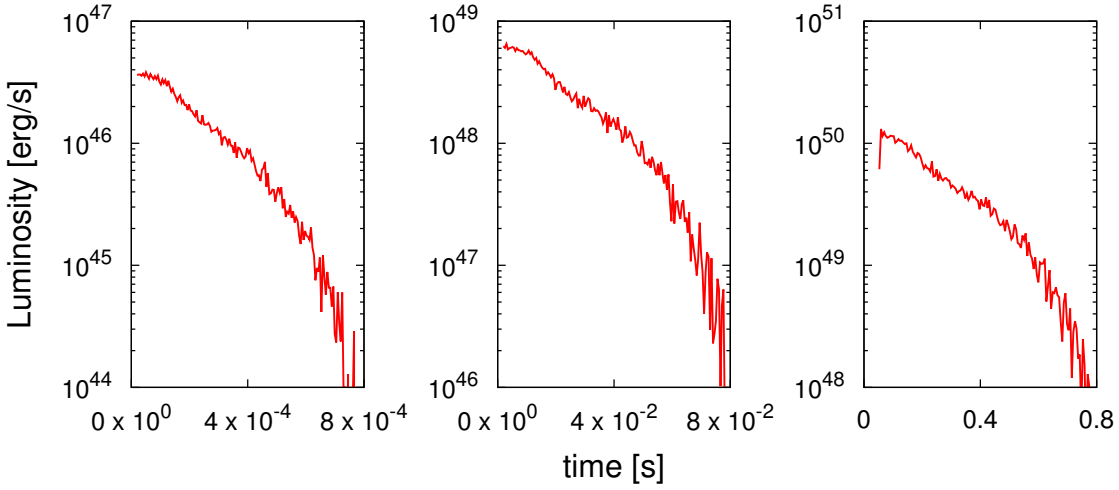

Figure 2.9: Light curves of the ultra-relativistic shock breakout at the surface of a star. The left panel shows when $(R, X_{\rm b}) = (10^7, 10^{10})$ cm (Model-S), the middle panel when $(10^9, 10^{12})$ cm (Model-M), and the right panel when $(10^{11}, 10^{13})$ cm (Model-L). The shock Lorentz factor $\Gamma_{\rm b}$ equals 10 at the breakout.

The total radiated energy is described as a function of R and $\Gamma_{\rm b}$. By equating (2.24), (2.28), and (2.30), the photon generation rate per unit area is expressed as follows.

$$N_\nu = \frac{32\zeta(3)k_{\rm B}^3}{\left(11-3\sqrt{3}\right)c^{3/2}h^3}\left(\frac{3m_{\rm H}m_{\rm u}}{a\sigma_{\rm kl}}\right)^{3/4}\sqrt[4]{2X_{\rm b}}\sqrt{\Gamma_{\rm b}}. \tag{2.43}$$

The averaged energies of photons have a complex dependency on the parameters. When photons originate from the shock, they have the energies proportional to $X_{\rm b}^{-1}$. In Model-S, the energies of scattered photons increase up to $\sim \Gamma_{\rm ph} m_{\rm e} c^2$. Meanwhile, in Model-L, the energies of scattered photons are close to $\Gamma_{\rm ph} k_{\rm B} T_{\rm s,\,ph}$. Since each spectrum is composed of both thermal and non-thermal photons, the luminosity can not be written by a simple scaling formula in terms of $X_{\rm b}$.

On the other hand, the relation between the luminosity and $(R, \Gamma_{\rm b})$ is easily expressed as

$L \propto R\Gamma_{\rm b}^{7/2}$. It is determined by the area of emission region ($\propto R^2$), the photon energy ($\propto \Gamma_{\rm b}$), and the duration $R/(c\Gamma_{\rm b}^2)$.

2.5 Conclusions

Due to $X_{\rm b}$ (and $\Gamma_{\rm b}$) dependency of the shock temperature, the spectral shape of shock breakout becomes very different between cases of $X_{\rm b} = 10$ and 100.

- When $X_{\rm b} = 10^{11}$ cm, the energies of bulk-Comptonized photons ($E \sim E_{\rm HE} = \Gamma m_{\rm e} c^2$) are one or two orders of magnitude higher than those of thermal photons ($E \sim E_{\rm LE} = \Gamma k_{\rm B} T_{\rm s}$). For this reason, the spectrum consists of two separating components at $E \sim E_{\rm LE}$ and $E_{\rm HE}$.

- When $X_{\rm b} = 10^7$ cm, the energies of bulk-Comptonized photons and those of thermal photons are compatible. For this reason, bulk-Comptonizated photons form a cut-off shape on the thermal spectral component.

- Cases of $X_{\rm b} = 10^9$ cm are intermediate.

I describe the shapes of the thermal components using a broken-power law model with exponents α and β, and compare them with those of the observed GRBs ($\alpha \approx -1$, $\beta = -2.5$). Though some of the resultant spectra ($X_{\rm b} \geqslant 10^9$ cm) show values of β compatible with the observed GRBs, α can not have a negative value in any case.

Furthermore, the duration ($\sim R/c/\Gamma_{\rm b}^2$) of ultra-relativistic shock breakout is significantly shorter than 1 sec, which is inconsistent with that of long-GRBs ($>$ 2 sec). The total radiation energy is 10^{49} erg, which is two orders of magnitude lower than that of observed prompt emission of GRBs.

For these reasons, I conclude that ultra-relativistic shock breakout can not explain the entire emission of a prompt GRB emission. In order to explain the lower-energy emission, duration and radiation energy, it might be worth considering emission from a more extended region, such as the dense CSM.

Chapter 3

Ultra-relativistic shock breakout in the CSM

It might be possible to obtain some information on the central engine activity by examining the relations between the behavior of a shock and shock breakout. As referred in Chapter 2, the shock behavior is independent of the energy injection rate when the shock propagates through the stellar surface. Meanwhile, when the shock propagates in a CSM, its behavior is directly determined by the energy injection rate. For this reason, I calculate the ultra-relativistic shock breakout in a dense CSM.

3.1 Hydrodynamics

Initial profiles of CSM are given by the same formula in Section 4.1.1 (Equation 4.3). The hydrodynamical evolution between the forward-shock and the contact surface is described by self-similar solutions found by Blandford & McKee (1976). The combination of the basic equations yields the following equations;

$$\frac{d}{dt}\left(p\gamma^4\right) = \gamma^2\frac{\partial p}{\partial t}, \tag{3.1}$$

$$\frac{d}{dt}\ln\left(p^3\gamma^4\right) = \frac{-4}{r^2}\frac{\partial}{\partial r}(r^2\beta), \tag{3.2}$$

$$\frac{\partial n'}{\partial t} + \frac{1}{r^2}\frac{\partial}{\partial r}\left(r^2 n'\beta\right) = 0, \tag{3.3}$$

where the definitions of t, p, β, γ, and n' are the same as those of the previous chapter, and r denotes the radius. The boundary conditions are expressed by the same formulas as Equations (2.5)–(2.6).

Here, I define a similarity variable χ as

$$\chi = \left[1 + 2(m+1)\Gamma^2\right]\left(1 - \frac{r}{t}\right), \tag{3.4}$$

changes with time t as

$$\Gamma^2 = B_{\rm sh}t^{-m}. \tag{3.5}$$

Then, non-dimensional functions are introduced as follows.

$$p_2 = \frac{2}{3}\Gamma^2\omega_1 f(\chi), \tag{3.6}$$

$$\gamma^2 = \frac{1}{2}\Gamma^2 g(\chi), \tag{3.7}$$

$$n_2' = 2\Gamma^2 n_1 h(\chi), \tag{3.8}$$

where subscript 1 and 2 are the same as Chapter 2. The boundary conditions becomes $f(1) = g(1) = h(1) = 1$.

The transformations from (t, r) to (Γ, χ) are

$$\frac{\partial}{\partial \ln t} = -m\frac{\partial}{\partial \ln \Gamma^2} + \left[(m+1)(2\Gamma^2 - \chi) + 1\right]\frac{\partial}{\partial \chi}, \tag{3.9}$$

$$t\frac{\partial}{\partial r} = -\left[1 + 2(m+1)\Gamma^2\right]\frac{\partial}{\partial \chi}, \tag{3.10}$$

$$\frac{d}{d \ln t} = -m\frac{\partial}{\partial \ln \Gamma^2} + (m+1)\left(\frac{2}{g} - \chi\right)\frac{\partial}{\partial \chi}. \tag{3.11}$$

As a result, the basic equations are written by

$$\frac{1}{g}\frac{d \ln f}{d\chi} = \frac{8m - (m-2)g\chi}{(m+1)(4 - 8g\chi + g^2\chi^2)}, \tag{3.12}$$

$$\frac{1}{g}\frac{d \ln g}{d\chi} = \frac{(7m+2) - (m+2)g\chi}{(m+1)(4 - 8g\chi + g^2\chi^2)}, \tag{3.13}$$

$$\frac{1}{g}\frac{d \ln h}{d\chi} = \frac{(18m+4) - (10m+4)g\chi + mg^2\chi^2}{(m+1)(2 - g\chi)(4 - 8g\chi + g^2\chi^2)}. \tag{3.14}$$

3.1.1 Relation between the shock behavior and the energy supplying rate

There is a relation between the shock Lorentz factor and the energy supplying rate from the central energy, which is in contrast to the flow discussed in the previous chapter. The propagation of shock emerging from the surface is determined by the density distribution of the atmosphere through the parameter δ.

To start with, in the similar solution, it is necessary that the amount of energy stored in a width of $d\chi$ does not change with time. This means that when the energy flux $(w\gamma^2\beta)$ passes through a sphere of the radius r in a time interval dt, the amount of the energy corresponds to the momentum flux $(w\gamma^2\beta^2 + p)$ of a spherical shell spreading with a constant width of χ, namely,

$$4\pi r^2 w\gamma^2\beta dt = 4\pi r^2(w\gamma^2 - p)\beta_{\rm n} dt, \tag{3.15}$$

where $\beta_{\rm n} = 1 - \chi/2\Gamma + O(\Gamma^{-4})$ is the velocity (in units of c) of the shell. Since the position of the inner boundary of the shock is characterized by a constant value of $\chi = \chi_{\rm in}$, the energy

flux $F_{\rm in}$ across the inner boundary is expressed as follows in the rest-frame of the shock.

$$F_{\rm in} = \Gamma_{\rm in}^2(1-\beta_{\rm in})^2\frac{L}{r\pi t^2} \simeq \frac{L\chi_{\rm in}}{16\pi\Gamma_{\rm in}^2 t^2}, \tag{3.16}$$

where L denotes the power supplied by the central engine (measured in the co-moving frame). Therefore,

$$L = \frac{16\pi w_1\Gamma^4 t^2 f(\chi_{\rm in})}{\chi_{\rm in}}. \tag{3.17}$$

On the other hand, in the relativistic limit, the total energy between the radius $R_0(t)$ and $R_1(t)$ is expressed by

$$E(R_0, R_1, t) = \int_{R_0}^{R_1} 16\pi p\gamma^2 r^2 dr, \tag{3.18}$$

because the total energy density can be approximated by $(4\gamma^2-1)p$. Therefore, the total energy contained in the shock ($1 \leqslant \chi \leqslant \chi_{\rm in}$) is given by

$$E = 8\rho_1\Gamma^2 t^3/9, \tag{3.19}$$

where $\alpha = \int_1^{\chi_{\rm in}} fg\ d\chi$.

The energy injection rate L can be expressed

$$L(1-\beta_{\rm in}) \simeq \frac{L}{2\Gamma_{\rm in}^2} = \frac{dE}{dt}, \tag{3.20}$$

and

$$\alpha = \frac{3(m+1)}{3-m} f(\chi_{\rm in}). \tag{3.21}$$

Here, the energy injected into the ultra-relativistic shock is assumed to follow a power-law of the time, such as

$$L = L_0 t_{\rm e}^q, \tag{3.22}$$

where $t_{\rm e}$ denotes the emitted time. In this case,

$$t_{\rm e} = \frac{t}{2}\frac{\chi_{\rm in}}{\Gamma(m+1)}, \tag{3.23}$$

and

$$m = \frac{-q}{2+q}. \tag{3.24}$$

In order to investigate the relation between the appearance of the shock breakout emission and the energy injection rate, we obtain self-similar solutions for m =0 (uniform) , -2/3 (accelerate), 1 (decelerate). These values of m correspond to the cases that q =0 (constant rate injection), 4, -1 (impulsive).

Table 3.1: Dependence of m on q in the circumstellar matter with density $n \propto r^{-k}$, $k = 2$ (Blandford & McKee, 1976).

q	4	1	0	2/3	-4/5
m	-2/3	-1/3	0	1/2	2/3

3.1.2 Freely expanding ejecta

I assume that the ejecta expand freely, and determine the velocity by $v_{\rm ej} = r/t$. Here I use a uniform density approximation. The reason is as follows. The density of shocked ejecta is expected to be so high that when a photon enters ejecta, it will be scattered immediately, or otherwise be absorbed. Thus the internal structure is not important for the photon transfer. In this study, I assume that the density of the ejecta is 10^4 times higher than that of the shock front, and the velocity is the same as that of the shocked CSM at the contact surface.

In the following, I define $R_{\rm s}$, $R_{\rm c}$ as the radius of the shock front and the contact surface.

3.1.3 Settings of Monte-Carlo calculation

The following list describes the setup for Monte-Carlo calculations.

- Shock breakout occurs at a radius of 1×10^{12} cm, which is close to the breakout radius supposed for XRO 080109/SN 2008D.
- Inverse-Compton scattering and free-free absorption is taken into consideration. Figure **??** shows the overview of the Monte-Carlo method used in the calculation.
- The position of the photosphere is determined so that 37% of generated photons diffuse out and the others are absorbed.
  - Figure 3.2 shows a schematic picture of the shock propagation and the photosphere.
  - Figure 3.3 displays the position of the photosphere relative to the shock radius. More precisely, the y-axis shows the ratio

$$f = \frac{R_{\rm ph} - R_{\rm c}}{R_{\rm s} - R_{\rm c}}, \tag{3.25}$$

    where $R_{\rm ph}$ is the photospheric radius. The x-axis shows the time t divided by the moment of shock breakout $t_{\rm b}$. Since the temperature of shocked matter decreases with time, the position of the photosphere approaches the contact surface (i.e., f becomes smaller). The right-most point in each panel shows the time the shocked region becomes transparent.
- The angular aperture of a jet is 10 deg.
- In case of a decelerating shock, the calculation stops when the shock reaches at a radius of $R_{\rm f} = 10^{16}$ cm, because
  - the scattering optical depth is not negligible within the radius.
- In case of an accelerating shock or a shock with a constant velocity, the calculation stops at a smaller radius of $R_{\rm f} = 10^{15}$ cm, because
  - the shock will begin to decelerate at some radius.
- The light curve and spectrum are presented for several pairs of the index m and shock Lorentz factor $\Gamma_{\rm b}$ at the moment of breakout.

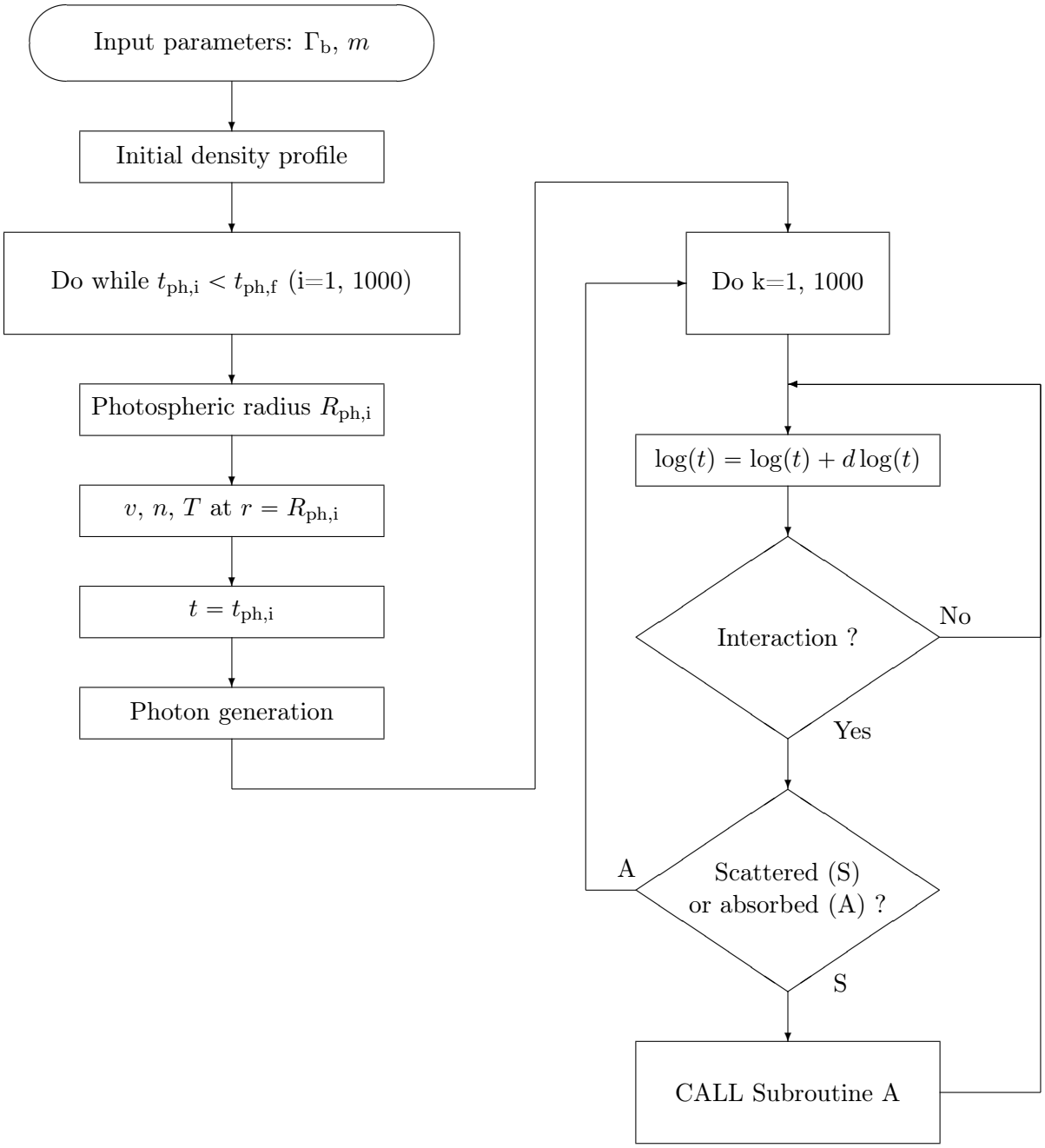

Figure 3.1: Monte-Carlo simulation for ultra-relativistic shock breakout in the CSM. Definition of Subroutine A is shown in Figure 2.3.

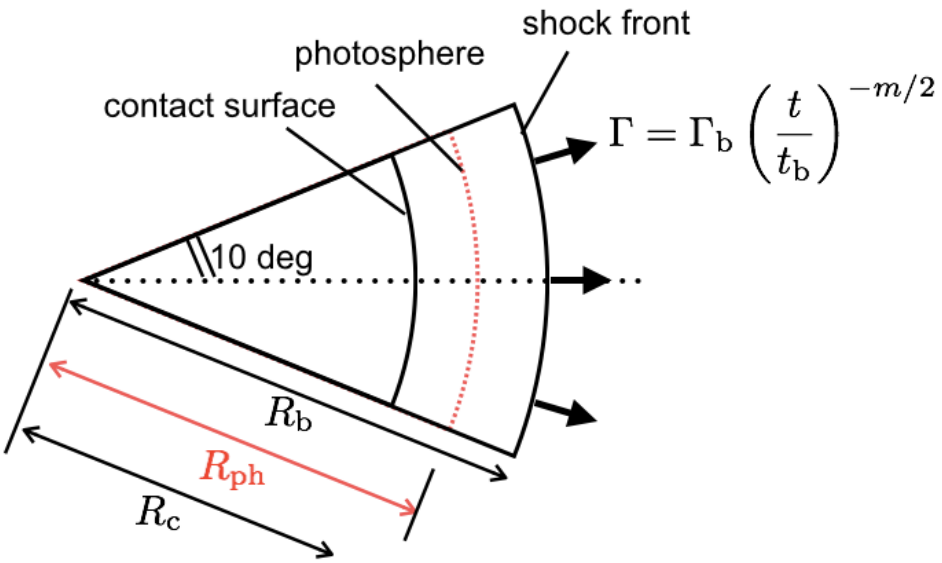

Figure 3.2: Schematic image of the shock propagation in the CSM.

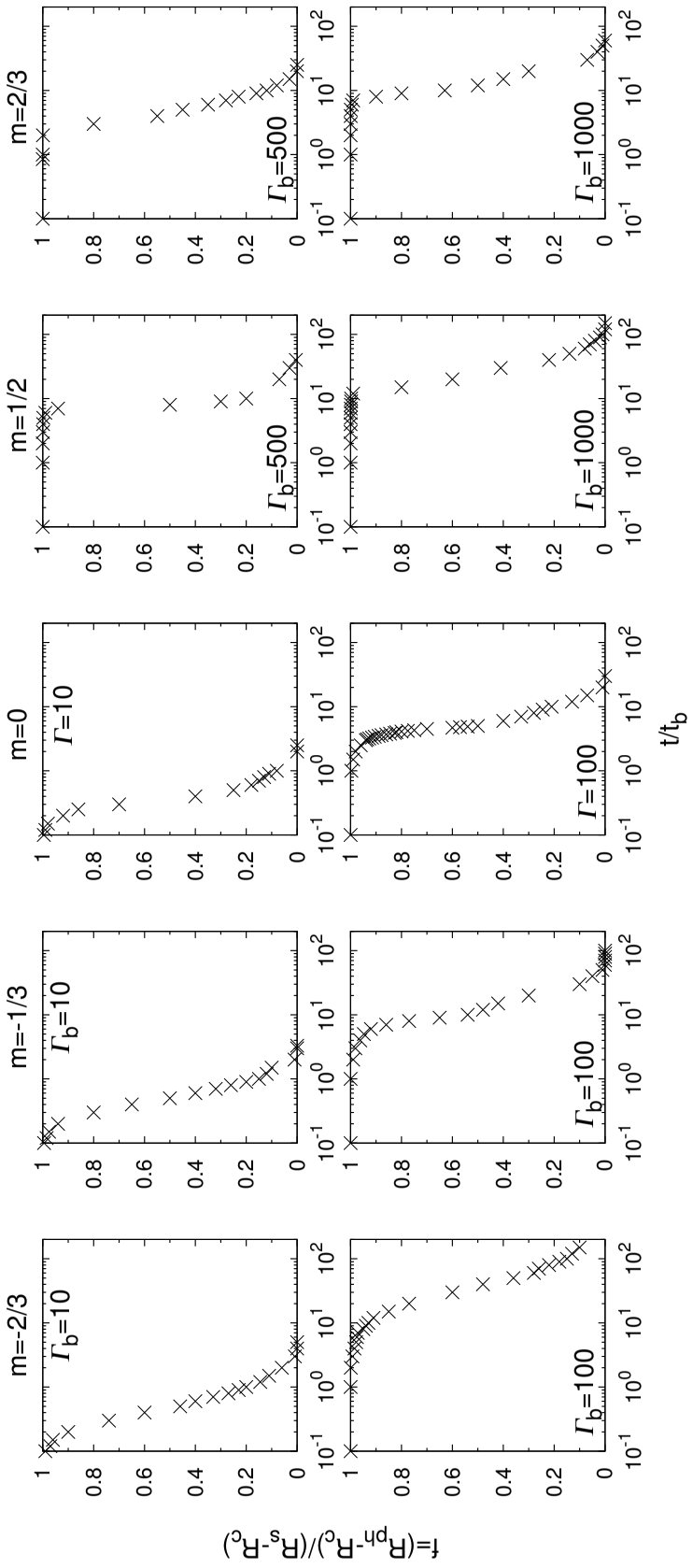

Figure 3.3: Position of the photosphere.

3.2 Results

I investigate the influence of the behavior of the shock (characterized by the index m defined in Equation (3.5); the shock accelerates if $m < 0$ and decelerates if $m > 0$) in the CSM and the shock Lorentz factor $\Gamma_{\rm b}$ at the moment of shock breakout on the spectra and light curves. First of all, I introduce the overall picture of traveling photons.

3.2.1 Two types in photon traveling

Because the photosphere moves with time, there seem two types of photon traveling. Figure 3.4 shows comparison of the position of the photosphere (expressed in Figure 3.3) in cases of $(m, \Gamma_{\rm b}) = (-2/3, 10)$ (left panel) and $(1/2, 500)$ (right panel).

In the case of $(m, \Gamma_{\rm b}) = (-2/3, 10)$, $f \approx 0.2$ (defined by Equation (3.25)) at the moment of shock breakout ($t = t_{\rm b}$). That means, the photosphere locates near the contact surface at $t = t_{\rm b}$. These photons are overtaken by ejecta before escaping through the CSM. Since the shock front get accelerated, photons can repeat scattering several times in the shocked CSM or ejecta. Furthermore, f becomes smaller with time, so most of photons emitted from an accelerating shock of $(m, \Gamma_{\rm b}) = (-2/3, 10)$ are overtaken by ejecta. Even in the case of $(m, \Gamma_{\rm b}) = (-2/3, 100)$, in which $f = 1$ at $t = t_{\rm b}$, a similar process can occur, because the accelerating matter will overtake photons.

On the other hand, in the case of $(m, \Gamma_{\rm b}) = (1/2, 500)$, $f = 1$ at the moment of the breakout. Since the shock decelerates, photons emitted from the shock front can escape from the CSM before being overtaken by ejecta. Therefore, these photons scatter off only in the CSM. After $t \sim 10 t_{\rm b}$, f becomes very close to 0. At that time, significant fraction of emitted photons will be overtaken by ejecta.

3.2.2 Light curves

Figure 3.5 displays the resulatant light curves in the energy range covered by the Swift/XRT (Gehrels et al., 2004; Burrows et al., 2005). Here I define t_{50} and t_{95} as the times at which 50 or 95 % of photons have reached the observer. In Figure 3.5, t_{50} is expressed using a dotted vertical line. Also, Table 3.2.2 summarizes t_{50} and t_{95} for each parameter set.

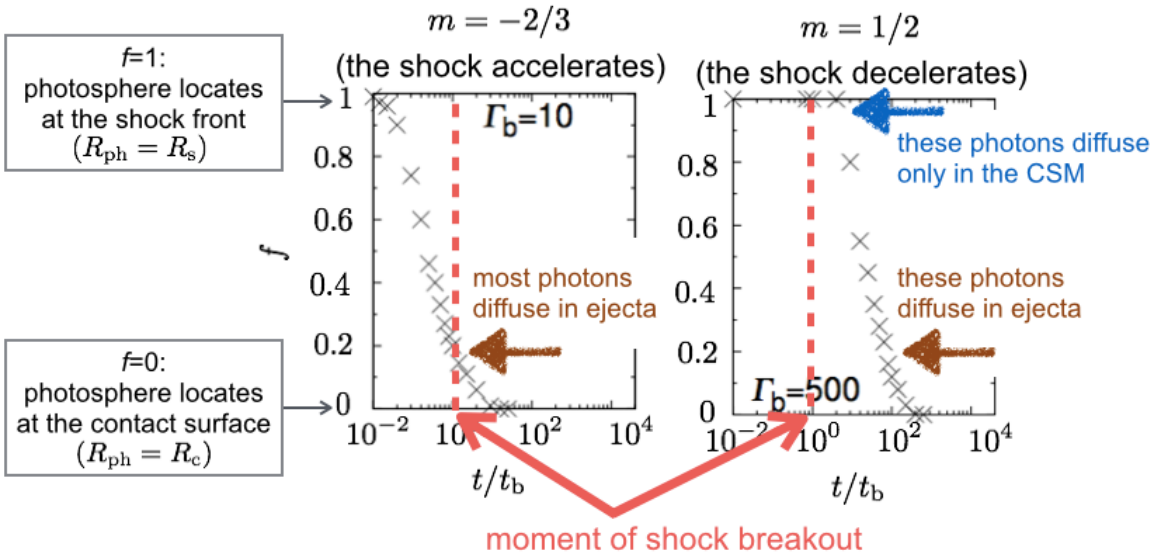

Figure 3.4: Difference of position of the photosphere between cases of an accelerating shock ($m < 0$) and a decelerating shock ($m > 0$). If $m < 0$, the photosphere locates near the contact surface at $t = t_b$, so most of emitted photons enter in ejecta. On the other hand, if $m > 0$, the photosphere locates at the shock front at t_b, then gradually approaches to the contact surface. In this case, some photons escape from the CSM before being overtaken in ejecta, while some others enter in ejecta.

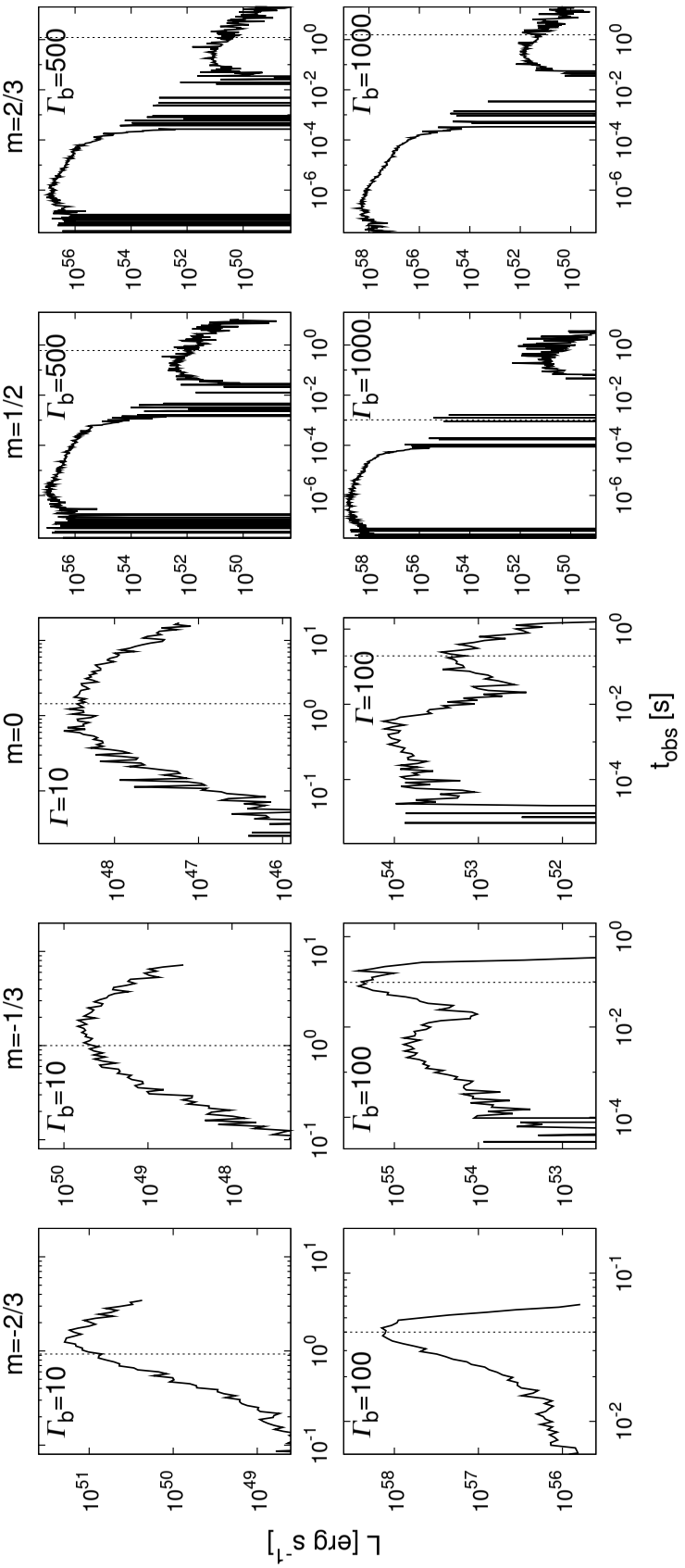

Figure 3.5: Light curves of U.R.-shock breakout emission from the CSM. Photons with energy less than the lower detection limit (0.2 keV) of the Swift/XRT are excluded. The dotted vertical lines indicates t_{50}, at which half of photons have being detectable.

Table 3.2: Dependences of t_{50} and t_{95} on m, $\Gamma_{\rm b}$, and $\Gamma_{\rm f}$.

m	$\Gamma_{\rm b}$	$\Gamma_{\rm f}$	t_{50}, t_{95} [s]	
-2/3	10	100	0.9	2
	100	1000	0.04	0.05
-1/3	10	32	1	4
	100	316	0.1	0.2
0	10	10	1	8
	100	100	0.2	0.8
1/2	500	50	0.5	4
	1000	100	0.001	2
2/3	500	23	1	10
	1000	46	1	10

Since t_{95} is approximately proportional to $R_{\rm f}/(c\Gamma_{\rm f}^2)$, where $\Gamma_{\rm f}$ denotes the shock Lorentz factor at $r = R_{\rm f}$, the timescale of the light curve is determined by diffusion in the shocked matter. Regardless of that, the shapes of light curves are obviously different between $m \leqslant 0$ and $m > 0$.

- In the case of $m < 0$, the time (hereafter $\Delta t_{\rm p}$) from the onset to the peak are compatible to the time (hereafter $\Delta t_{\rm d}$) from the peak to t_{95}.
- In the case of $m > 0$, the light curve shows two components; early emission decaying in shorter than 10^{-4}–10^{-3} sec, and late emission lasting several sec. In the late emission, $\Delta t_{\rm p}$ is at least ten times shorter than $\Delta t_{\rm d}$.
- $m = 0$ is the intermediate case.

The difference can be explained by characteristics of photon travel referred in the previous section. If the shock accelerates, most scattered photons are stored at the surface of ejecta.

As soon as the shocked matter becomes thin, these photons escape through the CSM. As a consequence, if $m < 0$, $\Delta t_{\rm p}$ is consistent with the time when the optical depth of the CSM becomes significantly smaller than 1. In this case, $\Delta t_{\rm p}$ is not far smaller than $\Delta t_{\rm d}$.

On the other hand, if the shock decelerates, photons emitted at $t \sim t_{\rm b}$ can escape from the CSM shortly after the generation. Accordingly, these photons cause the early emission. Meanwhile, photons emitted at $t \gg t_{\rm b}$ stay in ejecta at first, then escape when the CSM becomes thin enough. For this reason, these photons form the late emission.

3.2.3 Spectral evolution

The red solid lines in Figure 3.6 show the time-integrated spectra of scattered photons, which escape from the CSM. The blue dashed lines denote the same photons but at the moments they originate from the shock front. Hereafter, I call them as "initial" photons. Since the absorption is taken into consideration, the distribution of "initial" photons does not match the doppler shifted Planck distributions at different temperatures. Only a small fraction of photons with energies lower than ≈ 1 keV can survive absorption.

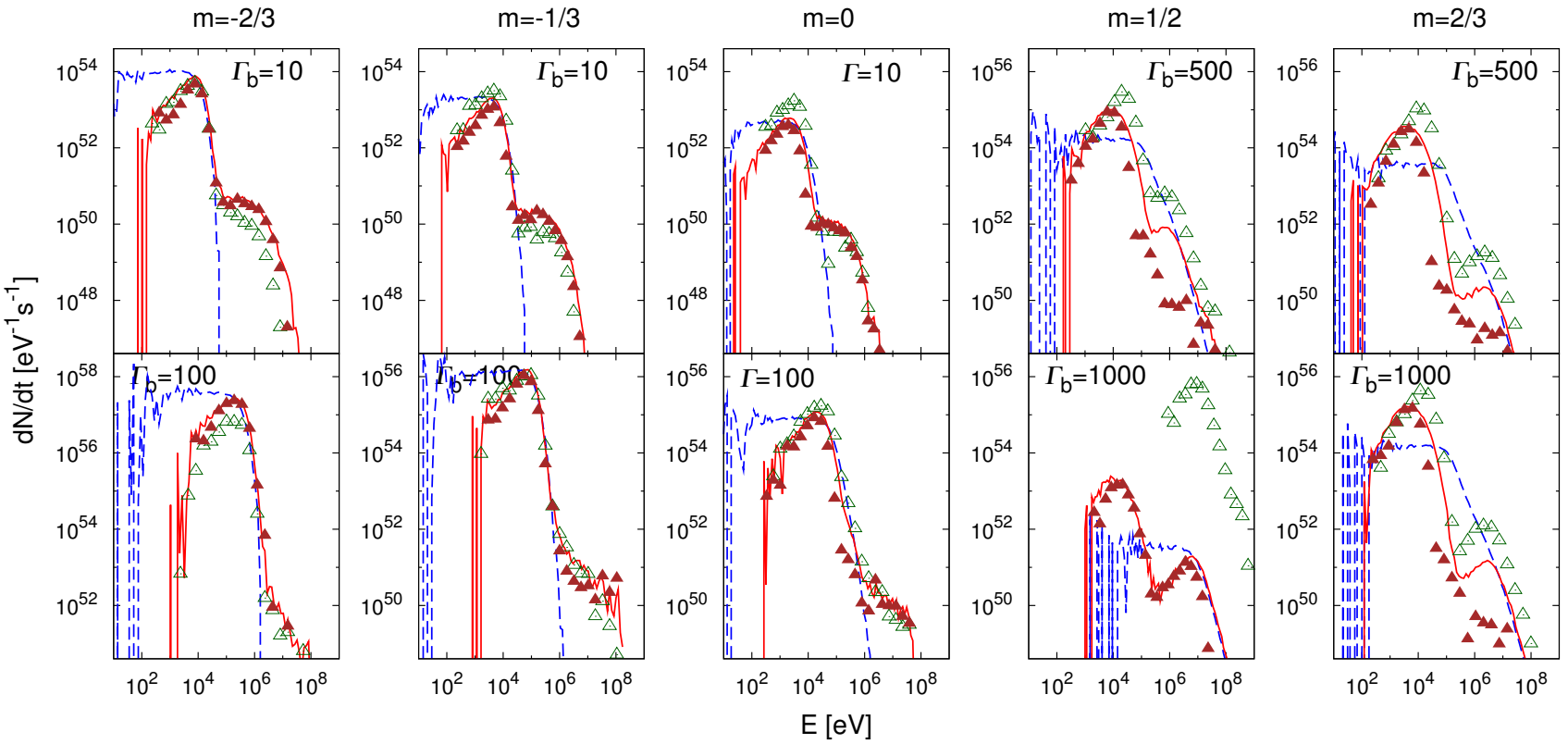

Figure 3.6: Spectral evolution of U.R.-shock breakout emission from the CSM. The lines indicate average number flux spectra of initial photons (blue dashed line) and of scattered photons (red solid line) over the time duration 0 to t_{95}, and the triangles display time-resolved spectra in the energy range above $E_{\rm XRT,low}$ for $t_{\rm obs} < t_{50}$ (open triangle) and $t_{\rm obs} > t_{50}$ (filled triangle).

The time-integrated spectra (red solid line) of scattered photons share some similarities regardless of m and $\Gamma_{\rm b}$. Most of the spectra have peaks at the cut-off energy of the "initial" spectra. Since the "initial" emission has thermal properties, the cut-off energy is about $\Gamma k_{\rm B}T (\equiv E_{\rm p})$. On the contrary, there seems a $(m, \Gamma_{\rm b})$ dependency in spectra in the energy range higher than $E_{\rm p}$ as follows.

- If $m \leqslant 0$ and $\Gamma_{\rm b} = 10$, the high-energy emission (above 0.1–1 MeV) has an exponential cut-off.
- If $m \leqslant 0$ and $\Gamma_{\rm b} = 100$, the high-energy emission has a power-law feature.
- If $m > 0$, the high-energy emission forms an independent.

These spectral behaviors would be explained by the energy efficiency through electron scattering. In the case of an accelerating shock, most photons scatter off the downstream electrons several times, and the energies increase up to $\Gamma m_{\rm e}c^2$. On the other hand, in the case of a decelerating shock, only photons escaping at $t < t_{50}$ can obtain high energies. The rest of scattered photons sometimes lose the energies after scattering.

In order to confirm the energy change of scattered photons, I calculate time-resolved spectra. The open and filled triangle points in Figure 3.6 display energy distributions of photons received in the period of $t_{\rm obs} < t_{50}$ and $t_{\rm obs} > t_{50}$. In the cases of $m \leqslant 0$, the early and late spectra have similar shapes. On the other hand, in the cases of $m > 0$, fluxes of high energy photons (> 1 MeV) is larger in $t_{\rm obs} < t_{50}$ than in $t_{\rm obs} > t_{50}$.

3.3 Comparison with GRBs

Though some of the resultant spectra have non-thermal features above 0.1–1 MeV, the fraction of low-energy photons seems too high to explain the general spectral features of long-GRBs. Accordingly, it might be difficult to reproduce the general GRBs by an ultra-relativistic shock breakout of a conical jet.

In this study, I do not take the energy loss by emission into consideration. The effects of energy loss might reduce both of the the high-energy and low-energy components, and cause a complex time-variabilities as shown in observed GRBs.

3.4 Conclusions

Properties of shock breakout in the CSM depend on whether the shock accelerates and decelerates. Note that the behavior of the shock is determined by the energy injection rate L from the central engine, and when $dL/dt = 0$ the shock will propagate with a constant velocity if the density of the CSM is proportional to r^{-2}.

Differences between the emission from accelerating or decelerating shock are seen in the following properties.

- If the shock accelerates, the time t_{50} that half of generated photons appear is compatible to the time between t_{50} and t_{95}. If the shock decelerates, t_{50} is far smaller than t_{95}-t_{50}.
- If the shock accelerates, there is no significant difference between photons arriving at $t_{\rm obs} < t_{50}$ and $t_{\rm obs} > t_{50}$. If the shock decelerates, photons with higher energies tend to arrive earlier.

These discrepancies might be a source of information on whether the energy injection to the ultra-relativistic shock increases with time (at least for $\sim R_{\rm b}/c \approx$several tens sec) or begins to decrease instantly after the generation.

Chapter 4

Mildly-relativistic shock breakout

Properties of shock breakout (such as light curve and spectrum) might be sources of information on the geometry of the shock such as degree of asymmetry. Previous studies (Suzuki & Shigeyama, 2010a,b) having examined the light curve and spectrum of XRO 080109/SN 2008D, from which the shock breakout was observed in unprecedented detail, involve two problems in reproducing the observed properties. One is that the spectrum is explained in the context of 1D hydrodynamic model, though it is necessary to consider an asymmetric shock for reproducing the light curve. The other is that the light curve is calculated without taking scattering of photons in the CSM (or ejecta) into account.

I calculate both the light curve and spectrum as results of photon scattering in the CSM, assuming an asymmetric shock as described by Suzuki & Shigeyama (2010b). Since XRO 080109/SN 2008D is an observational milestone in study of non-relativistic shock breakout from the CSM, I apply the model presented in this chapter to this event, and discuss the properties of this object that can be deduced from the light curve and spectrum.

4.1 Hydrodynamics

In this study, the motion of the shocked matter is given by hand, so that the velocity becomes constant regardless of time. I approximate the distribution of the shocked matter as a uniform shell. The reasons are as follows; the optical depth of the CSM is small ($\lesssim 1.4$), and the mean-free path of a photon in the ejecta should be much shorter than the thickness of the shell.

4.1.1 Initial profile of a CSM

The density distribution of the CSM is expressed by the steady wind solution (e.g. Chevalier, 1982; Chevalier et al., 1992). If the motion of the CSM is stationary and spherically symmetric, the mass conservation, of which general form is

$$\frac{\partial \rho}{\partial t} + \nabla \cdot (\rho \boldsymbol{v}) = 0, \tag{4.1}$$

where ρ is the mass density and $\boldsymbol{v}$ the velocity, yields

$$\frac{1}{r^2}\frac{d}{dr}(r^2\rho v) = 0. \tag{4.2}$$

The velocity becomes constant after the acceleration up to $v_{\rm w} \sim 1000$ km s^{-1} in the wind blown from a Wolf-Rayet star. As a result, the above equation reduces to the following density distribution.

$$\rho(r) = \frac{\dot{M}}{4\pi v_{\rm w}} r^{-2}, \tag{4.3}$$

where $\dot{M}$ is the mass-loss rate.

In a non-relativistic shock breakout, the timescale of photon travel $\Delta t_{\rm trv}$ of photons (roughly represented by the value at breakout, $\tau_{\rm b} R_{\rm b}/c$ where $\tau_{\rm b}$ and $R_{\rm b}$ denote the optical depth and radius at breakout) is longer than the light crossing time $\Delta t_{\rm lc} = R_{\rm b}/c$. One can expect that the luminosity increases for the light crossing time from the onset. Therefore, I determine the breakout radius by interpreting the observed time between the onset and the peak of the outburst $\Delta t_{\rm rise}$ as $\Delta t_{\rm lc}$. By referring to the observation of XRO 080109 (Figure 1.22), $\Delta t_{\rm rise}$ is estimated to be 100 sec. Thus,

$$R_{\rm b} = c\Delta t_{\rm rise} = 3 \times 10^{12} \text{ cm}. \tag{4.4}$$

4.2 Freely expanding ejecta

Since the ejecta expand have swept a tiny amount of the CSM at a radius of $\approx 10^{12}$-10^{14} cm, the ejecta remain freely expanding. In this case, the density of the ejecta decreases with time as t^{-3}, where t is measured from the moment of stellar explosion (Chevalier & Liang, 1989).

In reality, the distribution of the ejecta velocity $v_{\rm ej}$ should satisfy $v_{\rm ej} = r/t$ and the shocked CSM has a large density gradient. Regardless of the facts, in this study I approximate the post-shock region as uniform ejecta as shown in Figure 4.1, instead of the combination of the shocked CSM and ejecta followed by the unshocked ejecta. This is because the optical depth of the CSM at breakout ($\approx c/v_{\rm ej}$, $v_{\rm ej}$ is several tens % of the speed of light) would not be significantly larger than 1 after shock breakout. Furthermore, I consider only a spherical shell of a small width compared to the radius of the shell. For example, when the number density of ejecta is 10^{14} cm^{-3}, the mean-free path of a photon with an energy of several keV is $(\sigma_{\rm s} n)^{-1} \approx 10^{10}$ cm$\ll R_{\rm b}$. (When assuming that ejecta of this density fill a sphere of radius $R_{\rm b}$, the total ejecta mass would be about $30 M_\odot$.)

Here, I assume that the ejecta expanding velocities are constant with time. At the

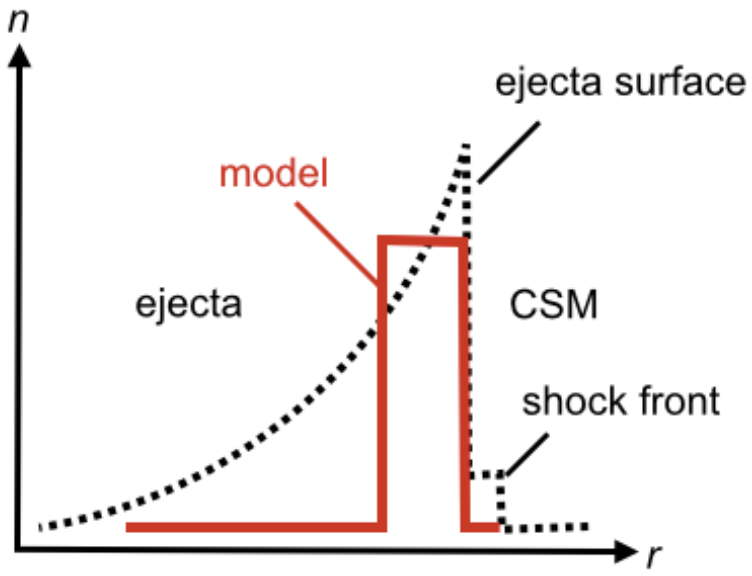

Figure 4.1: Distribution of ejecta expanding freely in the CSM (black dotted line) and the model used in this study (red solid line).

moment of breakout, the number density of the ejecta is 10^{14} cm^{-3}, and it decreases with time as t^{-3}.

4.2.1 Asymmetry

To describe the asymmetry of ejecta, I have made the following assumptions. (Fundamental configurations are similar to those of Suzuki & Shigeyama 2010b.)

- The shape of the shock follows the empirical law described by Equation (1.46). The velocities of ejecta $v_{\rm ej}$ depends on the degree of asymmetry α and direction θ as follows,

$$v_{\rm ej}(\alpha,\theta) = \frac{v_{\rm ej}(\alpha,0)}{1+(T_{\rm em}(\alpha,\theta)v_{\rm ej}(\alpha,0)/R_{\rm b})}, \tag{4.5}$$

  Since $v_{\rm ej}$ is supposed to be independent of time, the moment of shock breakout (hereafter $t_{\rm b}(\alpha,\theta)$) equals $R_{\rm b}/v_{\rm ej}(\alpha,\theta)$. Figure 4.2 shows the angular dependences of $v_{\rm ej}$ (left panel) and $t_{\rm b}$ (right panel) in cases of α=0.2, 0.5, and 0.8.

- The ejecta velocity at maximum is $v_{\rm ej}(\alpha,0) = 0.7c$.

- The optical depth at $t = t_{\rm b}$ is

$$\tau = \frac{c}{v_{\rm ej}} \approx 1.43, \tag{4.6}$$

according to (1.44).

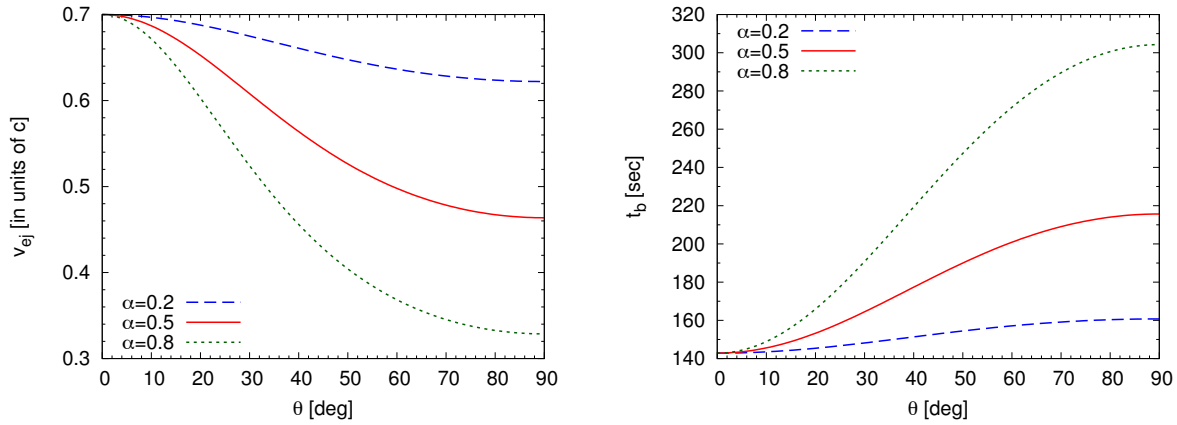

Figure 4.2: Angular dependences of the ejecta velocity $v_{\rm ej}$ (left panel) and moment of shock breakout $t_{\rm b}$ (right panel) if the shock shape is axisymmetric. Here, $v_{\rm ej}$ has the maximum value of $0.7c$ at $\theta = 0$ deg. The degree of shock asymmetry is characterized by $\alpha = 0.2$, 0.5, and 0.8.

4.2.2 Settings of Monte-Carlo calculation

- Temperature of ejecta is 1 keV at the breakout, because
  - the best-fit blackbody model for the observed spectrum of XRO 080109/SN 2008D results in the shock temperature of about 0.7 keV (Soderberg et al., 2008).
- Only inverse Compton scattering is taken into consideration, because
  - the density of the ejecta is expected to be not so high that absorption becomes dominant. (Figure 4.3 shows the energy dependence of scattering and absorption coefficients.)
- The position of the photosphere is determined to be at the outer boundary of the ejecta, because
  - the density of the ejecta is expected to be so high that the position of the photosphere will become very close to the surface of the ejecta.
- The light curve and spectrum are presented in terms of the degree of shock asymmetry α and angle Θ between the line of sight and the symmetry axis.

Figure 4.4 is the flowchart of the Monte-Carlo simulation.

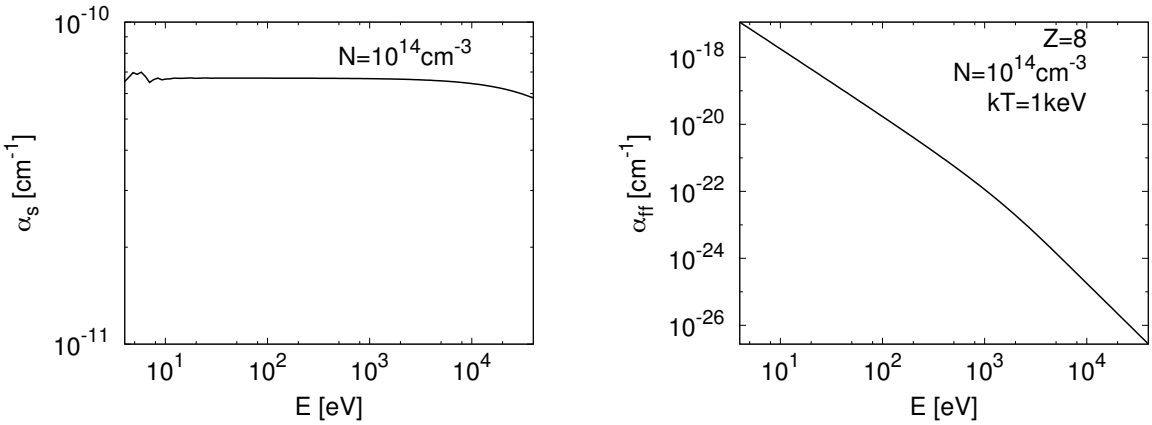

Figure 4.3: Scattering and absorption coefficients in an oxygen-rich envelope in case of $n = 1 \times 10^{14}$ cm^{-3} and $k_{\rm B}T_{\rm e} = 1$ keV.

4.3 Results

I investigate the influence of the degree of shock asymmetry α and viewing angle Θ on the spectra and light curves. In this section, I show the resultant spectra and light curves. Compared to the previous study presented by Suzuki & Shigeyama (2010b), the results of this study show different properties in the following points.

- Signature of bulk-Comptonization in spectrum depends on α and Θ (, namely, shock velocity along the line of sight).
- Timescale of light travel caused by scattering in the CSM determines the luminosity evolution after the peak.

4.3.1 Spectra

Figure 4.5 shows the resultant time-integrated spectra, averaged over three ranges of viewing angles 0 deg$<\Theta<$30 deg (top panel), 30 deg$<\Theta<$60 deg (middle panel), and 60 deg$<\Theta<$90 deg (bottom panel). For a comparison with XRO 080109, the straight lines denote power-law distributions with exponents of -2.6 and -2.0.

Compared to the primordial blackbody radiation (dash-dotted line), it is clear that the resultant spectrum has a higher-energy component due to bulk-Compton scattering, either α is 0 (spherically symmetric) or 0.5. Each of the three panel shows that larger the degree of asymmetry (α), lower the energies of scattered photons, when the shock velocity at $\theta = 0$ is fixed. In addition, for the same value of α, the photon energies decrease when the viewing angle Θ becomes larger. When α has a finite value, $dv_{\rm ej}(\alpha, \theta)/d\theta$ is negative (in the range 0

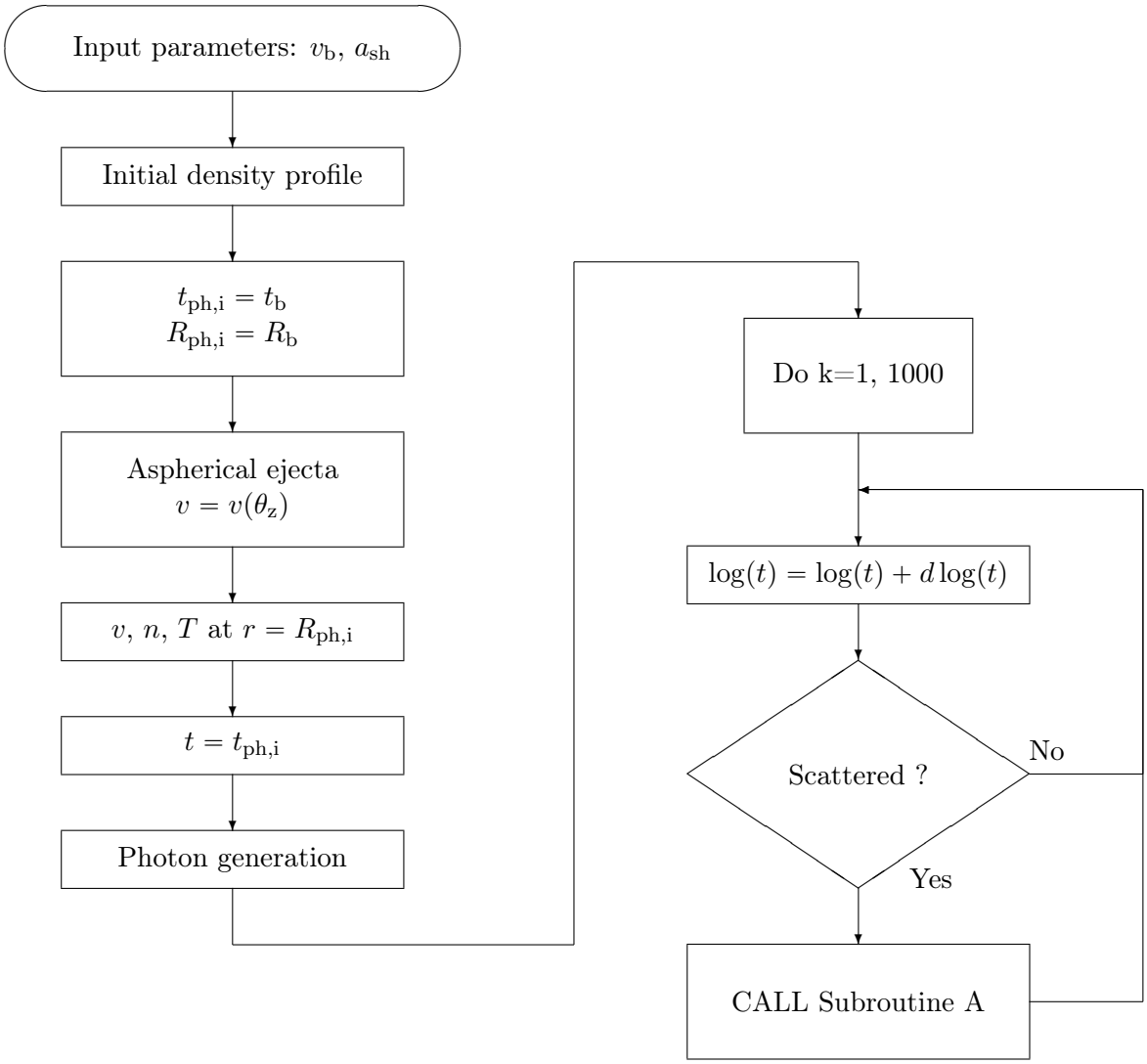

Figure 4.4: Monte-Carlo simulation for mildly-relativistic shock breakout. Definition of Subroutine A is shown in Figure 2.3.

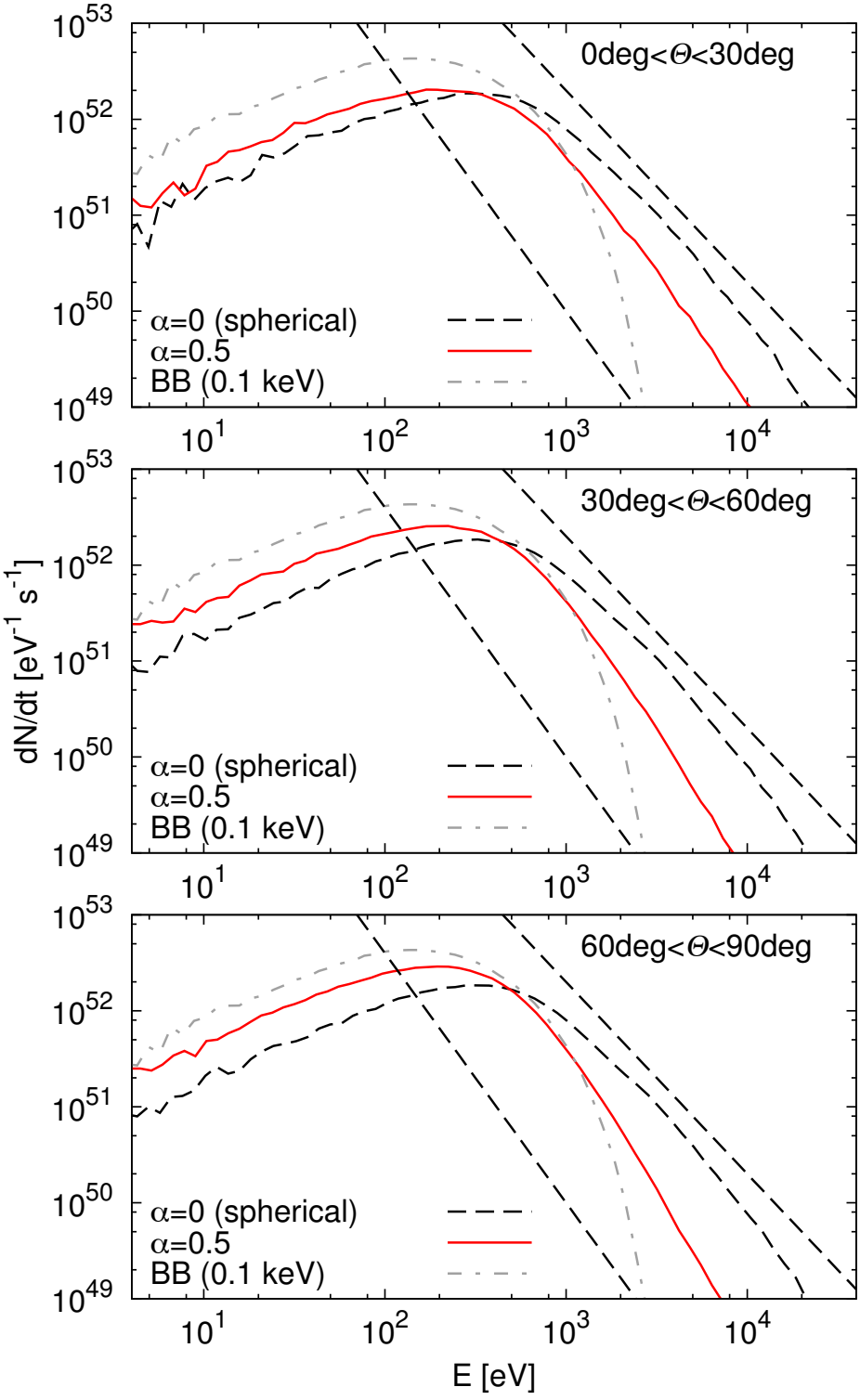

Figure 4.5: Spectra of shock breakout emission for $v_{\rm ej} = 0.7c$. The emission is averaged in the range 0 deg< Θ<30 deg (top), 30 deg< Θ<60 deg (middle), and 60 deg< Θ<90 deg (bottom). The curved dashed lines show a blackbody radiation at $T_{\rm ej} = 0.1$ keV. The straight lines display power-law distributions with indexes of -2.6 (left) and -2.0 (right), corresponding to the 1σ error given by the observation of XRO 080109/SN 2008D.

deg< Θ <90 deg). Since the bulk-Comptonization directly depends on the shock velocities, the photon energies for larger α and lower θ become smaller.

4.3.2 Light curves

Figure 4.6 displays the light curves, consisting of photons with energies above 0.2 keV and below 10 keV (to mimic the energy range covered by the Swift/XRT). Since the spectrum follows the power-law distribution in the above energy range, the majority of photons contained in the light curve seem scatter-off electrons at least once.

As referred in the previous section, when α has a finite value, the bulk-Comptonization works weaker than when $\alpha = 0$, so the energies of scattered photons becomes lower by a factor of $\lesssim 2$. From Figure 4.6, it is obvious that when $\alpha > 0$ the integration of luminosity ($E_{\rm tot}$) decreases with respect to the case of $\alpha = 0$. This seems consistent with the fact that the number of photons with energies 0.2 keV< E <10 keV becomes smaller when $\alpha > 0$. The evolution of the luminosity depends on three kinds of timescales; the shock emergence time, the light crossing time, and the timescale of photon travel (depending on electron scattering). Since most of the photons undergo the scattering, the behaviors of the whole light curves are sensitive to the timescale of photon travel $\Delta t_{\rm trv}$. The time from the onset to the peak is determined by the delay the shock emergence time $\Delta t_{\rm b}$ and the light crossing time $\Delta t_{\rm lc}$ of the emission region. Afterward, the behavior of the emission is dominated only by the diffusion of photons. The relations between the timescales and α are as follows.

- The difference in the moment of shock breakout $\Delta t_{\rm b}$ increases with α.
  - For example, when $\alpha = 0.5$ and $\Theta = 90$ deg, $\Delta t_{\rm b} \approx 60$ sec.
- When $\Theta > 30$ deg, the typical timescale of photon travel $\Delta t_{\rm trv}$ in the CSM increases with α.
  - For example, when $\alpha = 0.5$ and $\Theta = 90$ deg, $\Delta t_{\rm trv} = R_{\rm b}/v_{\rm ej} \approx 210$ sec.

On the contrary,

- The difference in the light crossing time $\Delta t_{\rm lc}$ is independent of α.
  - When $\Theta = 90$ deg, $\Delta t_{\rm lc} = R_{\rm b}/c \approx 100$ sec.

As referred in the first paragraph of this section, most of photons contained in the light curve seems to scatter off before escaping from the CSM. In this case, the timescale of photon travel can significantly influence the shape of the light curve both before and after the peak. When α is small, most scattered photons simultaneously reach the observer, and the different in the light crossing time (and the shock emergence time) becomes subdominant in

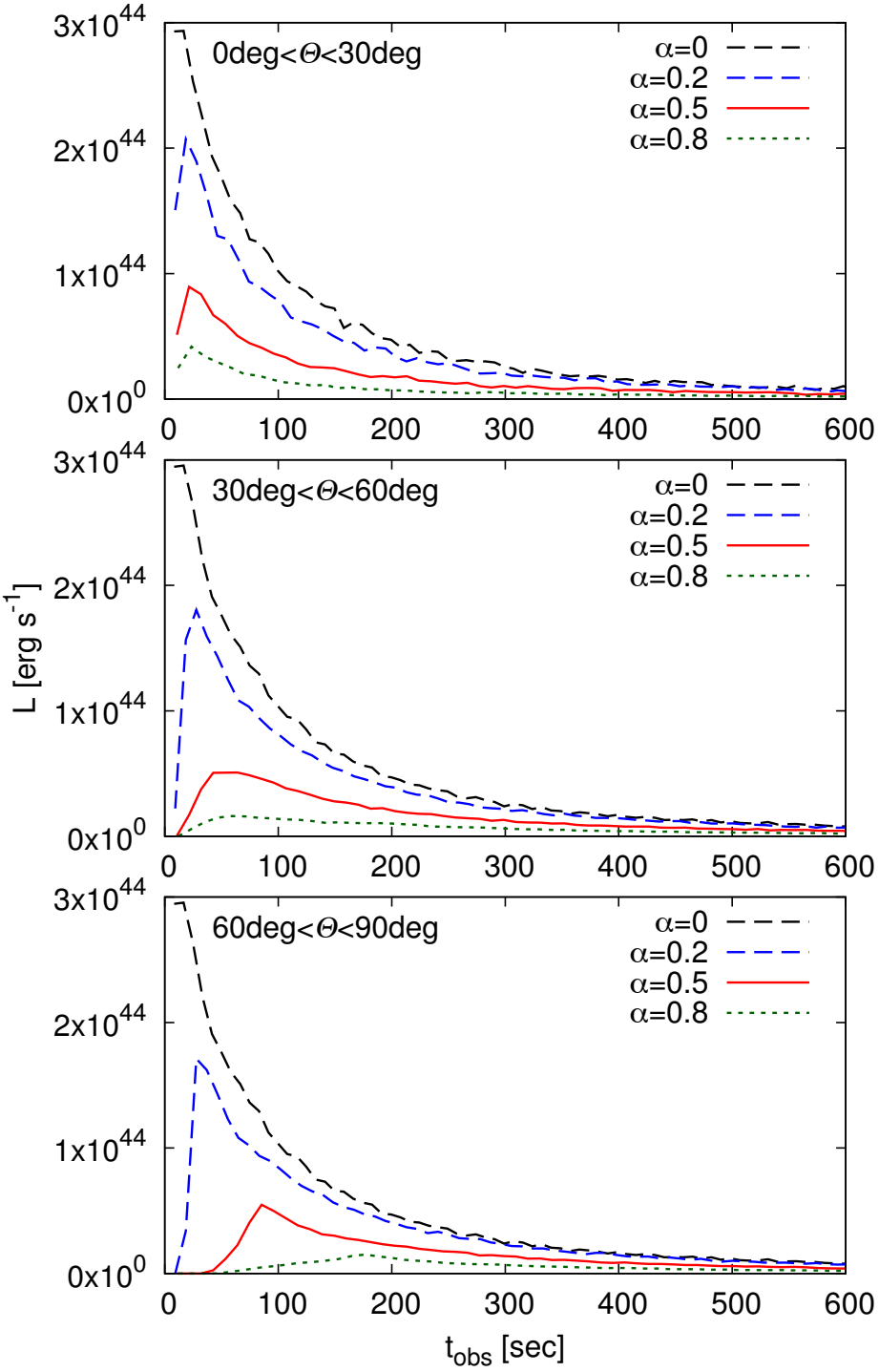

Figure 4.6: Light curves of shock breakout emission for $v_{\rm ej} = 0.7c$, in the range of 0.2 keV$< E <$10 keV.

the increasing phase. Meanwhile, when α is significantly larger than zero, the time between the onset and the peak $\Delta t_{\rm p}$ becomes close to the sum of $\Delta t_{\rm b}$ and $\Delta t_{\rm lc}$.

As a summary, there seem the following tendencies.

- When the degree of the shock asymmetry (α) becomes large,
  - $E_{\rm tot}$ decreases,
  - and $\Delta t_{\rm p}$ becomes longer.
- When the viewing angle Θ becomes large,
  - the onset delays,
  - and $\Delta t_{\rm p}$ becomes longer.

4.3.3 Comparison with XRO 080109/SN 2008D

In order to explain the observation of XRO 080109, the spectrum in the range of $1 \lesssim E \lesssim 10$ keV should have a power-law distribution with an index larger than ~ -2.6 and smaller than ~ -2.3. Red solid lines of Figure 4.5 shows that in the case of 0 deg$< \Theta <$30 deg, the slope of the spectrum resembles to the power-law distribution with index of ≈ -2.6. In the case of 60 deg$< \Theta$, the spectral slope seems significantly softer than that of XRO 080109.

On the other hand, the dependence of light curve (shape from the onset to the peak) on Θ strongly indicates that the emission of the outburst is observed from the side of the outflow, at least 30 deg$< \Theta$. In the resultant light curves (Figure 4.6), the model of $\alpha = 0.5$ seems to most closely resemble the observed light curve. Figure 4.7 show comparisons of models, in which $\alpha = 0.5$ and 60 deg$<\Theta<$90 deg, and the observed light curve of XRO 080109/SN 2008D. Figure 4.8 is the same as Figure 4.7, but for 30 deg$<\Theta<$60 deg.

The results seem to indicate that XRO 080109 was emitted from an asymmetric shock, and if the shape of the shock was axisymmetric, the angle between the line of sight and the symmetric axis is at least 30 deg. In addition, Figures 4.5 and 4.2 imply that in order to explain the spectral features of XRO 080109, the shock must propagates with velocity larger than about $0.5c$. Showing Figures 4.7 and 4.8, it seems possible to explain both the observed spectrum and light curve of XRO 080109 by an axisymmetric shock of $\alpha \approx 0.5$ and a viewing angle that larger than 30 deg and smaller than 60 deg.

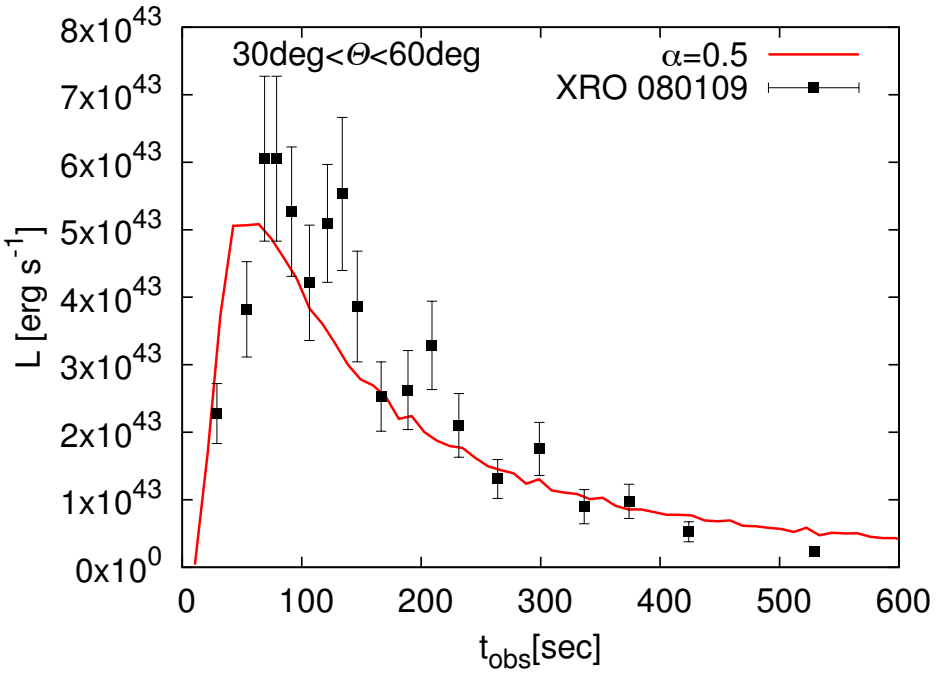

Figure 4.7: Comparison of the model in which $\alpha = 0.5$ and 30 deg$<\Theta<$60 deg with XRO 080109/SN 2008D.

4.4 Conclusions

From the calculations, I found the following tendencies of the mildly shock breakout on the degree of shock asymmetry α (from 0 to 0.8) and viewing angle Θ. Note that the shock velocity is assumed to have a constant value ($0.7c$) at $\Theta = 0$, regardless of α. When α has a large value and Θ is several tens deg,

1. Spectrum becomes less harder. (Bulk-Comptonization is weak.)

2. Peak luminosity becomes lower and the time between the onset to the peak becomes larger.

These properties would enable to obtain some information on the geometry of the shock. For example, in the case of XRO 080109/SN 2008D, the shock certainly seems to have an asymmetric (probably axisymmetric) shape. In the fiducial models, $\alpha \approx 0.5$ and $\Theta > 30$ deg are suggested. The shock of $\alpha = 0.5$ will be shaped like an ellipse of oblateness ≈ 0.3 in a plane passing through the symmetric axis. The result also shows that in the case of XRO 080109, the shock velocity along the line of sight should be larger than $0.5c$.

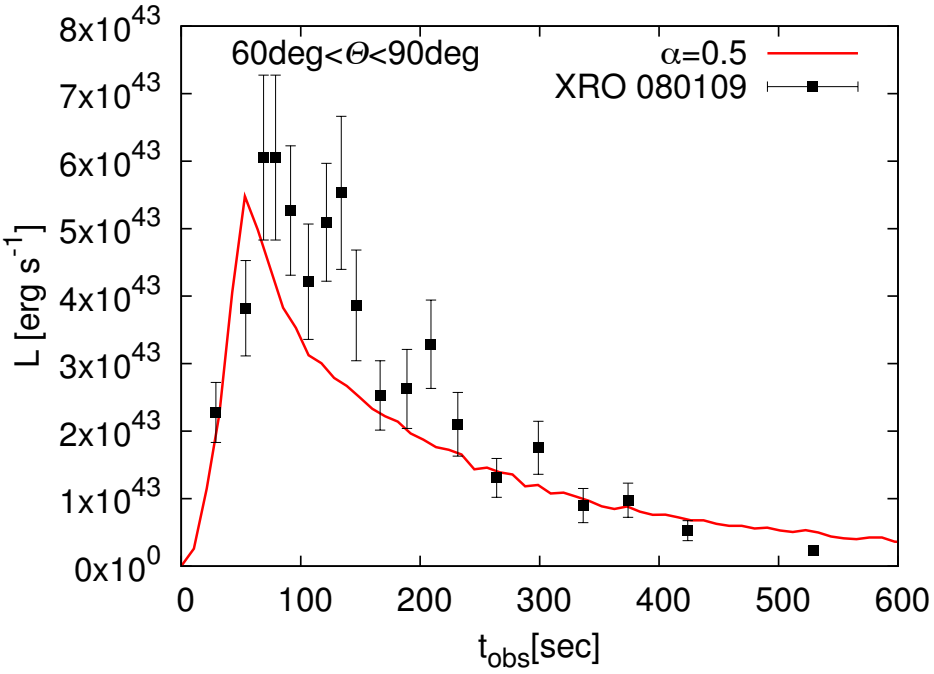

Figure 4.8: Same as Figure 4.7, but for 60 deg<Θ<90 deg.

Chapter 5

Summary and Discussions

Through a series of Monte-Carlo calculations of photons across an ultra-relativistic shock, I predict the spectral properties due to shock breakout phenomena in various circumstances. Essentiality of shock breakout for a core-collapse supernova has long been believed, although the phenomenon lasts only a short time ($\lesssim$ several seconds even when the shock velocity is non-/mildly- relativistic). Since the emission properties reflect those of the shock (such as the shape, velocity, and temperature), a study of shock breakout is regarded as an important probe of stellar explosion. In this chapter, I summarize the results of the calculations.

In Chapter 2, I investigate the properties of emission generated from an ultra-relativistic shock approaching the stellar surface. Though there is no clear observation of an ultra-relativistic shock breakout, it certainly appears when a massive progenitor dies by a jet-like explosion. Photons emitted at that moment provide information on the activity of the jet central engine through features of the shock propagation. Thus, it is worth while to predict the emission properties for future observations. However, there are only a small number of former studies that deal with ultra-relativistic shock breakout. Even none of the few exceptions calculates the spectrum taking electron scattering into consideration. Since the energy gain of photons from repeated scattering across the shock (called as bulk-Comptonization) is regard as an essential process for shock breakout, it is important to calculate the effects on the spectrum.

I calculate the effects of bulk-Comptonization on the spectrum using a Monte-Carlo method. I construct the code taking relativistic specification (e.g. Lorentz transformation) into account. In order to describe the dynamics of the shocked matter, I use a self-similar solution constructed by Nakayama & Shigeyama (2005), in which the temporal evolution of the shock is determined analytically as the shock always accelerates due to the steep density decrement toward the surface. As a result, I found that the spectrum consists of two components. The lower-energy component is a signature of thermal photons, and the higher-energy one is that of bulk-Comptonized photons. In the case that the averaged energy ($E_{\rm HE}$) of bulk-Comptonized photons is about 20–30 times higher than that ($E_{\rm LE}$) of thermal photons, there are two peaks in the spectrum. Meanwhile, in the case that $E_{\rm HE}$ is not very different from $E_{\rm LE}$, the spectrum consists of a single peak due to thermal emission

and an additional cut-off feature. Note that the ratio of $E_{\rm HE}$ and $E_{\rm LE}$ depends on two free-parameters to be specified for the Nakayama & Shigeyama solution. The deeper the depth of the shock (measured from the stellar surface) at breakout, and the smaller the shock Lorentz factor, the larger the ratio $E_{\rm HE}/E_{\rm LE}$ becomes.

As a development, I consider a possibility of relationships between ultra-relativistic shock breakouts and observed l-GRBs. A comparison shows that in the energy range higher than 1 MeV, some of the resultant spectra resemble the typical GRB spectrum (the Band function). On the other hand, the shape of the lower-energy components are not similar to the Band function at all. Additionally, the duration of ultra-relativistic shock breakout is shorter than 1 sec and the total radiation energy $E_{\rm tot}$ is as small as 10^{49} erg. Both of them are inconsistent with long duration GRBs, in which the durations are at least 2 sec and $E_{\rm tot} \approx 10^{51}$ erg. Thus, it is obvious that ultra-relativistic shock breakouts can not explain the entire prompt emission of l-GRBs.

In Chapter 3, I examine the properties of ultra-relativistic shock breakout in the CSM. As suggested by a fortunate observation (XRO 080109/SN 2008D), shock breakout would occur also in a dense CSM. Thus, investigating the spectrum of an ultra-relativistic shock breakout in the CSM can be intriguing. In the case of a CSM, the temporal evolution of the forward shock is determined by the density profile and the rate L of energy injection into the contact discontinuity between ejecta and the CSM, according to a self-similar solution of Blandford & McKee (1976). The shock accelerates if $dL/dt > 0$ and decelerates if $dL/dt < 0$. Accordingly, it might be possible to obtain some pieces of information on the central engine of the jet from the properties of shock breakout emission.

I calculate the spectrum of scattered photons and its temporal evolution using the Monte-Carlo code introduced in Chapter 2. The results show that if the shock decelerates, photons with energies higher than $\approx$ 100 MeV tend to appear in the beginning of shock breakout. This is because the bulk kinetic energy of shocked matter or ejecta significantly decreases with time. On the other hand, if the shock accelerates, photons with only a tiny transverse momentum are overtaken by the shock immediately after their generation, and can not escape out until the entire CSM becomes transparent. In this case, there are only slight changes in the spectrum. In comparison to the general properties of l-GRBs, it might be difficult to reproduce the low-energy spectral components ($<$ 1 MeV).

In Chapter 4, I study the dependence of mildly-relativistic shock breakout on shock asymmetry and the viewing angle Θ, aiming at explaining the observation of XRO 080109/SN 2008D. XRO 080109 is believed as shock breakout emission generated from a mildly-relativistic shock. A former study suggests that the shape of the observed light curve might be evidence of shock asymmetry. Since the former studies do not reproduce both of the observed spectrum and light curve using a hydrodynamical model, it might be important to try that.

I perform a Monte-Carlo calculation using an axisymmetric (ellipsoidal) shock model and compare the results with the observed properties (spectrum and light curve) of XRO 080109/SN 2008D. The resultant light curves suggest that the observed shape with a rapid rise and slow decline prefers oblate shock fronts (with an oblateness of $\sim$0.3) to the spherical one and that the viewing angle is $\sim$30 deg off the symmetry axis. The observed spectrum implies the shock velocity along the line of sight greater than $0.5c$.

The results of calculations would suggest that in principle, it might be possible to obtain some pieces of information on the central engine activity of a jet from observable properties of ultra-relativistic shock breakout. Nonetheless, in order to utilize the model in analysis of an observation, it is necessary to overcome many questions and difficulties. For example, the assumptions in the model may cause significant uncertainties in the calculation, such as mutual influences between fluid dynamics and radiative transfer. Furthermore, if an observation is analyzed in the context of this study, careful arguments will be required to clarify if the source of observed high-energy emission is really the shock propagation.

Shock breakout itself is a phenomenon independent of l-GRB. In this thesis, I examine a possibility of a contribution of shock breakout to the observed l-GRB. If supposing that there is a relationship between the two phenomena, it might be possible to interpret the high-energy emission of ultra-relativistic shock breakout at the stellar surface (mentioned in Chapter 2) as the high-energy tail of an observed Band spectrum. If the interpretation is right, the low-energy tail of the Band spectrum might be explained by considering the subsequent thermal radiation emitted from ejecta. While in this thesis the calculations do not take account of effects of radiation loss on fluid evolution, coupling calculations of the hydrodynamics and radiation are desirable in future work.

Though there remain some subjects such as model uncertainties, I examine the properties of ultra- (and mildly-) relativistic shock breakout and relate them with the geometry of explosions, the size of the progenitors, and the activities of the central engines.

References

Abdo, A. A., Ackermann, M., Ajello, M., et al. 2009a, ApJ, 706, L138

—. 2009b, ApJS, 183, 46

Ackermann, M., Asano, K., Atwood, W. B., et al. 2010, ApJ, 716, 1178

Ackermann, M., Ajello, M., Asano, K., et al. 2013, ApJ, 763, 71

Akiyama, S., Wheeler, J. C., Meier, D. L., & Lichtenstadt, I. 2003, ApJ, 584, 954

Amati, L. 2006, MNRAS, 372, 233

Amati, L., Frontera, F., & Guidorzi, C. 2009, A&A, 508, 173

Amati, L., Guidorzi, C., Frontera, F., et al. 2008, MNRAS, 391, 577

Amati, L., Frontera, F., Tavani, M., et al. 2002, A&A, 390, 81

Atwood, W. B., Abdo, A. A., Ackermann, M., et al. 2009, ApJ, 697, 1071

Axelsson, M., Baldini, L., Barbiellini, G., et al. 2012, ApJ, 757, L31

Band, D., Matteson, J., Ford, L., et al. 1993, ApJ, 413, 281

Band, D. L., Axelsson, M., Baldini, L., et al. 2009, ApJ, 701, 1673

Barthelmy, S. D., Cannizzo, J. K., Gehrels, N., et al. 2005, ApJ, 635, L133

Beloborodov, A. M. 2010, MNRAS, 407, 1033

Bethe, H. A., & Wilson, J. R. 1985, ApJ, 295, 14

Bisnovatyi-Kogan, G. S., Popov, I. P., & Samokhin, A. A. 1976, Ap&SS, 41, 287

Blandford, R. D., & McKee, C. F. 1976, Physics of Fluids, 19, 1130

Bludman, S. A., & van Riper, K. A. 1977, ApJ, 212, 859

Bosnjak, Z., Celotti, A., & Ghirlanda, G. 2006, MNRAS, 370, L33

Briggs, M. S., Band, D. L., Kippen, R. M., et al. 1999, ApJ, 524, 82

Buras, R., Rampp, M., Janka, H.-T., & Kifonidis, K. 2003, Physical Review Letters, 90, 241101

Burrows, A., Dessart, L., Livne, E., Ott, C. D., & Murphy, J. 2007, ApJ, 664, 416

Burrows, A., Hayes, J., & Fryxell, B. A. 1995, ApJ, 450, 830

References

Burrows, D. N., Hill, J. E., Nousek, J. A., et al. 2005, Space Sci. Rev., 120, 165

Butler, N. R., Kocevski, D., & Bloom, J. S. 2009, ApJ, 694, 76

Butler, N. R., Kocevski, D., Bloom, J. S., & Curtis, J. L. 2007, ApJ, 671, 656

Castignani, G., Guetta, D., Pian, E., et al. 2014, A&A, 565, A60

Castro-Tirado, A. J., & Gorosabel, J. 1999, A&AS, 138, 449

Catchpole, R. M., Menzies, J. W., Monk, A. S., et al. 1987, MNRAS, 229, 15P

Cavallo, G., & Rees, M. J. 1978, MNRAS, 183, 359

Chevalier, R. A. 1982, ApJ, 258, 790

Chevalier, R. A., Blondin, J. M., & Emmering, R. T. 1992, ApJ, 392, 118

Chevalier, R. A., & Fransson, C. 1987, Nature, 328, 44

Chevalier, R. A., & Liang, E. P. 1989, ApJ, 344, 332

Costa, E., Frontera, F., Heise, J., et al. 1997, Nature, 387, 783

Crotts, A. P. S., Landsman, W. B., Bohlin, R. C., et al. 1992, ApJ, 395, L25

Crowther, P. A. 2007, ARA&A, 45, 177

Dainotti, M., Petrosian, V., Willingale, R., et al. 2015a, MNRAS, 451, 3898

Dainotti, M. G., Cardone, V. F., Piedipalumbo, E., & Capozziello, S. 2013, MNRAS, 436, 82

Dainotti, M. G., Del Vecchio, R., Shigehiro, N., & Capozziello, S. 2015b, ApJ, 800, 31

Ensman, L., & Burrows, A. 1992, ApJ, 393, 742

Falk, S. W. 1978, ApJ, 225, L133

Fishman, G. J., Meegan, C. A., Wilson, R. B., et al. 1994, ApJS, 92, 229

Flath, D. L., Johnson, T. S., Turri, M., & Heidenreich, K. A. 2009, in Astronomical Society of the Pacific Conference Series, Vol. 411, Astronomical Data Analysis Software and Systems XVIII, ed. D. A. Bohlender, D. Durand, & P. Dowler, 193

Fong, W., Berger, E., Margutti, R., et al. 2012, ApJ, 756, 189

Frail, D. A., Kulkarni, S. R., Sari, R., et al. 2001, ApJ, 562, L55

Fransson, C., & Lundqvist, P. 1989, ApJ, 341, L59

Fransson, C., Larsson, J., Migotto, K., et al. 2015, ApJ, 806, L19

Fryer, C. L., & Warren, M. S. 2002, ApJ, 574, L65

References

Gehrels, N., Ramirez-Ruiz, E., & Fox, D. B. 2009, ARA&A, 47, 567

Gehrels, N., Chincarini, G., Giommi, P., et al. 2004, ApJ, 611, 1005

Ghirlanda, G., Celotti, A., & Ghisellini, G. 2003, A&A, 406, 879

Ghirlanda, G., Ghisellini, G., Firmani, C., Celotti, A., & Bosnjak, Z. 2005, MNRAS, 360, L45

Ghirlanda, G., Ghisellini, G., & Lazzati, D. 2004, ApJ, 616, 331

Goldstein, A., Preece, R. D., Mallozzi, R. S., et al. 2013, ApJS, 208, 21

Goldstein, A., Burgess, J. M., Preece, R. D., et al. 2012, ApJS, 199, 19

Goodman, J. 1986, ApJ, 308, L47

Greiner, J. 1999, Mem. Soc. Astron. Italiana, 70, 891

Guidorzi, C., Frontera, F., Montanari, E., et al. 2005, MNRAS, 363, 315

—. 2006, MNRAS, 371, 843

Guidorzi, C., Lacapra, M., Frontera, F., et al. 2011, A&A, 526, A49

Guiriec, S., Briggs, M. S., Connaugthon, V., et al. 2010, ApJ, 725, 225

Guiriec, S., Connaughton, V., Briggs, M. S., et al. 2011, ApJ, 727, L33

Guiriec, S., Daigne, F., Hascoët, R., et al. 2013, ApJ, 770, 32

Hamuy, M., Suntzeff, N. B., Gonzalez, R., & Martin, G. 1988, AJ, 95, 63

Hanke, F., Müller, B., Wongwathanarat, A., Marek, A., & Janka, H.-T. 2013, ApJ, 770, 66

Herant, M., Benz, W., Hix, W. R., Fryer, C. L., & Colgate, S. A. 1994, ApJ, 435, 339

Ito, H., Nagataki, S., Matsumoto, J., et al. 2014, ApJ, 789, 159

Janka, H.-T. 2001, A&A, 368, 527

Janka, H.-T., & Mueller, E. 1996, A&A, 306, 167

Johnson, H. L., & Morgan, W. W. 1953, ApJ, 117, 313

Johnson, M. H., & McKee, C. F. 1971, Phys. Rev. D, 3, 858

Kaneko, Y., Preece, R. D., Briggs, M. S., et al. 2006, ApJS, 166, 298

Kirshner, R. P., Sonneborn, G., Crenshaw, D. M., & Nassiopoulos, G. E. 1987, ApJ, 320, 602

Kitaura, F. S., Janka, H.-T., & Hillebrandt, W. 2006, A&A, 450, 345

Klebesadel, R. W., Strong, I. B., & Olson, R. A. 1973, ApJ, 182, L85

References

Klein, R. I., & Chevalier, R. A. 1978, ApJ, 223, L109

Kouveliotou, C., Meegan, C. A., Fishman, G. J., et al. 1993, ApJ, 413, L101

Kunkel, W., Madore, B., Shelton, I., et al. 1987, IAU Circ., 4316, 1

Landau, L. D., & Lifshitz, E. M. 1959,

LeBlanc, J. M., & Wilson, J. R. 1970, ApJ, 161, 541

Liang, E. W., Zhang, B., O'Brien, P. T., et al. 2006, ApJ, 646, 351

Liebendörfer, M., Mezzacappa, A., Thielemann, F.-K., et al. 2001, Phys. Rev. D, 63, 103004

Lundman, C., Pe'er, A., & Ryde, F. 2013, MNRAS, 428, 2430

Lundqvist, P., & Fransson, C. 1991, ApJ, 380, 575

—. 1996, ApJ, 464, 924

Margutti, R., Zaninoni, E., Bernardini, M. G., et al. 2013, MNRAS, 428, 729

Massaro, F., Cutini, S., Conciatore, M. L., & Tramacere, A. 2008, in American Institute of Physics Conference Series, Vol. 1000, American Institute of Physics Conference Series, ed. M. Galassi, D. Palmer, & E. Fenimore, 84–87

Massey, P. 1984, ApJ, 281, 789

Meegan, C., Lichti, G., Bhat, P. N., et al. 2009, ApJ, 702, 791

Meier, D. L., Epstein, R. I., Arnett, W. D., & Schramm, D. N. 1976, ApJ, 204, 869

Menzies, J. W., Catchpole, R. M., van Vuuren, G., et al. 1987, MNRAS, 227, 39P

Mészáros, P., & Rees, M. J. 2000, ApJ, 530, 292

—. 2011, ApJ, 733, L40

Metzger, M. R., Djorgovski, S. G., Kulkarni, S. R., et al. 1997, Nature, 387, 878

Mezzacappa, A. 2005, Annual Review of Nuclear and Particle Science, 55, 467

Mezzacappa, A., Calder, A. C., Bruenn, S. W., et al. 1998, ApJ, 493, 848

Michelson, P. F., Atwood, W. B., & Ritz, S. 2010, Reports on Progress in Physics, 73, 074901

Müller, B. 2015, MNRAS, 453, 287

Müller, B., Janka, H.-T., & Heger, A. 2012, ApJ, 761, 72

Nakar, E., & Sari, R. 2010, ApJ, 725, 904

—. 2012, ApJ, 747, 88

Nakayama, K., & Shigeyama, T. 2005, ApJ, 627, 310

Nava, L., Ghirlanda, G., Ghisellini, G., & Celotti, A. 2011, A&A, 530, A21

Norris, J. P., Marani, G. F., & Bonnell, J. T. 2000, ApJ, 534, 248

Nousek, J. A., Kouveliotou, C., Grupe, D., et al. 2006, ApJ, 642, 389

O'Brien, P. T., & Willingale, R. 2007, Royal Society of London Philosophical Transactions Series A, 365, 1179

O'Brien, P. T., Willingale, R., Osborne, J., et al. 2006, ApJ, 647, 1213

Ohtani, Y., Suzuki, A., & Shigeyama, T. 2013, ApJ, 777, 113

Paciesas, W. S., Meegan, C. A., Pendleton, G. N., et al. 1999, ApJS, 122, 465

Paczynski, B. 1986, ApJ, 308, L43

Pan, M., & Sari, R. 2006, ApJ, 643, 416

Patat, F., & Piemonte, A. 1998, IAU Circ., 6918, 1

Pe'er, A. 2008, ApJ, 682, 463

Pe'er, A., Mészáros, P., & Rees, M. J. 2006, ApJ, 642, 995

Piran, T. 2003, Nature, 422, 268

Pomraning, G. C. 1973,

Preece, R. D., Briggs, M. S., Mallozzi, R. S., et al. 1998, ApJ, 506, L23

—. 2000, ApJS, 126, 19

Rampp, M., & Janka, H.-T. 2000, ApJ, 539, L33

Rees, M. J., & Mészáros, P. 2005, ApJ, 628, 847

Reichart, D. E., Lamb, D. Q., Fenimore, E. E., et al. 2001, ApJ, 552, 57

Ruderman, M. 1975, in Annals of the New York Academy of Sciences, Vol. 262, Seventh Texas Symposium on Relativistic Astrophysics, ed. P. G. Bergman, E. J. Fenyves, & L. Motz, 164–180

Ruffini, R., Siutsou, I. A., & Vereshchagin, G. V. 2013, ApJ, 772, 11

Rybicki, G. B., & Lightman, A. P. 1979, Radiative processes in astrophysics

Ryde, F. 2004, ApJ, 614, 827

Ryde, F., Pe'Er, A., Nymark, T., et al. 2011, MNRAS, 415, 3693

Sakurai, A. 1960, Communications on Pure and Applied Mathematics, 13, 353

References

Sari, R., Piran, T., & Narayan, R. 1998, ApJ, 497, L17

Schaefer, B. E. 1987, ApJ, 323, L47

Schmidt, W. K. H. 1978, Nature, 271, 525

Shemi, A., & Piran, T. 1990, ApJ, 365, L55

Shigeyama, T., & Nomoto, K. 1990, ApJ, 360, 242

Shu, F. H. 1992,

Smith, L. F. 1968, MNRAS, 138, 109

Soderberg, A. M., Berger, E., Page, K. L., et al. 2008, Nature, 453, 469

Sonbas, E., MacLachlan, G. A., Shenoy, A., Dhuga, K. S., & Parke, W. C. 2013, ApJ, 767, L28

Sumiyoshi, K., Yamada, S., Suzuki, H., et al. 2005, ApJ, 629, 922

Suntzeff, N. B., & Bouchet, P. 1990, AJ, 99, 650

Suwa, Y., Kotake, K., Takiwaki, T., et al. 2010, PASJ, 62, L49

Suzuki, A., & Shigeyama, T. 2010a, ApJ, 719, 881

—. 2010b, ApJ, 717, L154

Tagliaferri, G., Goad, M., Chincarini, G., et al. 2005, Nature, 436, 985

Takiwaki, T., Kotake, K., & Suwa, Y. 2012, ApJ, 749, 98

Tan, J. C., Matzner, C. D., & McKee, C. F. 2001, ApJ, 551, 946

Taub, A. H. 1948, Physical Review, 74, 328

Thompson, C. 1994, MNRAS, 270, 480

Thompson, C., Mészáros, P., & Rees, M. J. 2007, ApJ, 666, 1012

Thompson, T. A., Quataert, E., & Burrows, A. 2005, ApJ, 620, 861

Wang, L., & Wheeler, J. C. 1998, ApJ, 504, L87

Wheeler, J. C., Meier, D. L., & Wilson, J. R. 2002, ApJ, 568, 807

Woltjer, L. 1972, ARA&A, 10, 129

Woosley, S. E., Heger, A., & Weaver, T. A. 2002, Reviews of Modern Physics, 74, 1015

Yonetoku, D., Murakami, T., Nakamura, T., et al. 2004, ApJ, 609, 935

Zhang, B., Fan, Y. Z., Dyks, J., et al. 2006, ApJ, 642, 354

Zhang, B., & Mészáros, P. 2001, ApJ, 552, L35

—. 2002, ApJ, 581, 1236

Appendix A

Properties of the Swift & Fermi telescope

A.1 Swift

The Swift satellite consists of one wide field camera and two narrow field spectrometers (see Figure A.1); Burst Alert Telescope (BAT), X-Ray Telescope (XRT), and Ultra Violet-Optical Telescope (UVOT) (Gehrels et al., 2004). The BAT, watching about 1/10 (1.4 steradian) of the sky at a time, provides the position of a newborn transient only a few sec after the detection. Then, the XRT and the UVOT automatically slew towards the source so that they would be ready for the afterglow within several tens of sec. Tables A.1 & A.2 shows the timeline of an observation and the summary of the three instruments. Ground-based telescopes can receive the information as soon as the initial BAT localization has finished.

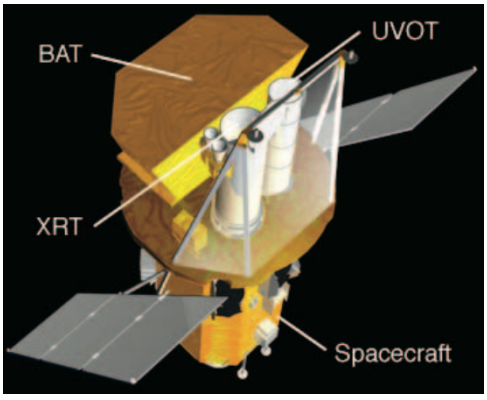

Figure A.1: The swift satellite image (Gehrels et al., 2004).

Table A.1: Timeline of the *Swift* observation (http://swift.gsfc.nasa.gov).

Time (sec)	Event
0	GRB detection
20	Slew begins
20	BAT approx. location distributed
~ 50	GRB acquired
70	XRT location distributed
240	UVOT finding chart distributed
300	XRT lightcurve distributed
1200	XRT spectrum distributed
~ 60,000	All automated observations complete (20,000 sec exposure)

Table A.2: Properties of the *Swift* instruments (Gehrels et al., 2004).

	BAT	XRT	UVOT
Telescope	-	Wolter I	Modified RC[1]
Detector	CdZnTe	XMM EPIC CCD	Intensified CCD
Detection area	5240 cm^{-2}	-	-
Aperture	Coded mask	-	30 cm diameter
Detector operation[2]	PC	PC, II, & RT	PC
Field of view (FoV)	1.4 sr	23.6 ^{sec}×23.6 ^{sec}	17 ^{sec}×17 ^{sec}
Location accuracy	1 ^{sec}-4 ^{sec}	5 ^{sec}	0.3 ^{sec}
Energy range (or Wavelength)	15–150 keV	0.2–10 keV	170–600 nm
Energy (/Spectral) resolution	∼ 7 keV	-	∼200 at 400 nm
Detection rate	> 100 yr^{-1}	-	-
Sensitivity	10^{-8} erg cm^{-2} s^{-1}	2×10^{-14} erg cm^{-2} in 10^4 sec	B=24 in white light in 1000 sec

[1] Ritchey-Chétien.
[2] PC: Photon Counting, II: Integrated Imaging, RT: Rapid Timing.

A.2 Fermi

The *Fermi* has two instrument; the Large Area Telescope (LAT) and the Gamma-ray Burst Monitor (GBM) (Michelson et al., 2010; Atwood et al., 2009; Meegan et al., 2009; Flath et al., 2009). The LAT is an wide field of view (2.4 sr), imaging pair-conversion detector for photons in the energy range from 20 MeV to 300 GeV. The GBM is for photons of relatively lower energy (from 8 keV to 40 MeV), covering the Band spectral break energy. The GBM plays key role in notification and localization of bursts. Ground-based telescopes obtain the information through the GRB Coordinates Network (GCN). Table A.3, A.3 list the capabilities of the LAT and GBM. Table A.5 shows the general notification of the GCN starting from the GBM trigger.

Table A.3: *Fermi*/LAT properties (Atwood et al., 2009).

Parameter	Value or Range
Energy range	20 MeV–300 GeV
Effective area at normal incidence[a]	9,500 cm^2
Energy resolution (equivalent Gaussian 1σ):	
100 MeV–1 GeV (on-axis)	9%–15%
1 GeV–10 GeV (on-axis)	8%–9%
10 GeV–300 GeV (on-axis)	8.5%–18%
>10 GeV (>60° incidence)	⩽6%
Single photon angular resolution (space angle)	
on-axis, 68% containment radius:	
>10 GeV	⩽0.°15
1 GeV	0.°6
100 MeV	3.°5
on-axis, 95% containment radius	$< 3 \times \theta_{68\%}$
off-axis containment radius at 55°	< 1.7× on-axis value
Field of View (FoV)	2.4 sr
Timing accuracy	< 10 μs
Event readout time (dead time)	26.5 μs
GRB location accuracy onboard[b]	< 10′
GRB notification time to spacecraft[c]	<5 sec
Point source location determination[d]	< 0.′5
Point source sensitivity (>100 MeV)[e]	3×10^{-9} ph cm^{-2} s^{-1}

Notes.

[a] Maximum (as a function of energy) effective area at normal incidence. Includes inefficiencies necessary to achieve required background rejection. Effective area peak is typically in the 1 to 10 GeV range.

[b] For burst (<20 s duration) with >100 photons above 1 GeV. This corresponds to a burst of ∼5 cm^{-2} s^{-1} peak rate in the 50 – 300 keV band assuming a spectrum of broken power law at 200 keV from photon index of –0.9 to –2.0. Such bursts are estimated to occur in the LAT FoV ∼10 times per year.

[c] Time relative to detection of GRB.

[d] High latitude source of 10^{-7} cm^{-2} s^{-1} flux at >100 MeV with a photon spectral index of –2.0 above a flat background and assuming no spectral cutoff at high energy; 1σ radius; one-year survey.

[e] For a steady source after one-year sky survey, assuming a high-latitude diffuse flux of 1.5×10^{-5} cm^{-2} s^{-1} sr^{-1} (>100 MeV) and a photon spectral index of –2.1, with no spectral cutoff.

Table A.4: *Fermi*/GBM properties (Meegan et al., 2009).

Energy resolution (FWHM)	~15% at 100 keV; ~10% at 1 MeV
High-rate performance	<2% distortion at 50,000 cps
Energy range	8 keV to 40 MeV
On-board trigger threshold	0.74 photons cm^{-2} s^{-1}
On-board burst location error	<15 deg
Burst trigger rate	~260 per year
Dead time per event	2.6 μs

Table A.5: GCN notifications due to the *Fermi*/GBM (Meegan et al., 2009).

Notice Type	Information Provided
Fermi-GBM alert	Trigger time, energy range, significance; detectors triggered, spacecraft lat. and long.
Fermi-GBM flight position	On-board computed localization (R.A. and decl. plus spacecraft coordinates), classification, intensity, hardness ratio
Fermi-GBM ground position	On-ground computed localization (R.A. and decl. plus spacecraft coordinates)
Fermi-GBM ground internal	Diagnostic data (sent to GBM team only)

Appendix B

Equations of fluid dynamics

For a perfect gas, the energy momentum tensor $T^{\mu\nu}$ in the rest frame of the gas is expressed as follows.

$$T^{\mu\nu} = \begin{pmatrix} \rho c^2 & 0 & 0 & 0 \\ 0 & p & 0 & 0 \\ 0 & 0 & p & 0 \\ 0 & 0 & 0 & p \end{pmatrix}, \tag{B.1}$$

where ρ is the energy density ρ, p the pressure (i.e. Landau & Lifshitz, 1959). In a frame moving in an arbitrary direction, the tensor $T^{\mu\nu}$ is derived by the Lorentz transformation of Equation (B.1). If the frame moves with the four-velocity u^μ,

$$T^{\mu\nu} = \left(\rho + \frac{p}{c^2}\right) u^\mu u^\nu + p\eta^{\mu\nu} \qquad (\mu, \nu = 0, \ldots, 3), \tag{B.2}$$

where $\eta^{\mu\nu}$ denotes the Minkowski metric. Each component corresponds to the energy density (T^{00}), the energy flux in the each (ν-th) direction ($T^{0\nu}$), the three-momentum density ($T^{\mu 0}$), and the three-momentum stress ($T^{\mu\nu}$). The change rates of the energy and momentum are derived by the divergence of $T^{\mu\nu}$, so the conservation laws are written as follows.

$$\frac{\partial T^{\mu\nu}}{\partial x^\nu} = 0. \tag{B.3}$$

The equation of continuity is derived from the divergence of the number flux $\boldsymbol{n}$. Since the number flux is written by

$$\boldsymbol{n} = n\boldsymbol{u}, \tag{B.4}$$

where $\boldsymbol{u}$ is the four-velocity, the equation of continuity is

$$\frac{\partial}{\partial x^\nu}(n\boldsymbol{u}) = 0. \tag{B.5}$$

In a plane-parallel model, the conservation laws of energy and momentum are expressed as following equations.

$$\begin{aligned}
\frac{\partial T^{0\nu}}{\partial x^{\nu}} &= \frac{\partial T^{00}}{\partial (ct)} + \frac{\partial T^{01}}{\partial x} \\
&= \frac{1}{c}\frac{\partial}{\partial t}\left[\gamma^2(\rho c^2 + p\beta^2)\right] + \frac{\partial}{\partial x}\left[\gamma^2(\rho c^2 + p)\beta\right] \\
&= \frac{1}{c}\frac{\partial}{\partial t}\left[\gamma^2(e + p\beta^2)\right] + \frac{\partial}{\partial x}\left[\gamma^2(e + p)\beta\right] = 0, \qquad \text{(B.6)} \\
\frac{\partial T^{1\nu}}{\partial x^{\nu}} &= \frac{\partial T^{10}}{\partial (ct)} + \frac{\partial T^{11}}{\partial x} \\
&= \frac{1}{c}\frac{\partial}{\partial t}\left[\gamma^2(\rho c^2 + p)\beta\right] + \frac{\partial}{\partial x}\left[\gamma^2(\rho c^2 + p)\beta^2\right] + \frac{\partial p}{\partial x} \\
&= \frac{1}{c}\frac{\partial}{\partial t}\left[\gamma^2(e + p)\beta\right] + \frac{\partial}{\partial x}\left[\gamma^2(e + p)\beta^2\right] + \frac{\partial p}{\partial x} = 0, \qquad \text{(B.7)}
\end{aligned}$$

where γ is the Lorentz factor of the fluid, β the velocity in units of c, and e the internal energy per unit mass. The equation of continuity is written by

$$\frac{1}{c}\frac{\partial n'}{\partial t} + \frac{\partial}{\partial x}\left(\beta n'\right) = 0, \qquad \text{(B.8)}$$

where $n' = n\gamma$.

In a spherically symmetric model, the equations of fluid dynamics are expressed as follows.

$$\frac{\partial T^{00}}{\partial (ct)} + \frac{1}{r^2}\frac{\partial (r^2 T^{0\nu})}{\partial r} = \frac{1}{c}\frac{\partial}{\partial t}\gamma^2\left[e + p\beta^2\right] + \frac{1}{r^2}\frac{\partial}{\partial r}\gamma^2\left[r^2(e + p)\beta\right] = 0, \qquad \text{(B.9)}$$

$$\frac{\partial T^{10}}{\partial (ct)} + \frac{1}{r^2}\frac{\partial (r^2 T^{1\nu})}{\partial r} = \frac{\partial}{\partial t}\gamma^2\left[(e + p)\beta\right] + \frac{1}{r^2}\frac{\partial}{\partial r}\gamma^2\left[r^2(e + p)\beta^2\right] + \frac{\partial p}{\partial r} = 0, \qquad \text{(B.10)}$$

$$\frac{1}{c}\frac{\partial n'}{\partial t} + \frac{1}{r^2}\frac{\partial}{\partial x}\left(r^2\beta n'\right) = 0. \qquad \text{(B.11)}$$

B.1 Hydrodynamics in the relativistic limits

In this section, I describe the expressions of the basic equations of ultra-relativistic fluids.

B.1.1 At the stellar surface

Near the stellar surface, the basic equations of the shocked matter is expressed by Equations (B.6)– (B.8). In the relativistic limit, the equation of state of an ideal Fermi gas is expressed as follows (Bludman & van Riper, 1977).

$$e = 3p \qquad \text{(B.12)}$$

When $\gamma \gg 1$, a combination of the four equations can yields three ordinary differential equations (2.2)–(2.4). In the conversion, the following two approximations of β ($\gamma \to 1$) are used.

$$\beta \to 1 - \frac{1}{2\gamma^2}, \quad \beta^2 \to 1 - \frac{1}{\gamma^2}, \tag{B.13}$$

and the relation between the Lagrangian description and the Euler one,

$$\frac{d}{dt} = \frac{\partial}{\partial t} + \beta \frac{\partial}{\partial x}. \tag{B.14}$$

B.1.2 In the CSM

In the case of the spherically symmetric fluid model, the basic equations (B.9)–(B.11) can be converted to the ordinary differential equations by almost the same arrangements as referred in the previous chapter. The convective derivative is

$$\frac{d}{dt} = \frac{\partial}{\partial t} + \beta \frac{\partial}{\partial r}. \tag{B.15}$$

Then, Equation (3.1)–(3.3) are derived as the basic equations.

B.2 Boundary condition

The boundary condition at the shock surface is given by the Rankine-Hugoniot condition in the relativistic limit (Taub, 1948),

$$[v] = -\frac{j}{W_s}\left[\frac{1}{D}\right] \tag{B.16}$$

$$[p] = \frac{j}{W_s}\left[\frac{S}{D}\right] \tag{B.17}$$

$$[vp] = \frac{j}{W_s}\left[\frac{\tau}{D}\right]. \tag{B.18}$$

where W_s is the Lorentz factor of the shock, $D = \rho W$ the rest-mass density, $S = \rho h W^2 v$ the momentum density, $h = 1 + e + p/\rho$ the specific enthalpy, $\tau = \rho h W^2 - p - \rho W$ the energy density, and j the invariant mass flux,

$$j = W_s D_2 (V_s - v_2) = W_s D_1 (V_s - v_1). \tag{B.19}$$

If the shock is strong, the kinetic energy in the pre-shock and the rest-mass energy in the post-shock is negligible. Therefore, $v_1 \sim 0$ and $p_1 \sim 0$. Then, replacing β and e in Equations (B.18) and (B.19) with Equations (B.13) and (B.12) results in Equation (B.17)

and

$$\rho_2\gamma \quad = \quad 2\rho_1\Gamma^2. \tag{B.20}$$

The expression of Equation (B.20) can be rewritten in terms of the number density n as Equation (2.6). Equation (2.7) results from (B.17).

Appendix C

Lorentz transformation

In order to calculate the variety of the energy or momentum of a particle in a fluid moving at high velocity, it is necessary to calculate the four-vector $[\epsilon, \boldsymbol{p}]$ of the particle by utilizing a coordinate transformation in the spacetime.

In this thesis, a transformation process consists of two rotations and a Lorentz boost along the fixed z-axis. For example, in a transformation from the observer frame into the rest-frame of the fluid ($[\epsilon, \boldsymbol{p}] \rightarrow [\epsilon', \boldsymbol{p}']$), the three momentum of the particle rotates around the z- and y- axis before the Lorentz transformation, so that the momentum vector corresponds to the z-axis. The transformation can be written as follows.

$$\begin{bmatrix} \epsilon' \\ p' \cos\phi' \sin\theta' \\ p' \sin\phi' \sin\theta' \\ p' \cos\theta' \end{bmatrix} = \boldsymbol{L_z} \boldsymbol{R_y}(\theta) \boldsymbol{R_z}(\phi) \begin{bmatrix} \epsilon \\ p \cos\phi \sin\theta \\ p \sin\phi \sin\theta \\ p \cos\theta \end{bmatrix}, \tag{C.1}$$

where θ and ϕ are the inclination and azimuth angle of the motion of the particle with respect to the $z - x$ plane,

$$\boldsymbol{L_z} = \begin{bmatrix} \gamma & 0 & 0 & -\gamma\beta \\ 0 & 1 & 0 & 0 \\ 0 & 0 & 1 & 0 \\ -\gamma\beta & 0 & 0 & \gamma \end{bmatrix},$$

and

$$\boldsymbol{R_y}(\theta) = \begin{bmatrix} 1 & 0 & 0 & 0 \\ 0 & \cos\theta & 0 & -\sin\theta \\ 0 & 0 & 1 & 0 \\ 0 & \sin\theta & 0 & \cos\theta \end{bmatrix}, \quad \boldsymbol{R_z}(\phi) = \begin{bmatrix} 1 & 0 & 0 & 0 \\ 0 & \cos\phi & \sin\phi & 0 \\ 0 & -\sin\phi & \cos\phi & 0 \\ 0 & 0 & 0 & 1 \end{bmatrix} \tag{C.2}$$

The inverse transformation is written as follows.

$$\begin{bmatrix} \epsilon \\ \epsilon\cos\phi\sin\theta \\ \epsilon\sin\phi\sin\theta \\ \epsilon\cos\theta \end{bmatrix} = \boldsymbol{R_z}(\phi)^{-1}\boldsymbol{R_y}(\theta)^{-1}\boldsymbol{L_z}^{-1} \begin{bmatrix} \epsilon' \\ p'\cos\phi'\sin\theta' \\ p'\sin\phi'\sin\theta' \\ p'\cos\theta' \end{bmatrix}. \tag{C.3}$$

Appendix D

Relativistic effect on radiation

Properties of electro-magnetic radiation such as GRBs are strongly influenced by relativistic effects in the source. When the effects of gravity are negligible, the influence can be expressed by considering an approximation of special relativity, which includes the theories of mass-energy equivalence, relative difference in velocity (the Doppler effect), the universal speed limit (, and so on). In this chapter, I focus on the beaming effect.

D.1 Beaming effect

Due to the Doppler effect, photons are strongly collimated into a small angle when they are produced in a relativistic expanding outflow (, as shown in Figure D.1). Considering a emitting element moving along the line of sight (x-axis) with a velocity v, the relation between the velocity u of an emitted particle in the observer's frame S and the velocity u' in the rest-frame of the element S' can be expressed as

$$u_{\parallel} = \frac{u' \cos\theta' + v}{1 + v u' \cos\theta'/c^2}, \tag{D.1}$$

$$u_{\perp} = \frac{u' \sin\theta'}{\gamma(1 + v u' \cos\theta'/c^2)}, \tag{D.2}$$

where $u_{\parallel}$ and $u_{\perp}$ are velocity components parallel and perpendicular to the x-axis, θ' is the angle between the directions of the particle and the x-axis in the S'-system, and γ the Lorentz factor of the element. Therefore, in the S-system, the angle between the particle and the x-axis θ follows

$$\tan\theta = \frac{u_{\perp}}{u_{\parallel}} = \frac{u' \sin\theta'}{\gamma(u' \cos\theta' + v)}. \tag{D.3}$$

When $u' = c$, Equation (D.3) yields

$$\tan\theta = \frac{\sin\theta'}{\gamma(\cos\theta' + v/c)}, \quad \cos\theta = \frac{\cos\theta' + v/c}{1 + (v/c)\cos\theta'}, \quad \sin\theta = \frac{\sin\theta'}{\gamma(1 + v/c\cos\theta')}, \tag{D.4}$$

corresponding to the aberration of light. Therefore, when $\theta' = \pi/2$ and $\gamma \gg 1$,

$$\tan\theta = \frac{c}{\gamma v}, \quad \cos\theta = \frac{v}{c}, \quad \sin\theta = \frac{1}{\gamma} \ll 1. \tag{D.5}$$

From Equation (D.5), $\sin\theta \sim \theta$ is derived, so

$$\theta \sim \frac{1}{\gamma}. \tag{D.6}$$

Accordingly, when photons are emitted isotropically from a relativistic source, most of them are concentrated into a forward cone with half-angle of $1/\gamma$.

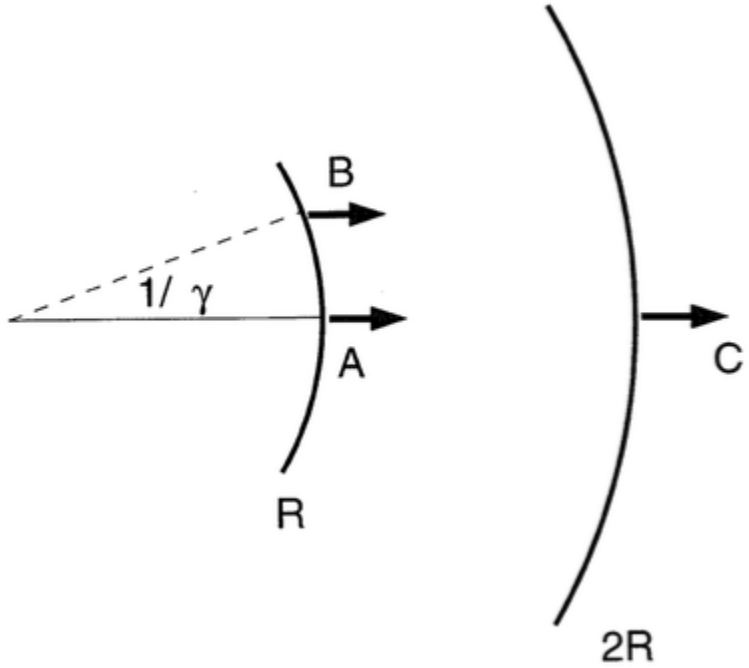

Figure D.1: Beaming effect on the radiation emitted from an outflow expanding with relativistic velocities (Ruderman, 1975, Figure 3).

Acknowledgments

First of all, I would like to appreciate to my supervisor Toshikazu Shigeyama for everything he did for me during my postgraduate life. By providing a lot of ideas, advice, intriguing topics, opportunities to attain scientific meetings, and time for discussion, he always lead me to having interests in scientific questions, and helped me to understand fundamental physics. He also helped improving this thesis by frequently giving me comments. I especially thank him for continuous encouragement.

I gratefully acknowledge Akihiro Suzuki for his advice. Statement of this thesis owe his ideas a lot. He also provided me advice on calculations and helped me to understand supernova physics. I am also grateful to Masamichi Kutsuna for helping me to improve calculations.

Finally, I thank to the members of Shigeyama-laboratory. Nobutoshi Yasutake, Ryo Tsutsui, Takuma Suda, Yutaka Komiya, Toshio Nakano, Yoichiro Tsuboki, Kentaro Wada, Miyu Masuyama, and Kazuhiro Noda provided me frequent opportunities of discussion. I wish to gratefully acknowledge all of them for sharing the exciting dates.